UNIVERSITY OF CALIFORNIA SAN DIEGO

The Development of Soft Actuation and Selective Control Methods through Vaporization

A dissertation submitted in partial satisfaction of the
requirements for the degree Doctor of Philosophy

in

Materials Science and Engineering

by

Han-Joo Lee

Committee in charge:

Professor Kenneth J. Loh, Chair
Professor Shengqiang Cai
Professor James Friend
Professor Michael Todd
Professor Michael Tolley

2021

The dissertation of Han-Joo Lee is approved, and it is acceptable in quality and form for publication on microfilm and electronically.

University of California San Diego

2021

DEDICATION

This dissertation is dedicated to God, my family, and Chang.

Thank you for your endless guidance and support.

EPIGRAPH

‘Anyone who wants to be first must be the very last, and the servant of all.’

- Mark 9:35

TABLE OF CONTENTS

LIST OF FIGURES

LIST OF TABLES

ACKNOWLEDGMENTS

My sincere thanks go to Professor Kenneth Loh for giving me the opportunity to conduct research and believing in me throughout my time at UCSD. I wouldn't have been able to study so far away from home without his help. His mentorship not only made me work hard but also gave me the freedom over my research, leading me to become a better scholar I am today.

I also thank Dr. Christopher Spadaccini, who helped me conduct my research at the Lawrence Livermore National Laboratory (LLNL). I would also like to thank Professor Alicia Kim and her postdocs, Hayoung Chung and Jaeyub Hyun, for helping me with finite element models and shape optimization. My research also wouldn't have been possible without the generous help from Professor Francesco Lanza di Scalea, who let me borrow whatever ultrasonics equipment I needed.

I also cannot fail to mention all the nice and smart people I encountered at UCSD and LLNL. Morgan Funderburk, Yujin Park, Bomi Lee, Sumit Gupta, Yening Shu, Sijia Li, Xinlun Zhao, Yun-An Lin, Long Wang, Irene Zhao, Julie Mancini, and Ishan Joshipura, you all made my long journey possible.

Chapter 2, in full, is a reprint of the materials as it appears in Liquid vaporization actuated soft structures with active cooling and heat loss control, Smart Materials and Structure 30 (2021) 055007, H.-J. Lee and K.J. Loh. The dissertation author was the primary investigator and author of this paper. This work was supported by the U.S. National Science Foundation under Grant No. CMMI-1762530. Additional support was provided by the Jacobs School of Engineering, University of California San Diego.

Chapter 3, in part, is a reprint of the materials as it appears in Soft material actuation by atomization, Smart Materials and Structure 28 (2018) 025030, H.-J. Lee and K.J. Loh, Characterization of a soft gripper with detachable fingers through rapid droplet evaporation, Proceedings of 3rd IEEE International Conference on Soft Robotics (2020) 83-88, H.-J. Lee, N. Melchor, H. Chung, and K.J. Loh, Soft material actuation and shape-change through ultrasonic atomization, Proceedings of the 12th International Workshop on Structural Health Monitoring, Stanford, CA (2019), H.-J. Lee, N. Melchor, and K.J. Loh,

Characterization of soft actuation through ultrasonic atomization, TMS 149th Annual Meeting & Exhibition Supplemental Proceedings, Springer, San-Diego, CA (2020) 881-888, H.-J. Lee and K.J. Loh, and Actuation of soft materials through ultrasonic atomization, Bioinspiration, Biomimetics, and Bioreplication VIII 10593 (2018) 105930Z, H.-J. Lee, M. Funderburk, and K.J. Loh. The dissertation author was the primary investigator and author of these papers. These works were supported by the U.S. National Science Foundation under Grant No. CMMI-1762530. Additional support was provided by the Jacobs School of Engineering, University of California San Diego.

Chapter 4, in part, is a reprint of the materials as it appears in Rapid soft material actuation through droplet evaporation, Soft Robotics (In press) DOI: 10.1089/soro.2020.0055 H.-J. Lee, P. Prachaseree, and K.J. Loh, and in part, has been submitted for publication of the material as it may appear in Frontiers in Robotics and AI (2021), H.-J. Lee, E. Guerra-Bravo, A. Baltazar, and K.J. Loh. The dissertation author was the primary investigator and author of both papers. These works were supported by the University of California Institute for Mexico and the United States (UC MEXUS) under Grant No. CN-19-153 and the U.S. National Science Foundation under Grant Nos. CMMI-1762530 and CMMI-2032021. Additional support was provided by the Jacobs School of Engineering, University of California San Diego.

Chapter 5, in full, is currently being prepared for submission for publication of the material, H.-J. Lee, J.A. Mancini, C.M. Spadaccini, and K.J. Loh. The dissertation author was the primary investigator and author of this material. This work was supported by the U.S. National Science Foundation under Grant Nos. CMMI-1762530 and CMMI-2032021. Additional support was provided by the Jacobs School of Engineering, University of California San Diego.

VITA

2007 – 2014	Bachelor of Science, Hanyang University
2014	Student researcher, Korea Institute of Science and Technology
2014 – 2016	Master of Science, Hanyang University
2016 – 2021	Doctor of Philosophy, University of California San Diego
2021	Intern, Lawrence Livermore National Laboratory

Publication

1. H.-J. Lee, E. Guerra-Bravo, A. Baltazar, and K.J. Loh, Controlling atomization to improve soft actuation through vaporization, Frontiers in Robotics and AI 8 (2021) 747400
2. E. Guerra-Bravo, H.-J. Lee, A. Baltazar, and K.J. Loh, Study of vibration analysis of a piezoelectric ultrasonic atomizer, Applied Sciences 11 (2021) 8350
3. S. Gupta, Y. Lin, H.-J. Lee, J. Buscheck, R. Wu, J.P. Lynch, N. Garg, and K.J. Loh, In-situ crack mapping of large-scale self-sensing concrete pavements using electrical resistance tomography, Cement and Concrete Composites 122 (2021) 104154
4. H.-J. Lee and K.J. Loh, Liquid vaporization actuated soft structures with active cooling and heat loss control, Smart Materials and Structure 30 (2021) 055007
5. H.-J. Lee, P. Prachaseree, and K.J. Loh, Rapid soft material actuation through droplet evaporation, Soft Robotics (In press) DOI: 10.1089/soro.2020.0055
6. H.-J. Lee, N. Melchor, H. Chung, and K.J. Loh, Characterization of a soft gripper with detachable fingers through rapid droplet evaporation, Proceedings of 3rd IEEE International Conference on Soft Robotics (2020) 83-88
7. H.-J. Lee and K.J. Loh, Characterization of soft actuation through ultrasonic atomization, TMS 149th Annual Meeting & Exhibition Supplemental Proceedings, Springer, San-Diego, CA (2020) 881-888
8. H.-J. Lee, N. Melchor, and K.J. Loh, Soft material actuation and shape-change through ultrasonic atomization, Proceedings of the 12th International Workshop on Structural Health Monitoring, Stanford, CA (2019)
9. H.-J. Lee, and K.J. Loh, Soft material actuation by atomization, Smart Materials and Structure 28 (2018) 025030
10. S. Gupta, H.-J. Lee, K.J. Loh, M.D. Todd, J. Reed, A.D. Barnett, Noncontact strain monitoring of osseointegrated prostheses, Sensors 18(9) (2018) 3015
11. H.-J. Lee, M. Funderburk, K.J. Loh, Actuation of soft materials through ultrasonic atomization, Bioinspiration, Biomimetics, and Bioreplication VIII 10593 (2018) 105930Z

ABSTRACT OF THE DISSERTATION

The Development of Soft Actuation
and Selective Control Methods through Vaporization

by

Han-Joo Lee

Doctor of Philosophy in Materials Science and Engineering

University of California San Diego, 2021

Professor Kenneth J. Loh, Chair

Soft robotics is a promising field that can solve several limitations of traditional rigid robotics. These systems are composed of soft and flexible materials to achieve high degrees-of-freedom and compliance with their surroundings. An important part of soft robotics is developing methods to actuate the soft structures. A popular method involves inflating soft hollow structures with a pneumatic pump that can achieve rapid and precise actuation. However, the structure must be tethered to a heavy and rigid pump, which limits its application. An alternative method vaporizes embedded liquid to inflate the structure instead. The simplest and widely used design to vaporize such liquid is by installing a heating element near the liquid. Heating the system beyond the boiling point rapidly boils the liquid and deforms the structure. The small amount of liquid and heater makes it easier to be packaged into a portable device. Nevertheless, this technique possesses several limitations that must be improved to be practical. This dissertation addresses these limitations and introduces methods that can advance the field for future robotics. Chapter

2 describes how actuation through vaporization can be affected by the environment and introduces a system that consists of double-layered walls and a thermoelectric device. Chapter 3 aims to implement ultrasonic waves that propagate through materials, which enables a system with detachable parts. Chapter 4 utilizes vibrating mesh atomization to drastically improve the slow actuation speed by evaporating small droplets with large surface areas. Last, chapter 5 introduces a method that can potentially remove electrical components by combining ultrasonics with shape optimization. These studies show that soft actuation through vaporization has significant room for improvement and can potentially replace commercial actuation methods with further optimization.

Chapter 1. Introduction

Rigid robotics with metallic components led to drastic developments in science and engineering. These automated systems were the foundation for various fields such as mass manufacturing and architecture. In general, the robotic system comprises several rigid components that are assembled with actuators installed between the joints. The rigid components were capable of supporting loads up to several tons, as well as precisely controlling its movement in the nanometer scale. The rapid advancement in robotics was possible because its movement was easy to control and predict through simple simulations when there is minimal effect from the environment. This means that the performance of these systems can be easily simulated and tested before assembling the final product. However, the same rigid components prevent the use of traditional robots in unpredictable environments or applications where human interaction is needed.[1,2] The lack of compliant property is not suitable for reacting with its surroundings and can potentially damage itself or harm humans unless they are equipped with high-speed feedback control systems.[3,4]

In contrast, most animals in nature have soft tissues surrounding their bodies. The flexible nature of the tissues allows us to perform delicate tasks (such as picking up an egg or walking on pebbles) without the need to control our body parts with perfect precision.[5-8] The extreme example of these flexible tissues would be the octopus that can fit through an aperture that is much smaller than its body.[9-13] In addition, the soft tissue can easily perform multiple tasks such as actuating, sensing, and changing its surface texture and color.[11,14]

Inspired by these biological systems, soft robots comprises of flexible elastomers that can stretch and bend without joints.[15-20] The higher degrees-of-freedom (DOF) of the material enables various types of movements, which is more amenable to applications that interact with diverse surroundings.[21] This is due to the fact that soft materials provide impact attenuation, strain dissipation, and conformability when in contact with other objects.[22] The compliant property of the material enables adaptable control that does not

require precise feedback. In addition, the robust nature of these soft robots allows the application to be used in extreme environments where the system should operate even after severe impacts.

Actuation methods used for soft robots are fundamentally different from traditional actuators that convert electric or magnetic energy to mechanical movements on a single point. Traditional robotic systems require an actuator (such as a motor) at the joint between two rigid components. Thus, increasing the DOF requires a greater number of actuators, and the increase in weight requires stronger components as well as stronger motors. Since the angle of the joints can be carefully controlled with the motor, traditional robots are mostly used to perform repetitive tasks such as simple labors that require precision or a large amount of force. On the other hand, soft robotic structures that are made from flexible elastomers do not deform at specific joints. The actuation method should be able to deform the entire structure by using lower rigidity components as possible. In addition, the weight of the system should be much lighter since the soft structure cannot sustain much weight. Several different methods have been developed to meet these goals, and they can be categorized into two different mechanisms.

One way of achieving deformation is to change the pressure inside a hollow structure. During inflation, the movement can be controlled by fabricating the structure with a certain design. The PneuNet is a popular design that bends the structure upon inflation, and the bellows structure demonstrates unidirectional deformation.[23,24] Another method is to install secondary materials (*e.g.*, metal wires) to limit deformation in a certain direction.[25,26] Different types of deformation can be achieved by adjusting the winding angle of the material.[27] The methods to increase internal pressure in the soft materials include connecting the structure to a fluidic pump or vaporizing liquid that is embedded in the structure.

Another mechanism for soft actuation is utilizing materials that deform under certain stimuli. Shape memory alloys (SMA) deform to its original shape when exposed to high temperatures.[28] The material can be embedded inside the structure and the heat can be provided through injecting current, which results in joule heating.[29] Stimuli-responsive polymers (SRP) are another example that can react to various external stimuli, depending on how the material was designed.[30] These include polymers that react to temperature, voltage and magnetic fields, and even humidity.

1.1. Development of soft robotics

Soft robotics has recently become one of the most popular topic in the field of robotics to bridge the gap between man-made automatic systems and animals found in nature.[20] The term "soft" was used in a paper on McKibben muscles in the year 2000.[31] In this study, braided shell threads were wrapped around rubber tubes to control the deformation upon inflation. However, this actuator was still connected at the joint of rigid components, showing limited compliance from compressed gas inside the rubber tube. These compliant joints were studied over time, and the term "soft robotics" was adopted in the field in 2004.[32] Early interests that fueled the field of soft robotics comes from mimicking the movement of animals without skeletal structures. The octopus is a great example, and its muscle structures were imitated with several inflating structures in 2009.[33] Since then, various studies worked on mimicking other animals, including caterpillars,[34] meshworms,[35] and starfish.[24] Diverse actuation systems were developed under various names, and the number of publication on soft robotics steadily increased since 2008.[36] To date, numerous studies were developed and branched out to achieve the goal of soft robotics, and they were categorized by actuation methods in the following section.

1.2. Actuation through pressure change

1.2.1. Fluidic pumps

Hydraulic pumps are one type of fluidic actuators that inject fluids to deform soft structures. Soft structures actuated by hydraulic pumps are capable of applying large amounts of force by utilizing incompressible liquids.[37] Since liquids are generally heavy as compared to soft hollow elastomers, these methods are suitable for underwater applications where weight is no longer an issue. Katzschmann *et al*.[38] demonstrated swimming locomotion with a soft robot that was inspired by a fish. The tail of the fish consisted of two channels that moved back-and-forth with a hydraulic pump. The system was capable of mimicking the movement of a fish, which also demonstrated an escape maneuver.[39] The system was controlled by acoustic signals,

and the surrounding was recorded with an embedded camera. The robotic fish easily blended into the environment by maneuvering without creating any turbulence. Another example is the soft robotic gripper that was implemented on a remotely operated vehicle for collecting samples underwater.[40] Since the samples from deep reefs are very delicate and brittle, the soft manipulator showed advantages over traditional rigid grippers. The contact area and the gripping force were controlled by simply installing a different material (*i.e.*, foam) on the surface of the finger.

Another type of fluidic actuator is the pneumatic pump, which injects pressurized gas to inflate the structure.[41] Since gas is much lighter than liquid, pneumatic actuation is suitable for most applications, where the soft structure should sustain its own weight.[42-44] Tolley *et al*.[45] demonstrated a large-scale locomotion robot that was able to support the entire actuation system including the pneumatic pump. The weight of the whole system was reduced by embedding hollow glass microspheres into the elastomer. The tough nature of the soft elastomer enabled the crawling robot to function in shallow waters, fire, snow, and even after being run over by a car. Pneumatic actuation was also implemented on a soft robot that was fabricated from a self-healing elastomer.[46] The material utilized a thermo-reversible Diels-Alder reaction in which the healing process was triggered when the material was subjected to heat.[47] The elastomer was flexible enough to achieve different types of deformation upon inflation, and gripping motion was demonstrated. After cutting the material with a blade, it was heated to 80 °C, which healed the structure to repeat the initial performance.

1.2.2. Liquid-gas phase transformation

As compared to fluidic actuators that require a heavy and bulky pump, vaporizing liquid to increase the inner pressure of the structure only requires a small, embedded heating element. This mechanism allows one to minimize the form factor and weight of the entire system, as well as to fabricate a soft robot that is not tethered to an external component. In general, a liquid with

a low boiling point is injected into the soft hollow structure. Heating the liquid results in vaporization, and the increase in volume inflates and deforms the system. Selecting a liquid with a lower boiling point actuates the structure faster and reaches higher maximum stress.[48]

The simplest way to increase temperature is by heating the system through joule heating. Since heating bulk liquid requires a long time, Miriyev *et al*.[49] dispersed ethanol into small cavities in the micrometer scale[50] inside the soft elastomer. Heating the entire system up to 90 °C with embedded resistive wires boiled the ethanol and expanded the structure. Repeatable actuation was demonstrated by air-cooling the system to condense the vapor back to liquid. Instead of injecting current through a wire, Boyvat *et al*.[51] applied magnetic fields onto an embedded resonator. The system was completely untethered, and the resonator heated up to the boiling point when subjected to a magnetic field. In this example, a liquid with a boiling point as low as 34 °C was used to accelerate actuation.

The temperature change to actuate soft structures can also be provided by methods other than joule heating. Rolling locomotion was demonstrated on a fully untethered robot by placing it on a hot surface.[52] The liquid-filled cavity that comes into contact with the hot surface inflated and rotated the soft structure. The next cavity that touched the hot surface boiled the embedded liquid, and the repeating reaction resulted in rolling locomotion of the system on the hot surface. The inflated cavity was air-cooled until it returned to its original shape by the time the system completed one cycle. Another example is a bending structure inspired by the stem of sunflowers.[53] Near-infrared lasers were used to heat one side of an untethered cylinder-shaped structure to achieve bending motions. A laser with 808 nm in wavelength and light density of 0.8 W/cm^{-2} was used to heat the cavity to 130 °C. Increasing the number of vertical cavities resulted in higher DOF.

1.3. Actuation through smart materials

1.3.1. Shape memory alloy

One of the most widely used stimuli-responsive materials is the shape memory alloy (SMA) that responds to temperature.[28,54] SMAs can be designed to remember a certain shape when subjected to a certain amount of temperature.[55] Similar to vaporizing liquid, heating a deformed SMA results in phase transformation that returns the material into its original shape. When the deformation to its original shape is blocked, the material can also apply a consistent force onto the structure.[55,56] Their high energy density as well as stability and repeatability allowed the material to be applied as soft actuators.[57] In general, the material is fabricated into a shape of a spring to increase the recoverable strain to as high as 1000 %.[54] As a result, most soft actuators implement SMAs with the shape of a spring that performs one-dimensional actuation.[58]

In another example, peristaltic locomotion was demonstrated by wrapping SMA springs around a meshworm.[59] Contracting the springs at higher temperatures reduced the diameter of the cylindrical meshworm, which resulted in longitudinal deformation. By selectively actuating the springs in different locations, the system was able to crawl forward in a manner that is similar to a worm. A similar method was also implemented on a robotic arm that was inspired by the octopus.[29] The transverse actuator consisted of SMA springs that were connected to a braided sleeve that is similar to the meshworm. The longitudinal actuation was achieved by pulling cables that were installed inside the arm. The complex movement of an octopus was imitated by combining these two actuation methods.

1.3.2. Stimuli-responsive polymers

Various applications have pushed the demand to require smaller actuation components in their systems. Manufacturing compact actuators limit the implementation of complicated circuits and assemblies. As a result, SRP materials are receiving much attention since the material is easy to fabricate on a small scale, and it can deform when the environment changes.[60]

As compared to other materials, SRPs can be designed to react to various types of stimuli,[7,30,61] which include electric field[62,63], magnetic field[64], heat[65,66], light[67,68], and chemical changes.[17,69-72] Signals such as electric field, magnetic field, and light can be easily tuned to precisely actuate the system, whereas heat and chemical changes involve diffusion and tend to be slower. There are various types of polymers that have a distinct and unique mechanism to react to their stimuli.

Liquid-crystal elastomers (LCE) consists of long polymer chains with liquid crystals (LC) that are periodically bonded to the sides.[73] The simplest ordered phase is the nematic mesophase, where the LC rods are aligned uniformly in one direction. The isotropic phase indicates a state where these mesogens are in random orientations. Depending on how the material is designed, the material can shift between these two phases when subjected to certain stimuli. In general, the LCE stretches during nematic mesophase and contracts during isotropic phase. He *et al*.[66] demonstrated a soft LCE actuator that contracts when subjected to heat. The material was prestretched during curing to maintain the nematic state, which transformed into its isotropic phase when the temperature increased. By controlling joule heating of the embedded wire, the actuator was capable of exhibiting various types of movements.

Hydrogels are materials that drastically change their volume upon absorbing solvents.[74,75] The stimuli that can affect this change in volume can also be controlled when designing the material. Like other polymers, hydrogels are made from cross-linked chains. When a certain solvent comes into contact with the hydrogel, it penetrates into the material by changing it into a soft phase that expands the chains. As the distance between the chain increases, more solvent can penetrate deeper into the material. The process is generally slow, since the method involves diffusion. However, Lee *et al*.[69] demonstrated rapid actuation by fabricating hydrogels into a buckled geometry. When the structure absorbed the solvent, the material expanded and snapped due to its bistable design. The structure demonstrated a jumping movement within 5 s after it was exposed to the solvent.

1.4. Potential and limitations of actuation through vaporization

Among these numerous methods, this dissertation focuses on soft actuation through liquid vaporization, since it has significant room for improvement and the potential to replace the widely used pneumatic pumps. Actuation through vaporization is a complex multi-physics process that involves thermodynamics, kinetics, and structural mechanics. First, heat must propagate from the heat source to the liquid. Second, the heat vaporizes the liquid into vapor. Then, this increases the volume of gas inside the chamber, which applies additional pressure to the inner walls. Heat dissipating to the surrounding must also be considered throughout actuation, as the environment might highly affect system performance. Nevertheless, the complexity of the problem also indicates that there are many parameters to optimize to improve performance. In addition, this method only requires a relatively small heat source and liquid that is already embedded inside the system, making it desirable for miniaturized and untethered systems.

One of the limitations of actuation through vaporization is that performance is highly affected by heat transfer. The cyclic motion of the actuator can be categorized into two stages. During the heating stage, the heater vaporizes the liquid. Containing the heat is important, as any heat loss to the environment will slow down actuation. During the cooling stage, however, the system must cool down to condense the vapor back to liquid. Higher heat loss will return the structure to its original shape faster during this reversing step. Since the performance is highly dependent on heat loss, the surrounding environment (*e.g.*, underwater) will have a crucial effect on this actuation method.

Another problem is the slow actuation speed, which might be the most crippling limitation. There is a significant time lag between powering the system and the actual response from the structure, as heat propagation and boiling liquid is time-dependent. Furthermore, the soft elastomers and liquid used in this method generally have high heat capacity and low thermal conductivity. One of the easier methods to increase actuation speed is using liquid with high vapor pressure.[48] Liquid with high vapor pressure will vaporize much faster even when the temperature increase is small. This was demonstrated

in the work by Boyvat *et al*.[51], where a liquid with boiling temperature of 34 °C was used to inflate a bellows structure.

1.5. Research objective and dissertation outline

The objective of this research is to address these limitations of actuation through vaporization and to suggest solutions by combining the method with other techniques. Chapter 2 combines double-walled structures with a thermoelectric device to gain better control of heat loss and speed up the cooling process. Chapter 3 utilizes ultrasonic waves that propagate through the structure to atomize liquid into small droplets. This method enabled structures that can be easily detached and replaced. Chapter 4 improves the atomization method used in Chapter 3 to achieve a rapid actuation rate that is comparable to commercial pneumatic pumps. Chapter 5 introduces a novel method to manipulate ultrasonic waves through shape optimization and achieve selective actuation that was inspired by biological systems. The overall study shows promising results that can advance soft actuation through vaporization closer to practical applications as well as suggest creative methods to take advantage of ultrasonic waves.

Chapter 2. Actuation through Active Cooling and Heat Loss Control

2.1. Introduction

Several techniques have been developed to fully utilize liquid vaporization for soft actuation. A popular method involves installing a joule heating element inside the structure to boil the embedded liquid.[76-80] These studies applied current to conductive wires or fabrics installed inside soft elastomers for joule heating. Ethanol was either filled in hollow chambers or distributed in small cavities inside the elastomer matrix. Oh *et al*.,[80] in particular, addressed the slow thermal-response time and installed microcapsules of liquid metal to increase thermal conductivity. Other methods heated the soft structures from external sources such as an oven,[81] heated surface,[52] or even lasers.[53,82] The benefit of these methods is that the system does not need to carry a power supply and can easily be untethered for deployment.

Despite these various approaches, comparing the performance of these studies are not straightforward, since actuation through vaporization is an intricate process. In most cases, actuation involving heat occurs under non-equilibrium conditions, making it difficult to analyze. Moreover, actuation is also affected by the thermal properties of the liquid and encasing structure. Even when implementing the same heating mechanism, using a liquid with higher vapor pressure will improve actuation. The thermal conductivity of the soft material, as well as the geometry of the structure, also affect heat loss during both the actuation and cooling processes. Furthermore, the effect of heat loss can become even more significant depending on its operational environment (*e.g.,* underwater). As a result, heat transfer analysis is imperative to better understand the actuation mechanism.

This chapter focused on actively controlling heat loss to enhance speed during both the actuation and cooling processes and to develop a system that can perform consistently in various thermal environments. In general, heat can be lost through conduction, convection, and radiation. While all three mechanisms are worth investigating to fully control heat loss, this study focused on adjusting thermal conductivity by incorporating a layer of air between the walls. Different wall designs were

analyzed using finite element (FE) modeling to study how it affects heat transfer and structural mechanics. Tests were conducted on a soft elastomer to determine the parameters necessary for FE modeling of the heat transfer process. Simple cuboid structures with single- and double-layered walls were designed to analyze heat loss, as well as displacement during inflation. When fabricating the structure, soft double-layered walls were combined with a thermoelectric device to manipulate heat loss. During actuation, the thermoelectric layer was powered to heat the system, while the double-layered walls minimized heat loss. After actuation, current flow to the thermoelectric device was reversed, which increased heat dissipation and allowed rapid cooling inside the structure. Testing the structure underwater further enhanced the Peltier effect and increased cooling rate. For validation, a soft anemone-like structure was fabricated and operated underwater, which opened upon actuation and closed during cooling. Its actuation and cooling speeds were compared with different conditions to validate the potency of the method.

2.2. Material background

2.2.1. Effect of soft elastomer properties

Thermal properties of soft materials have a substantial influence on reversible actuation through vaporization. Figure 1 shows a schematic of the actuator system. The cross-section illustrates a soft cuboid structure that is partially filled with liquid; the left half shows the heating (*i.e.*, actuation) process. Temperature is increased to boiling by injecting current into the heater. During this process, the thermal conductivity of the walls should be low enough to effectively contain heat inside the chamber. High thermal conductivity will result in significant heat loss, which in turn slows actuation. On the other hand, the right half of the illustration in figure 1 shows the cooling process that returns the structure to its original shape. Since the amount of gas inside the structure is directly dependent on temperature, high heat loss is required to quickly reverse actuation, which can be improved by using materials with high thermal conductivity.

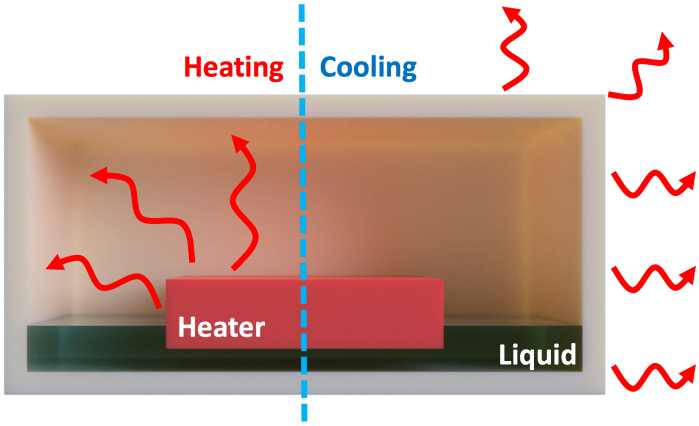

Figure 1. The illustration shows how heat loss affects soft actuation during vaporization and the cooling process.

These competing requirements mean that systems without a method to actively control heat loss will always sacrifice either actuation or cooling performance.

In this work, the wall design of soft materials was combined with a thermoelectric device to maximize both the forward and reverse actuation performance. Double-layered, versus single-layered, walls were studied to reduce heat loss and to increase displacement during inflation. When fabricating the structure, a commercial thermoelectric device was used as the bottom layer. Thermoelectric devices are operated to induce a temperature difference between its opposite surfaces, which was used to heat and cool the liquid inside the chamber by reversing current flow. Since Peltier cooling performs best when there is a heatsink on the heated side, the system showed high potential when used underwater. While the low thermal conductivity of the double-walled structure improves actuation, the thermoelectric device can improve the reversing (*i.e.*, cooling) process. Recent advancements in thermoelectric systems, such as flexible thermoelectric devices,[83] enable realization of a fully soft heating and cooling system.

2.2.2. Soft material characterization

Dragon skin FX-Pro was used as the soft elastomer in this study. The thermal conductivity and heat capacity of Dragon skin was measured through simple experiments. A hot wire method was used to measure thermal conductivity, which is illustrated in figure 2(a).[84-86] A Nichrome wire was installed through the middle of a cylindrical Dragon skin structure. While heating the structure, temperature was recorded with a thermocouple embedded inside the material. The thermal conductivity, λ, was calculated by:

$$\lambda = \left(\frac{q}{4\pi}\right) \cdot \left(\frac{dT}{d(\ln \tau)}\right)^{-1} \quad (1)$$

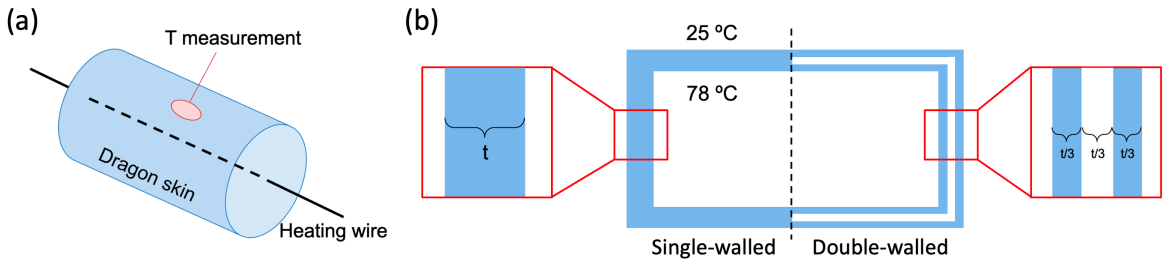

Figure 2. (a) A hot wire method was used to measure the thermal conductivity of the soft Dragon skin. (b) The illustration shows how the walls were designed for FE modelling. The temperature of the inside and outside of the chamber was 78 °C and 25 °C, respectively.

where q is specific heat output, T is temperature, and τ is time. The measured temperature can be plotted as a function of logarithmic time, and equation (1) becomes:

$$\lambda = \frac{Ri^2}{l4\pi a} \tag{2}$$

where R is resistance, i is current, l is length of Dragon skin, and a is the slope. The measured thermal conductivity of Dragon skin was ~0.25 W mK^{-1}.

2.3. FE study of double-layered structure

2.3.1. FE modeling

Two FE modeling studies were conducted with *COMSOL* to analyze heat transfer and structural mechanics. Since actuation involves numerous physics (*i.e.*, joule heating, Peltier effect, heat transfer, phase transformation, and structural mechanics), the two simulations were simplified to decrease computation time and analyze how the double-walled design directly affects heat loss and inflation individually. The cross-section of the designed structure is shown in figure 2(b). The left half shows a single-walled structure, whereas the right half shows a double-walled structure. The double-walled structure had three layers of material (*i.e.*, Dragon skin, air, and Dragon skin), and the total thickness, t, was equivalent to the single-layer. Heat loss analysis was conducted by assuming that the temperature inside the structure was 78 °C, which is the boiling temperature of ethanol (*i.e.*, the embedded fluid). In addition, the surrounding temperature was assumed to be 25 °C, since the fabricated structure was tested underwater. The total amount of heat loss was simulated by assuming the temperature of the surrounding and inside the chamber are constant. Structural mechanics was also used to determine how the walls affect displacement during inflation through a separate study. The Neo-Hookean model was used to define the hyperelastic material, with its shear modulus (64.7 kPa)

obtained from a previous study.[87] The bottom layers were assumed to be fixed in place, while the ideal gas law was used to define the gas inside the chamber and the layer in between two elastomer walls. The pressure inside the chamber, as well as the air layer between the double-layered wall, were updated using:

$$\frac{P}{P_0} = \left(\frac{V_0}{V}\right)^{\gamma} \tag{3}$$

where P is pressure, V is volume, and γ is specific heat ratio, and subscript 0 denotes the initial condition. The maximum displacement of the top layer was measured when the initial pressure of ~1.2 atm (equivalent to the vapor pressure of ethanol at ~45 °C) was applied to the inner wall.

2.3.2. Heat loss and displacement analysis

The heat loss results are plotted in figure 3(a). When t was 2 mm, the heat loss of single- and double-walled structures were ~27 W and ~8 W, respectively. This value decreased rapidly as t increased for the single-walled structure and reached ~18 W when t was 3 mm. On the other hand, the double-walled structure showed very small changes with increasing thickness. From the results, it is evident that simply adding a thin layer of air drastically decreased system heat loss. Overall, heat loss from the single-walled structure was ~3.5 times higher than the double-walled one. Similarly, the displacement of the top layer during inflation is plotted in figure 3(b). When t was 2 mm, the displacement of the single- and double-walled structure was ~3.4 mm and ~4 mm, respectively. With increasing t, these values declined at a similar rate (or slope). Although the difference was not significant, the displacement of the single-walled structure was ~1.2 times higher than the double-walled structure. The results show that fabricating the structure with double-layered walls would enhance the actuation phase due to low heat loss

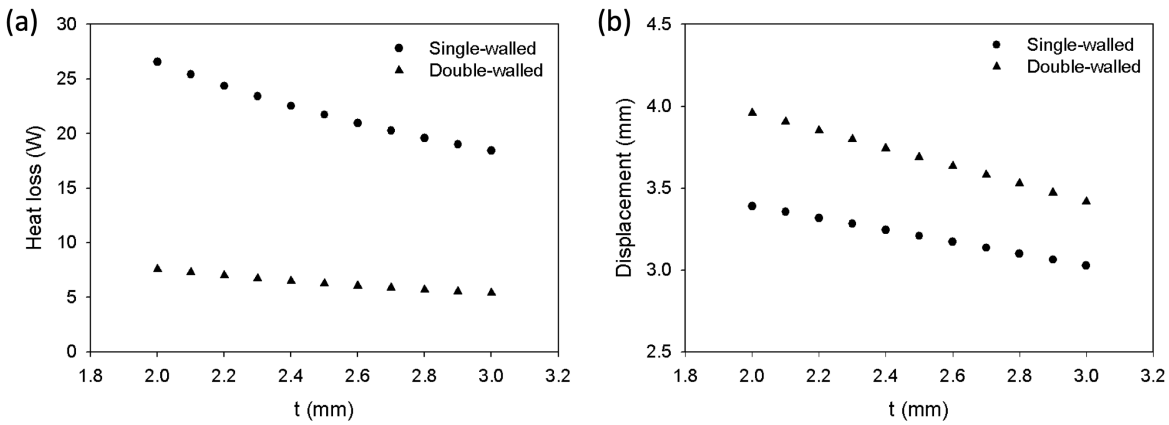

Figure 3. (a) An FE model was used to analyze the heat loss of single- and double-walled structures over a range of total wall thicknesses. (b) The displacement of the top layer was analyzed when the structures were inflated.

while attaining higher displacement under the same conditions. Although these simplified simulations do not represent the exact values of the following experiment, the results show a straightforward insight on how the double-layered wall affects heat loss and displacement in general.

2.4. Performance of double-layered structure

2.4.1. Fabrication

In this study, 3D-printed polylactic acid (PLA) rigid molds were used to fabricate the soft structures. Two parts of Dragon skin (Part A and Part B) were hand-mixed at a 1:1 weight ratio, and the mixture was placed in a vacuum chamber before pouring it into the mold. The mold was then placed in the vacuum chamber one more time to remove any bubbles formed during pouring. Then, the mold was left at room temperature for ∼1 h to fully cure the silicone elastomer. Figure 4(a) shows the cross-section of the cuboid actuator. Next, the thermoelectric device was placed at the bottom opening of the cuboid structure, and uncured Dragon skin was applied to seal the gap. A syringe was used to inject 2 ml of ethanol into the chamber, and the hole was sealed with the same elastomer in a similar way. The size of the single-layered structure (3 × 3 × 1.5 cm) was fabricated with 1 mm thick walls. After testing, a slightly smaller cuboid structure with 1 mm thickness was installed on the inside to form the double-walled structure.

The performance of the thermoelectric Peltier device is plotted in figure 4(b). An open-ended structure without ethanol was positioned so that the bottom (*i.e.*, outer) layer was in contact with water, while the top (*i.e.*, inner) layer was exposed to air. The amount of current was selected by slowly increasing the voltage until steady cooling was maintained on the top layer without excessive joule heating. The maximum voltage of 2.5 V resulted in ∼1 A of current. During the first phase, current was injected so that the top layer heated while cooling the bottom layer. After heating, current flow was reversed to cool the top layer while heating the bottom

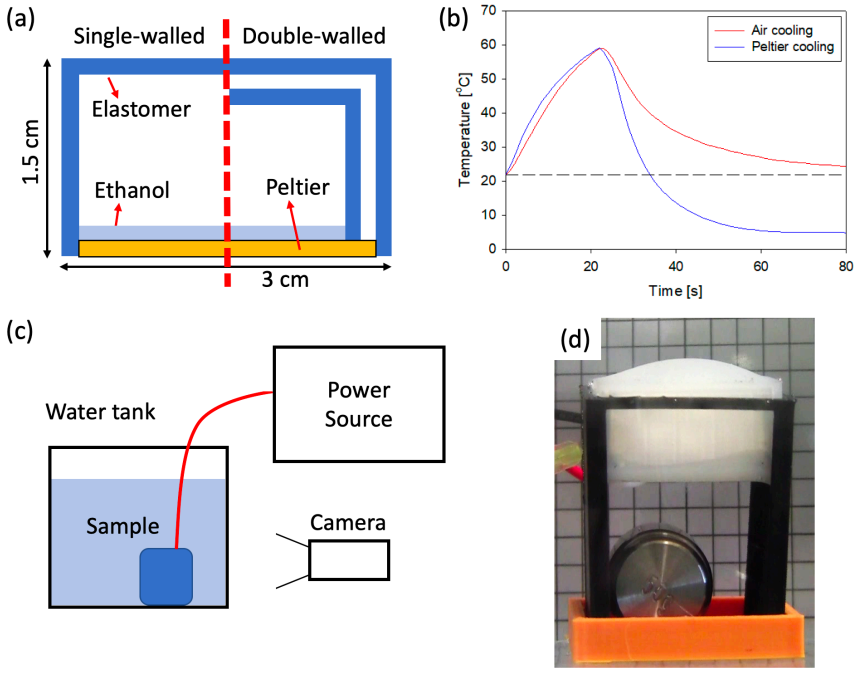

Figure 4. (a) The cross-section shows the design of the fabricated single- and double-walled soft structure. (b) The performance of the thermoelectric device is shown, where the temperature of the inner surface was measured. The inner surface reached ~ 60 °C after 20 s of heating. The system was then cooled by both air cooling and Peltier cooling. (c) The schematic shows the experimental setup. (d) The structure was actuated underwater to measure displacement over time.

layer. Temperature change during heating and air cooling is plotted in red in figure 4(b), whereas the blue plot shows temperature change during heating and Peltier cooling. The temperature reached ∼60 ◦C after ∼20 s of heating and decreased much faster during Peltier cooling as compared to air cooling. The temperature reached 25 ◦C after ∼50 s when air cooled, whereas Peltier cooling decreased the cooling time by ∼80%, taking only ∼10 s.

The setup of the underwater test is shown in figure 4(c), where the sample was placed in a large tank of water (30 × 17 × 22 cm). The Peltier device was connected to a power source, and the actuation was recorded by a camera. Figure 4(d) shows an image of the sample inside the tank, where a grid with 5 mm spacing was placed in the background. A fixture was 3D-printed with PLA to hold the soft structure. A platform was designed underneath the structure to place weights to prevent the system from floating due to buoyancy. Soft actuation was recorded by video during heating and cooling, and the displacement of the top layer was analyzed by post-processing individual image frames.

2.4.2. Actuation and active cooling

Figure 5 shows the displacement results when actuating the fabricated structure. Each structure was tested in two different environments. During the first test, the structure was fixed in place above water so that only the bottom layer of the Peltier device was in contact with liquid. This allowed maximum cooling from the device, while the soft walls were exposed to air. Afterwards, the entire structure was submerged underwater. For each environment, the structure was actuated by heating the thermoelectric device for ∼50 s, followed by cooling the system to return to its original shape. The system was cooled by simply turning off the thermoelectric device (*i.e.*, for air or water cooling) or reversing current for active Peltier cooling. The displacements were used to represent the performance of the actuation and reversing processes.

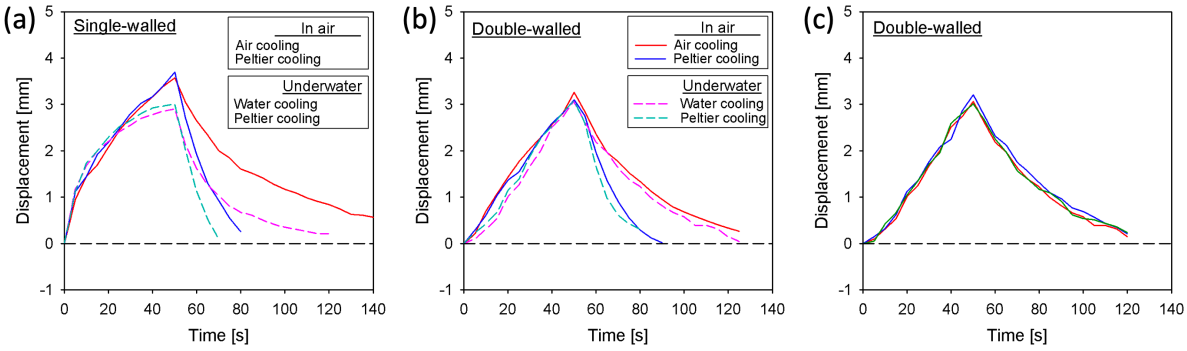

Figure 5. (a) The single-walled structure was actuated in air and underwater. The structure was actuated for 50 s and cooled down by either turning off the device or reversing the current for Peltier cooling. (b) The double-walled structure was tested under the same conditions. (c) The double-walled structure was actuated and cooled underwater 3 times to show consistency.

The single-walled structure had a wall thickness of 1 mm, and the results are shown in figure 5(a). The solid lines show the results for the structure that was exposed to air, whereas the dashed lines are results for the submerged structure. The structure reached a displacement of ~3.5 mm when in air, while it achieved ~3.0 mm of displacement underwater. The actuation rate decreased faster when the structure was underwater and began to plateau. This was due to the large heat loss from the single-walled structure, and it can be assumed that displacement will stabilize even upon further heating when the system reaches thermal equilibrium. After actuation, displacement decreased slowly once power was shut off. In contrast, when current was reversed for Peltier cooling, the displacement decreased at a much faster rate. To compare the cooling rates, the time it took for displacement to return to 0.5 mm was analyzed for both methods. When the single-walled structure was exposed to air, Peltier cooling reduced cooling time by ~74% with respect to air cooling. When submerged underwater, actively cooling the system with the thermoelectric device reduced cooling time by ~62% as compared to water cooling.

The same set of tests was conducted after adding an additional 1 mm thick layer within the previous structure to form the double-walled system, and the results are plotted in figure 5(b). As compared to the previous single-walled structure, the tests conducted in air and underwater showed little difference. This indicates that the double-walled structure was not significantly affected by its environment due to very low thermal conductivity. Although the increase in displacement during actuation was smaller due to the additional layer and greater structural stiffness, the slope was fairly linear and consistent even after 50 s of actuation. Unlike the single-walled structure, continued heating was expected to further increase its displacement. During cooling, Peltier cooling decreased cooling time by ~60% versus simply turning off power for air cooling. The double-walled structure was actuated and actively cooled three times, and the results are plotted in figure 5(c). The overlaid results show that the method performed consistently and was repeatable.

These results show several benefits of combining thermoelectric devices with double-walled structures that are actuated underwater. First, the low thermal conductivity of the soft walls enhances actuation by reducing heat loss. When heat dissipation is significant, the system quickly reaches thermal equilibrium, where the input power is the same as heat loss. Second, change in environment has little effect on actuation performance. This is especially important when the system is deployed in unpredictable situations. Last, the thermoelectric device can effectively improve the cooling process. While fabricating the entire structure with double-layered walls can improve actuation, water cooling will take longer due to its low thermal conductivity. This can be resolved by actively cooling the system with a thermoelectric device.

2.5. Anemone demonstration

A soft Dragon skin FX-Pro structure in the form of an anemone was fabricated to mimic its movements and to validate rapid actuation. Anemones in nature use their muscles to open/close its tentacles,[88] burrow in sand,[89] and even swim.[90] These delicate and complex movements are difficult to imitate with conventional rigid robotics. In this study, the opening and closing motions of the mouth and tentacles were demonstrated by inflating the soft structure. Figure 6(a) shows a 3D-printed PLA mold used to fabricate the top tentacle layer. First, uncured Dragon skin was left at room temperature for ~15 min until it became viscous. Then, the mold was dipped in the mixture to create a uniform layer around its surface. A heat gun was used to rapidly cure the elastomer, and the process was repeated twice to fabricate a durable layer. Finally, the elastomer was stretched and peeled off the mold.

The cross-section of the anemone structure is shown in figure 6(b). A separate hollow cylindrical structure was fabricated and sealed with the tentacle layer on top. Similar to the cuboid structure, both single-walled and double-walled artificial anemone structures were fabricated for comparison. The same thermoelectric device was installed at the bottom layer, and 2 ml of ethanol was injected into the chamber.

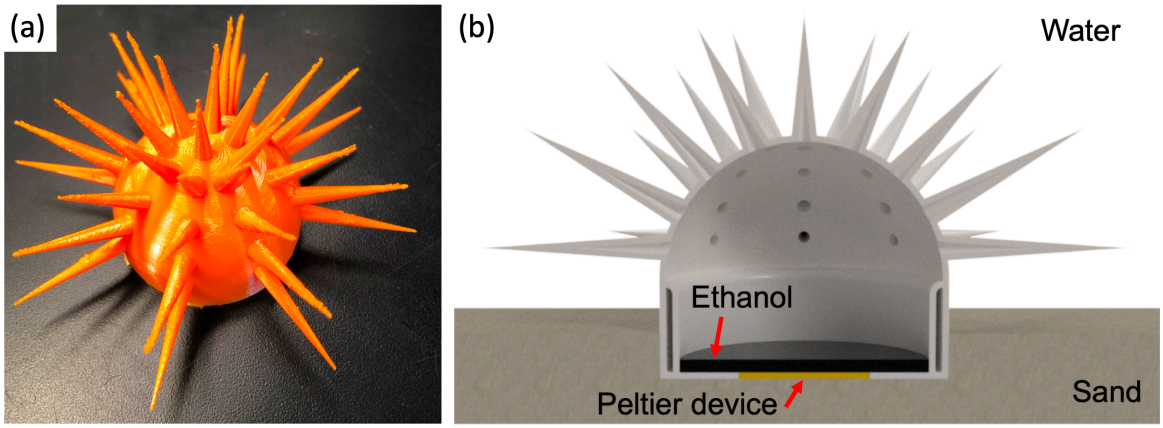

Figure 6. (a) A mold was 3D-printed to fabricate the top tentacle layer of the artificial anemone. (b) The illustration shows the cross-section of the fabricated double-walled anemone, which was partially burrowed in sand underwater.

Figure 7 shows the anemone structure that was partially burrowed into the sand underwater. Since the sand was also wet, it still functioned as a proper heat sink. Here, 5 V was applied to the system during actuation to heat the embedded ethanol. The applied voltage effectively heated the structure through a combination of Peltier effect and joule heating. After actuation, the device was either turned off for water cooling, or current was reversed for active Peltier cooling. While cooling the structure with the thermoelectric device, voltage was reduced to 2.5 V to prevent excessive joule heating. When actuating the single-walled structure, inflation slowed and stopped before full deployment. This was consistent with the previous test, where the displacement change of the cuboid structure slowed down due to greater heat loss. On the other hand, the double-walled structure fully inflated until the tentacle layer was completely actuated after ~60 s. During cooling, Peltier cooling was significantly more effective while reducing cooling time by ~55% versus ambient water cooling. Overall, the results confirmed the viability of the proposed actuation and cooling method for soft robotic structures underwater.

2.6. Conclusions

This chapter addresses the importance of thermal conductivity when actuating soft structures through liquid vaporization, while demonstrating a method that improved both the actuation and cooling processes underwater. In underwater environments, heat loss has a significant effect on actuation by phase transformation. While this can be solved by fabricating double-layered walls, the low thermal conductivity will also slow down the cooling process. In order to improve the reverse actuation process, a thermoelectric device was used to actively cool the system. FE modeling results showed how the double-walled structure reduced heat loss while simultaneously increasing the displacement during inflation when the wall thicknesses were kept the same. When testing the fabricated structures, the thermoelectric device was used to heat and cool the system. The actuation speed of the single-walled structure underwater decreased rapidly due to significant heat loss. On the

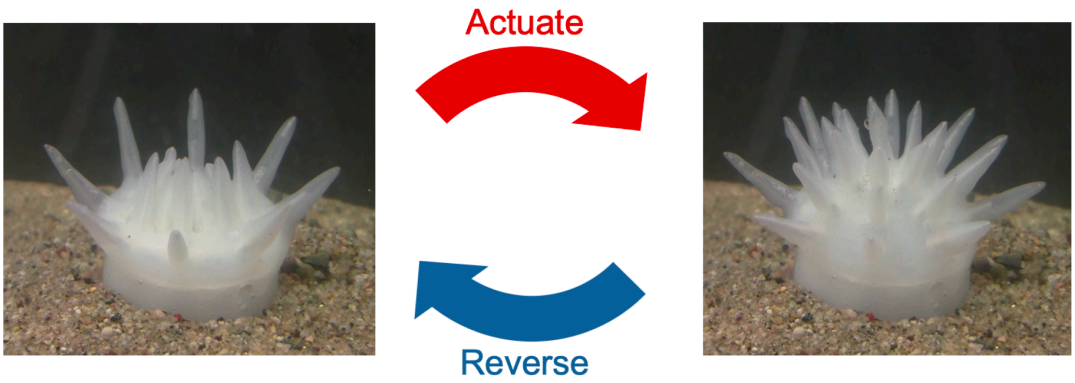

Figure 7. The artificial anemone structure was actuated and cooled to mimic the opening and closing motion of its biological counterpart.

other hand, the double-walled structure showed more stable actuation, and cooling down the system by Peltier cooling reduced the required time to less than half as compared to water cooling. This was achieved by simply reversing current flow, and the method does not require an additional power source for cooling. While most studies implement fluidic pumps for underwater applications that require precise and rapid movements, they must encase a large and heavy pump that is tethered to the chamber. Although slower, actuation through vaporization only requires a small heater that is connected to a power source. The proposed method opens new possibilities to apply actuation through vaporization in unpredictable or harsh surroundings, especially underwater, where the liquid significantly hinders the heating process.

2.7. Acknowledgments

Chapter 2, in full, is a reprint of the materials as it appears in Liquid vaporization actuated soft structures with active cooling and heat loss control, Smart Materials and Structure 30 (2021) 055007, H.-J. Lee and K.J. Loh. The dissertation author was the primary investigator and author of this paper. This work was supported by the U.S. National Science Foundation under Grant No. CMMI-1762530. Additional support was provided by the Jacobs School of Engineering, University of California San Diego.

Chapter 3. Actuation through Ultrasonic Atomization

3.1. Introduction

This chapter aims to utilize ultrasonic waves that propagate through structures to develop untethered actuation methods. In addition, ultrasonic atomization increases the evaporation rate even at substantially lower temperatures. When a layer of liquid is excited by ultrasonic waves, small droplets are ejected from the surface of the liquid into the surrounding air. The small size of the droplets in the mist enables much faster evaporation as compared to bulk liquid. The technique was first presented by Wood and Loomis,[91] and Lang[92] later determined the relationship between droplet size and wave properties. The benefit of using ultrasonic waves over traditional pneumatic atomization is that the droplet size can be easily controlled by adjusting the properties of the wave without affecting the mist density. In general, increasing the frequency of the ultrasonic wave results in smaller droplet sizes.

Atomization is already applied in various fields due to these characteristics, especially when precise control of droplet size is critical. Nebulizers apply ultrasonic waves to atomize liquid medicine into mist.[93] The small droplets of drugs are then inhaled by patients through a connected mask or mouthpiece. Electrostatic coating atomizes the substance that should be coated onto a surface.[94] The small droplets are negatively charged so that they can uniformly coat a positively charged surface. Ultrasonic atomization is also applied in areas where faster evaporation is needed. Small particles can be produced by atomizing solutions of components dissolved in solvents.[95] The solvents in the droplets are then dried to obtain small particles of certain sizes. Increasing the humidity through atomizing water can also be applied for dust control in underground mines.[96]

The goal of this study is to introduce a novel method of soft material actuation based on ultrasonic-wave-induced phase transformation of liquid embedded in patterned soft materials.[97] Different types of deformations, namely unidirectional extension and bending, were demonstrated, and the effects of atomization on actuation were also characterized. In short, hollow structures were

fabricated from soft elastomers with small amounts of ethanol inside. The embedded ethanol was then atomized by propagating ultrasonic waves into the entire soft structure. Instead of raising the temperature to boiling, the small ethanol droplets enabled rapid vaporization into its gas phase. The phase change increased the pressure inside the structure and resulted in actuation. Two different types of deformations were demonstrated by purposefully designing and patterning the structures. An accordion-like structure was fabricated to demonstrate unidirectional deformation. Bending deformation was validated by implementing pneumatic networks (PneuNets) into the soft structure.[24] Then, reversible back-and-forth bending was validated by combining and bonding together two identical bending structures facing in opposite directions to one another. This paper starts with an introduction of ultrasonic atomization. Then, the fabrication method of the structures is discussed, followed by the experimental setup for actuation and characterization. Last, the effect of evaporation and atomization were measured separately to show how much atomization enhances actuation performance as compared to simply heating and evaporating bulk ethanol.

3.2. Atomization background

Ultrasonic atomization is a method that can generate small droplets by propagating ultrasonic waves into a layer of liquid.[91] There are two different hypotheses that explain how these small droplets are generated. The cavitation hypothesis indicates that cavities are formed in the liquid when ultrasonic wave is applied.[98] When these cavities collapse near the liquid surface, small droplets are ejected. The capillary wave hypothesis explains that the droplets are formed when the capillary wave on the surface of the liquid becomes unstable.[92] Various studies were conducted to test both hypotheses, and several studies concluded that both cavities and capillary waves contribute to atomization.[99-101] Nevertheless, the capillary wave hypothesis established a strong correlation between the mean droplet size and the excitation frequency, which is still widely used in the field of atomization.

Figure 8 illustrates how capillary waves result in the ejection of small droplets. Initially, a layer

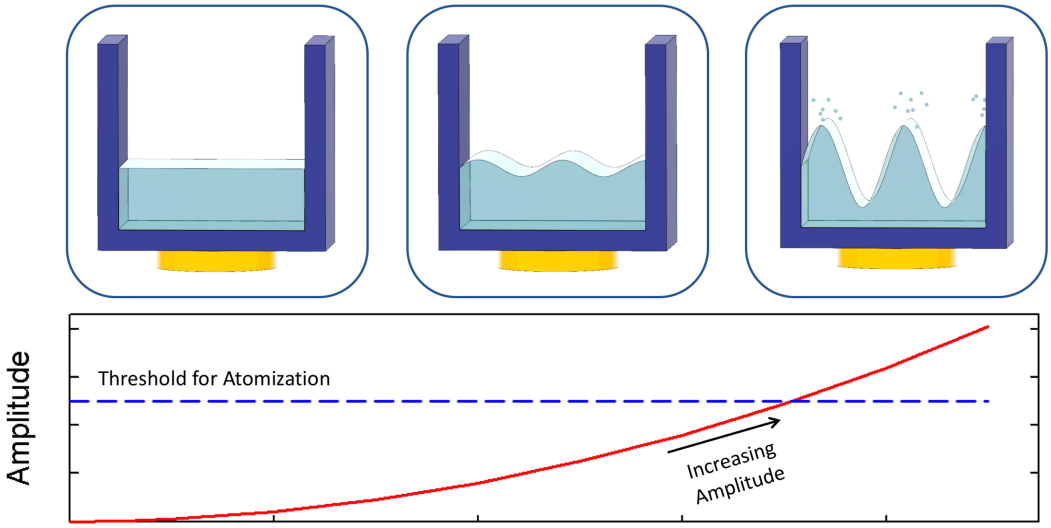

Figure 8. The illustration shows the process of ultrasonic atomization, where a layer of liquid is placed above an ultrasonic transducer. The surface of the liquid stays stationary when the transducer is off (*i.e.*, amplitude is zero). When ultrasonic waves are propagated, capillary waves form on the liquid surface. As the amplitude of the ultrasonic wave increases, a critical point is reached when small droplets are ejected from the crests of the capillary waves.

of liquid is placed above an ultrasonic transducer. When the transducer is turned off and does not generate any waves, the surface of the liquid remains stationary. If the transducer is turned on, the surface of the transducer vibrates, creating ultrasonic waves that propagate perpendicular to the surface. As a result, capillary waves are formed at the liquid-air interface. The amplitude of the capillary waves changes in tandem with the amplitude of the ultrasonic wave. However, a critical point is reached when the capillary wave is no longer stable due to its high amplitude. The surface at the crests start to collapse, which results in small droplets being ejected into the air. Since atomization is related to the stability of the liquid surface, surface tension and density of the liquid also play an important role.

As mentioned earlier, the size of the droplets can be controlled with uniform size by adjusting the applied ultrasonic wave. Lang[92] described the relationship between the frequency of the applied ultrasonic wave and the size of the droplets. First, the wavelength of the capillary wave can be calculated from:

$$\lambda^3 = \frac{2\pi T}{\rho f^2} \tag{4}$$

where λ is the wavelength of the capillary wave, T is surface tension, ρ is density of the liquid, and f is surface wave frequency. Here, f is half of the excitation wave frequency, F.[102] Since the droplets are generated from the crests of the capillary wave, median droplet diameter, D, is a function of λ. The droplet size can be calculated using:

$$D = 0.34\left(\frac{8\pi T}{\rho F^2}\right)^{\frac{1}{3}} \tag{5}$$

There are two effects that need to be considered during actuation through atomization. The first is the rapid evaporation rate of the small droplets as compared to its bulk form. Since the method involves expanding the structure through liquid to gas phase change, faster evaporation will result in faster actuation rates. The second effect is the evaporation of the bulk liquid throughout the process.

When ultrasonic waves propagate through the structure, ultrasonic heating naturally increases temperature. In this study, the effects of atomization and evaporation will be measured separately to evaluate how atomization improves actuation performance of soft structures.

3.3. Characterizing actuation through ultrasonic atomization

3.3.1. Fabrication

Two different soft structures were fabricated to achieve different types of deformations. The first structure was designed to have an accordion-like shape that expands unidirectionally. The second structure was fabricated to have PneuNets of channels to realize bending motion. Both structures were fabricated from FX-Pro elastomer (Smooth-On Inc.), since it is capable of sustaining large amounts of deformation and is suitable for soft robotics. The silicone rubber was prepared by hand-mixing two parts (Part A and Part B) with a 1:1 weight ratio. The mixture was then placed in a vacuum chamber before being cured in room temperature.

First, the fabrication procedure of the unidirectional structure is illustrated in figures 9(a) to 9(c). Figure 9(a) shows a 3D-printed mold for fabricating elastomer strips. The molds were printed using Ninjaflex, a flexible filament, to facilitate removal of the strips. The silicone mixture was then poured into the mold to form a semi-circular strip and was degassed before curing began. After curing, the two ends of the strip were bonded together with the same uncured mixture of FX-Pro to form a truncated cone-shaped structure. As shown in figure 9(b), this process was repeated until four of the same structures were stacked on top of one another. More uncured FX-Pro was applied to form a strong bond between the truncated cone shaped structures. Figure 9(c) is an illustration of the final structure, where thin aluminum sheets were used to seal the top and bottom openings. Thin metal sheets were selected, because they are lightweight and allow the ultrasonic wave to propagate through with little attenuation. Forming a strong bond between the elastomer and the aluminum sheet was crucial too, and this was achieved by folding

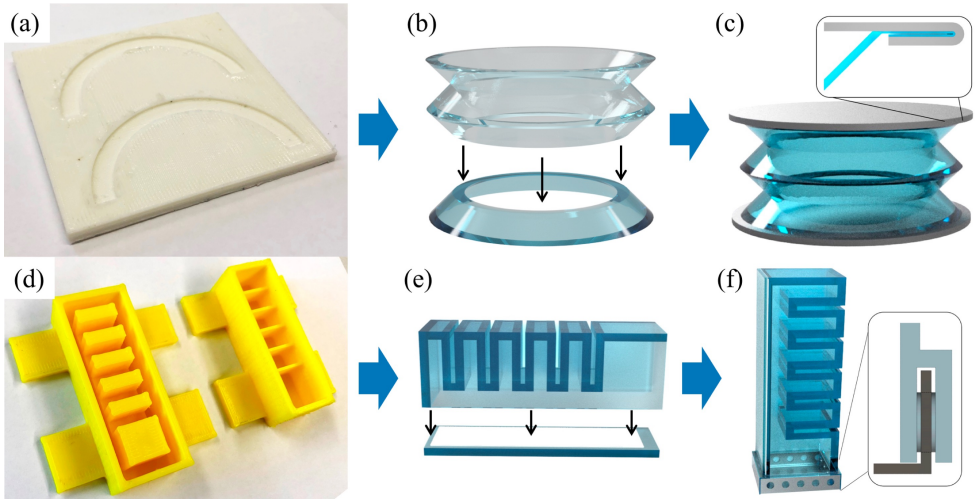

Figure 9. (a) A picture of a 3D printed mold for the unidirectional structure is shown. (b) Bonding the two ends of the strip resulted in a truncated cone structure that can be stacked on top of one another. (c) The edge of the aluminum sheet was folded onto the elastomer to ensure a tight seal. (d) A two-piece mold was 3D printed for fabricating the bendable structure. (e) A piece of paper was embedded in the bottom layer of the elastomer before sealing the bottom side of the structure. (f) The illustration shows the aluminum sheet that was bonded with the elastomer for complete sealing.

the edge of the aluminum sheets so that the metal layer held the elastomer in place.

Second, figure 9(d) to 9(f) illustrate the fabrication process of the PneuNets bending structure. Figure 9(d) shows a 3D-printed two-piece mold made of polylactic acid (PLA). After pouring the uncured silicone rubber into the bottom mold, it was degassed slowly before carefully placing the top mold. The cured elastomer is shown in the top part of figure 9(e), where the bottom and right side of the structure is still open. A layer of FX-Pro was used to seal the bottom side of the structure, where a sheet of paper was embedded to constrain elongation but still enable bending. This allowed the structure to bend more effectively without having to increase the thickness of the bottom layer. Then, uncured FX-Pro was carefully applied around the layer to bond it with the structure from the mold. Figure 9(f) shows the sealing of the final structure. The edges of the aluminum sheet were folded 90° with equally spaced holes on the sides. Uncured FX-Pro was applied over the aluminum so that the elastomer held onto the structure through the holes. Furthermore, two additional bending structures were fabricated and bonded together with more uncured FX-Pro to demonstrate rapid and reversible bending movements.

It should be mentioned that, before completely sealing the two structures with aluminum sheets, the samples were partially filled with ethanol. Ethanol was selected since it has a high vapor pressure and a low boiling temperature of 78 °C. The amount of ethanol in the accordion and PneuNet structures was ~ 2.5 mL and ~ 1 mL, respectively, so that the height of the ethanol layer were ~ 4 mm for both structures.

3.3.2. Experimental setup

Ultrasonic waves were applied to the test structures to validate actuation through atomization of the embedded ethanol. Figure 10(a) shows the unidirectional sample placed on

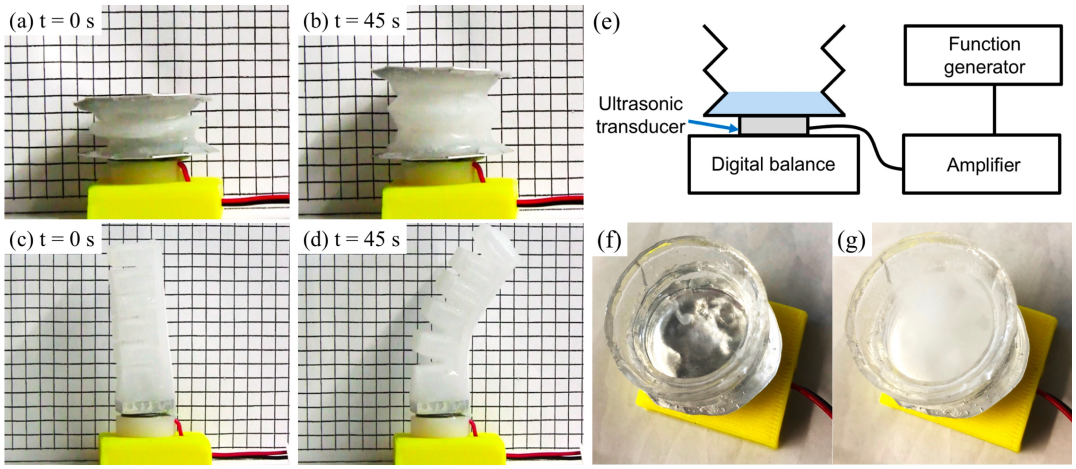

Figure 10. (a) The accordion-like soft structure was placed above the ultrasonic transducer, and, in the background, the grid separation distance is 5 mm. (b) A square wave of 320 V_{pp} and 2.72 MHz was applied to the structure for 45 s, which increased the displacement by ~ 10 mm. (c) A similar setup is shown for the bending structure. (d) The same testing condition resulted in a horizontal displacement of ~ 20 mm. (e) The experimental setup to measure atomization rate is illustrated, where an open-ended structure filled with ethanol was placed above the ultrasonic transducer. The ultrasonic transducer and the structure was placed on a digital balance to measure the weight loss of ethanol during atomization. (f) Applying ultrasonic waves to the open-ended structure resulted in atomization of ethanol. (g) Small droplets are ejected into the air, and, after ~ 30 s, the structure was filled with ethanol mist.

an ultrasonic transducer that was secured in place by a 3D-printed PLA stage. A coupling agent was applied between the sample and the transducer to minimize attenuation at the interface. The overall setup was placed immediately in front of a grid with lines separated by 5 mm. Then, a Keysight 33600A function generator connected to a Ciprian US-TXP-3 voltage amplifier outputted a controlled square-wave signal to actuate the structure. The voltage and frequency were varied to study how these parameters affected actuation performance. In one set of tests, frequency varied from 2.66 MHz to 2.78 MHz in 0.02 MHz increments, while the peak-to-peak voltage (V_{pp}) was fixed at 320 V_{pp}. An actuated unidirectional structure is shown in figure 10(b). In the other set of tests, voltage was varied from 320 V_{pp} to 240 V_{pp} in 20 V_{pp} intervals at a fixed frequency of 2.72 MHz. Videos were recorded throughout the tests to evaluate actuation, where the amount of displacement was quantified through image processing of individual video frames. The same experiments were also conducted using the bending structure, where the images before and after turning on the ultrasonic transducer are shown in figure 10(c) and 10(d).

Similar tests were conducted to measure the increase in pressure of the unidirectional structure. A load cell was fixed in place directly above the structure before actuation so that the pressure was measured at a constant displacement. The frequency dependence was measured under constant voltage of 320 V and the same frequency range of 2.66 MHz to 2.78 MHz. The pressure was also measured with the same decreasing voltage while the frequency was fixed at 2.72 MHz (*i.e.*, 240 V to 320 V).

The next set of experiments were conducted to evaluate how much atomization and evaporation separately contributed to soft structure actuation. Figure 10(e) illustrates the test setup for measuring the weight loss of ethanol due to atomization. An open-ended structure partially filled with ethanol was placed on top of the ultrasonic transducer. The actuation conditions for atomization were the same as the conditions mentioned previously. The transducer was set above a digital balance to periodically measure the weight loss of ethanol during atomization. In addition, temperature changes of ethanol were recorded using a

noncontact infrared thermometer. During this test, the weight of ethanol was recorded for 10 s when the increase in temperature was less than 3 °C. It was assumed that the measured weight loss was only due to atomization without evaporation. Continued atomization would then further increase temperature, and evaporation of ethanol would also start to influence weight loss. However, atomization rate was considered constant even after 10 s, since temperature does not significantly affect surface tension or density of ethanol according to equation (5).

The evaporation rate of ethanol was also measured to study how it affected actuation. First, temperature time histories measured from the aforementioned tests corresponding to different voltage and frequency combinations were used to guide the control of a digital hot plate. The open-ended structure with ethanol was placed on top of the hot plate, while the specimen was heated accordingly and periodically measuring weight. The decrease in weight of ethanol indicated the amount of liquid that evaporated, which would also contribute to expanding the soft structures if they were sealed. These tests were repeated using the sealed samples to measure how much the structures expanded due to evaporation.

3.3.3. Soft structure actuation

The goal of implementing atomization for soft material actuation is to promote liquid-to-gas phase change without significantly increasing the temperature of the embedded liquid. As mentioned earlier, ethanol was filled in two types of different soft structures, namely, one designed for unidirectional extension and the other for bending (figure 10). All of the tests were conducted for 45 s to attain the deformed states as shown in figures 10(b) and 10(d), thereby validating actuation by ultrasonic-wave-induced atomization of ethanol. Figures 10(f) and 10(g) show the same test conducted on a unidirectional soft structure with one end kept opened. It can be observed from figure 10(f) that the propagating ultrasonic waves induced atomization and violent motions of the liquid at the surface. Figure 10(g) shows that continued atomization ejected mist that filled the structure after ~ 30 s. The small droplets or ejected mist then

evaporated. Since evaporation is a surface phenomenon, small droplets evaporate faster than its bulk form due to its high surface-to-volume ratio. The size of the droplets can be calculated from equation (5) and by using an ethanol density of 789 kg/m^3, surface tension of 22.1 mN/m, and the corresponding excitation frequency (*i.e.*, 2.66 MHz to 2.78 MHz). The calculated median droplet diameter is in the sub-micrometer range, which is small enough to consider that the droplets evaporated immediately after being ejected into the air when vapor pressure was still low[103]. It should be mentioned that the tests were stopped at 45 s and well before the equilibrium vapor pressure of ethanol was reached so as to prevent over-deforming and damaging the samples.

Both the unidirectional and bending soft structures were actuated using the ultrasonic transducer, where the frequency and input voltage were varied. Vertical displacement was measured for the unidirectional structure, whereas the horizontal displacement of the free-end was measured for the bending structure. Pressure was also measured for the unidirectional structure while the displacement was fixed. Figures 11(a) and 11(b) plot the maximum displacements of the free-end for both types of samples when frequency or voltage was changed, respectively, while keeping the other parameter fixed. Among the frequencies, 2.72 MHz demonstrated the highest deformation rate after 45 s. The unidirectional structure deformed by ~ 10 mm and the horizontal displacement of the bending structure was ~ 20 mm after actuation. Both structures exhibited lower displacements as the frequency deviated from 2.72 MHz. Figure 11(b) shows similar tests that were conducted by decreasing the voltage from 320 V_{pp} to 240 V_{pp} at 20 V_{pp} intervals and at a fixed frequency of 2.72 MHz. Decreasing the voltage resulted in lower displacements. Pressure of the unidirectional structure measured under the same testing conditions are also plotted in figures 11(a) and 11(b). Similar to the displacement, the maximum pressure reached ~1300 Pa when the transducer was actuated with 2.72 MHz and 320 V_{pp} signals. Increasing or decreasing the frequency resulted in lower pressure, as well as decreasing the voltage.

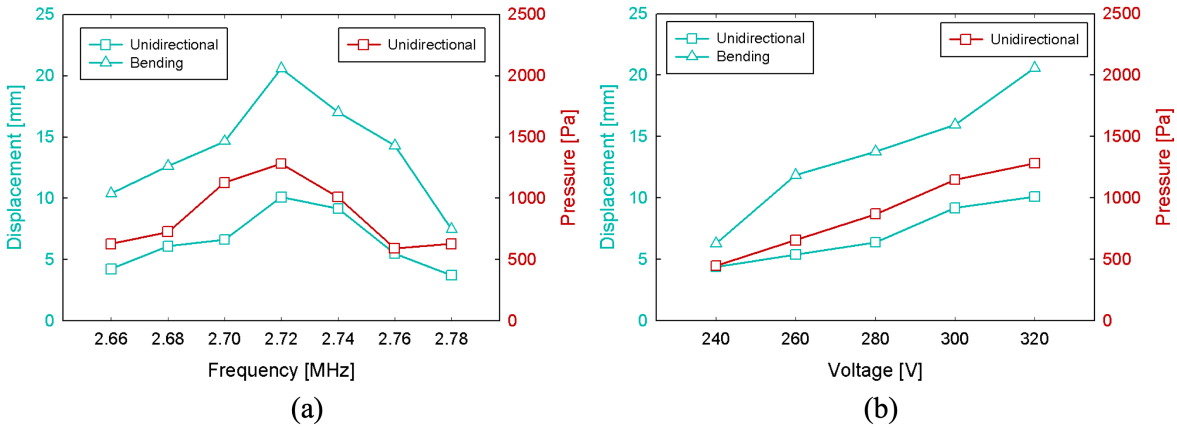

Figure 11. (a) Displacements of the unidirectional and bending samples are plotted against frequency between 2.66 MHz and 2.78 MHz. A constant voltage of 320 V_{pp} was applied, while displacements after 45 s were measured and plotted. Vertical displacement was measured for the unidirectional structure, whereas horizontal displacement was measured for the bending structure. Pressure was also measured at a constant displacement under the same frequency range. (b) Similar tests were conducted with the input frequency fixed at 2.72 MHz, while the input voltage ranged from 240 V_{pp} to 320 V_{pp}.

3.3.4. Effects of ultrasonic atomization

It was also explained that the voltage and frequency of the excitation signals were varied for characterizing actuation performance. The atomization rates for the various testing conditions are summarized in figure 12. Atomization rate was computed by measuring the amount of weight loss of ethanol over a testing period of ~ 10 s. The assumption was that, in the initial 10 s of testing, the temperature change of ethanol was negligible, so mass loss was due solely to atomization.

In particular, figure 12(a) shows the atomization rates when input frequency ranged from 2.66 MHz to 2.78 MHz at a constant voltage of 320 V_{pp}. It is well known that ultrasonic transducers resonate at a certain frequency, which generates the highest amplitude. The amplitude generally decreases as the excitation frequency deviates from its resonant frequency. A similar trend is shown in figure 12(a), where 2.72 MHz exhibited the highest atomization rate. Frequencies beyond the plotted conditions did not generate enough amplitude to atomize ethanol. On the other hand, figure 12(b) shows the atomization rates when the input voltage ranged from 240 V_{pp} to 320 V_{pp}, while frequency was fixed at 2.72 MHz (*i.e.*, as was determined based on the previous tests). It is known that increasing the amplitude of the voltage input also increases ultrasonic wave amplitude; this same trend for atomization can be observed in figure 12(b). Overall, the change in atomization rate indicates how adjusting input voltage and frequency affected the maximum displacements obtained (*i.e.*, after the same amount of time), as well as the actuation rate or speed of the soft structure.

3.3.5. Effects of temperature-induced evaporation

Since atomization does not boil ethanol, only evaporation contributes to atomization-induced phase change. Thus, to study the contributions of temperature-induced evaporation, open-ended soft structures partially filled with ethanol were prepared. Ultrasonic waves were

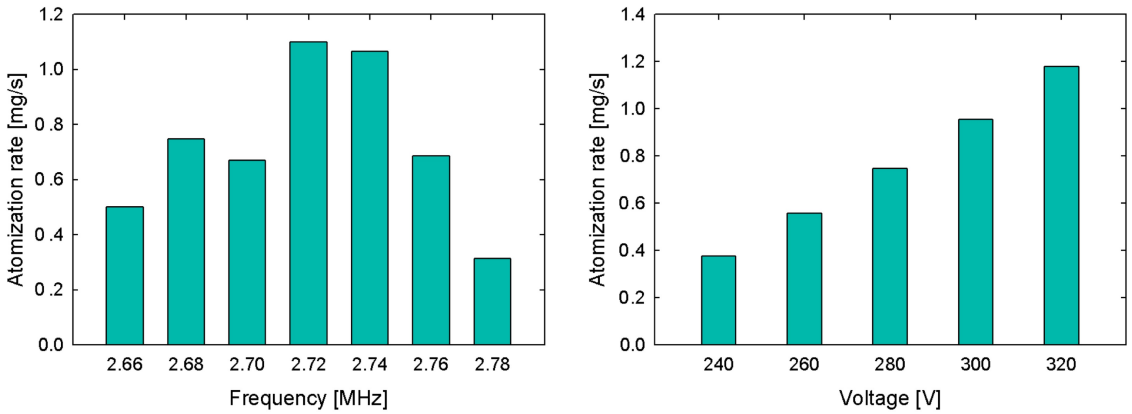

Figure 12. (a) Atomization rate was measured, while the ultrasonic transducer was excited with a voltage of 320 V_{pp} and frequency ranged from 2.66 MHz to 2.78 MHz. (b) Input voltage was controlled from 240 V_{pp} to 320 V_{pp} to study the effects on atomization rate, while frequency was set to 2.72 MHz.

applied to the structure with the aforementioned conditions, while temperature was measured and plotted in figures 13(a) and 13(b). Similar to the atomization rates shown in figure 12, 2.72 MHz and 320 V_{pp} demonstrated the highest temperature change. A digital hot plate was employed to heat the sample in a manner similar to how the sample heated up during ultrasonic atomization. Figures 13(c) and 13(d) summarize the weight loss of ethanol due to temperature-induced evaporation corresponding to different frequency and voltage conditions. The decrease in weight of the sample was strictly due to ethanol that evaporated from liquid to gas and then escaping to the ambient atmosphere due to the use of open-ended test samples. First, for samples where voltage was fixed at 320 V_{pp}, figure 13(c) shows that all frequency conditions showed a similar weight loss until ~ 20 s; major differences became clearly visible after 45 s of testing. In general, conditions that induced higher atomization rates (figure 12a) resulted in higher temperature changes, thus causing greater weight loss of ethanol as shown in figure 13(c). Second, the weight loss of ethanol due to temperature changes corresponding to tests conducted with different excitation voltages is plotted in figure 13(d). Overall, the results are similar to figure 13(c), where the difference in weight loss became more apparent after ~ 20 s. In addition, higher applied voltages resulted in higher weight loss, which was expected.

3.3.6. Atomization versus evaporation

The total weight loss of ethanol after 45 s was studied and compared to weight loss due to atomization and temperature-induced evaporation. The atomization rate was assumed to be constant throughout the actuation period of 45 s. The total weight loss of ethanol due to both atomization and evaporation for various conditions were considered and plotted in figures 14(a) and 14(b). Figures 14(a) shows the weight loss of ethanol, while the input frequency varied from 2.66 MHz to 2.78 MHz and at a constant voltage of 320 V_{pp}. The total weight loss reached a maximum value of 66 mg at 2.72 MHz and decreased to a minimum value of 20 mg at

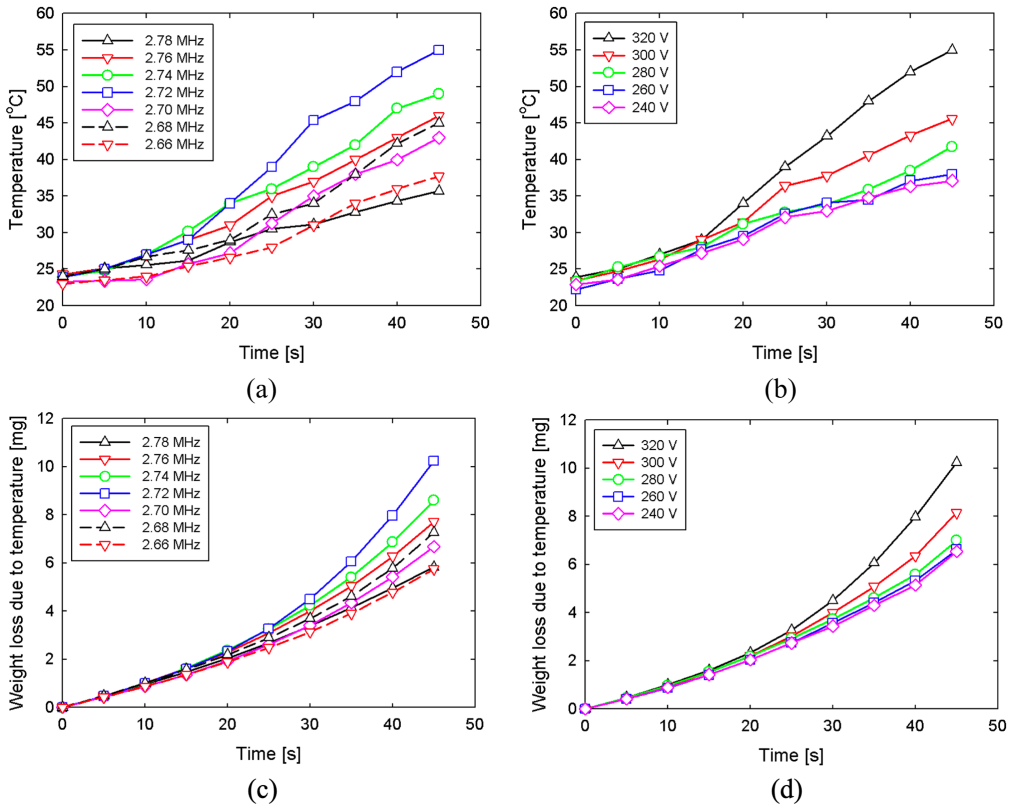

Figure 13. (a) Temperature change was measured and plotted, while the unidirectional structure was actuated with a constant input voltage of 320 V_{pp} and input frequency from 2.66 MHz to 2.78 MHz. (b) Temperature change was plotted, while the structure was actuated with input voltage from 240 Vpp to 320 Vpp and constant frequency of 2.72 MHz. The evaporation of ethanol was measured by employing a hot plate to heat the same structure in a similar manner. (c) The weight loss of ethanol was determined and plotted over the 45 s duration of testing. Results for different frequencies of excitation ranging from 2.66 MHz to 2.78 MHz kept at constant voltage of 320 V_{pp} are shown. (d) A similar set of tests was conducted except that voltage varied between 240 V and 320 V_{pp} with frequency kept constant 2.72 MHz.

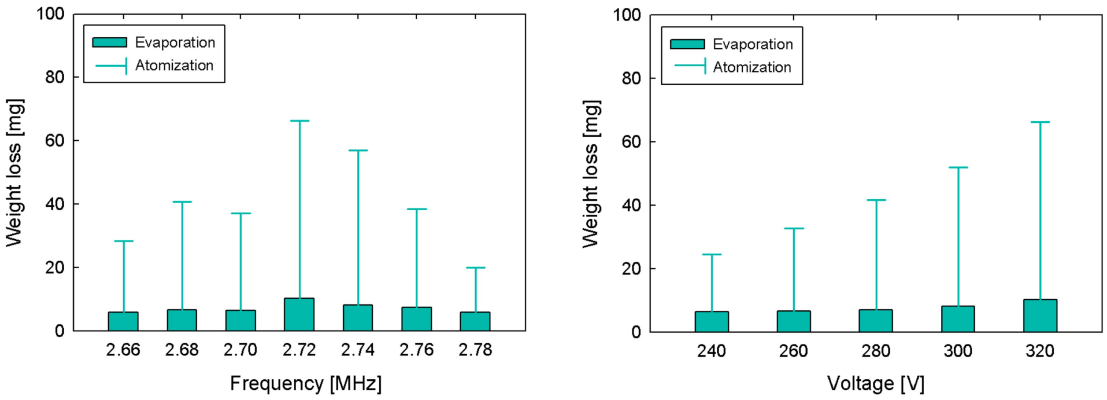

Figure 14. The total weight loss of ethanol after 45 s of testing was characterized based on the effects of both atomization and evaporation. The weight loss due to evaporation was first plotted, followed by adding weight loss due to atomization. (a) The weight loss of ethanol is plotted for different frequency cases while maintaining an input voltage of 320 V_{pp}. (b) Similar tests were conducted to measure weight loss, while input voltage ranged from 240 V_{pp} to 320 V_{pp} with a constant frequency of 2.72 MHz.

2.78 MHz. Figure 14(b) plots weight loss with respect to voltage varied from 240 V_{pp} to 320 V_{pp} but at a fixed frequency of 2.72 MHz. The maximum value of 66 mg at 320 V_{pp} decreased with decreasing voltage and reached a minimum value of 25 mg at 240 V_{pp}. In general, weight loss due to atomization was much greater than the weight loss due to temperature-induced evaporation.

When the soft structures were excited by the ultrasonic transducer, the total weight loss and displacement are due to the combined effects of atomization and evaporation. In order to compare the relative change in total weight loss and displacement over different conditions, both results were normalized with respect to their maximum values. The normalized values (N_{norm}) were calculated using:

$$N_{norm} = \frac{N}{N_{max}} \tag{6}$$

where N_{max} is the maximum value, and N is the measured value when tested with different conditions. The normalization was applied to total weight loss, temperature-induced weight loss, and displacement. From figure 14(a), it was found that the maximum total weight loss of ethanol was 66 mg when frequency was 2.72 MHz. Thus, the total and temperature-induced weight loss values for each frequency condition was divided by 66 mg to obtain their corresponding relative weight loss of ethanol. Figure 15(a) compares the relative weight loss and displacement over a range of frequencies at a fixed voltage of 320 V_{pp}. It can be seen that atomization-induced weight loss was as high as ~ 4.5 times greater than weight loss due to evaporation at 2.72 MHz. This ratio generally decreased as the frequency deviated from 2.72 MHz.

A similar normalization was performed on the displacement results of the unidirectional and bending structures shown in figure 11. During actuation by the ultrasonic transducer,

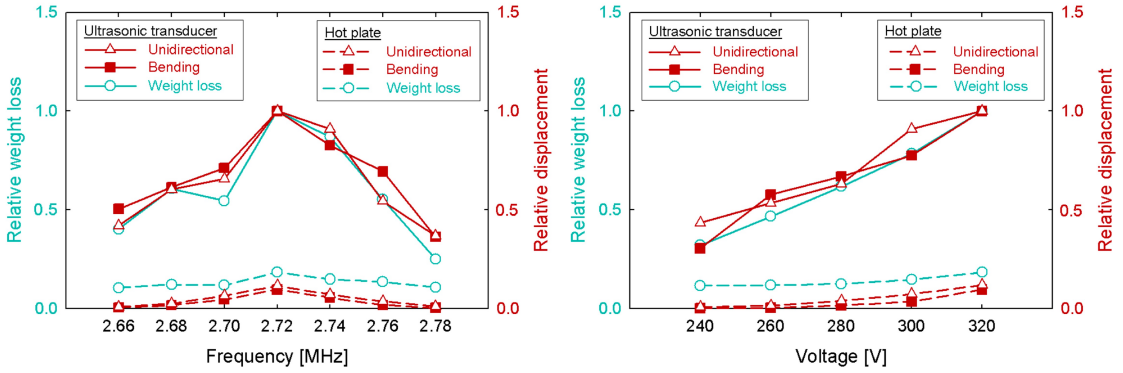

Figure 15. Relative weight loss was compared with relative displacement for different testing conditions. The results from the ultrasonic transducer indicate weight loss and displacement due to atomization and evaporation. Effect of evaporation alone was measured by heating the structure with a hot plate. The temperature of the hot plate was controlled following the temperature time histories in figure 13(a) and 13(b). Relative value for each condition was calculated by dividing the results by the maximum number. (a) Relative weight loss and relative displacement is plotted versus the frequency of excitation. (b) Relative weight loss and relative displacement are plotted as a function of input voltage. All the results indicated that temperature-induced evaporation only contributed a small fraction of the total actuated response of the soft structure.

unidirectional and bending structures reached a maximum displacement of ~ 10 mm and ~ 20 mm, respectively. Thus, the displacement due to the ultrasonic transducer and direct heating for each frequency condition was divided by these maximum values to compare their relative change. In case of actuation by the ultrasonic transducer, the relative decrease in ethanol weight loss and displacements of the two structures followed a similar trend. This indicated that total weight loss, which was mostly due to atomization, plays an important role in actuating the structure. The displacements of both structures deformed by temperature-induced evaporation (*i.e.*, by the hot plate) were significantly lower, which were both ~ 10% of the displacements induced by atomization. As the frequency deviated from 2.72 MHz, the displacements due to evaporation were almost negligible.

The results for relative weight loss and displacements as the excitation voltage was varied is shown in figure 15(b). Again, the maximum weight loss and displacement values were used to normalize the results shown in figure 11(b) and figure 14(b) to generate figure 15(b). The general decreasing trends of relative weight loss and displacement were similar as the voltage decreased. Similar to figure 15(a), decreasing the voltage reduced the contribution of atomization to the total weight loss. In case of results from the ultrasonic transducer, decreasing the voltage to 240 V_{pp} reduced the displacement to ~ 40% for both structures. Displacements of the structures placed on the hot plate also decreased with decreasing voltage and were almost negligible at 240 V_{pp}.

3.4. Actuation performance

3.4.1. Experimental setup

To characterize ultrasonic-atomization-induced soft structure actuation, a cuboid structure was actuated for ~ 20 s. The simple geometry enabled easier analysis of deformation. Figure 16(a) shows a similar setup, where the bottom metal sheet was placed above the

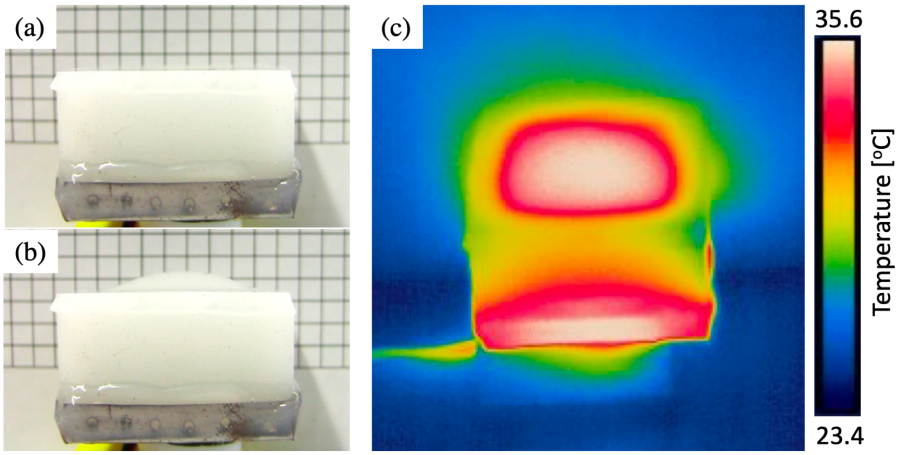

Figure 16. (a) The fabricated structure was placed on top of a piezoelectric disc. (b) The displacement of the top layer reached ~ 5 mm after 20 s of actuation. (c) The image shows a temperature distribution of the structure after 20 s, and the maximum temperature was ~ 36 °C.

ultrasonic transducer. Figure 16(b) shows the deformation of the top layer after ~ 20 s of actuation. In addition, the actuation of the structure was recorded with an infrared camera. The temperature distribution after ~ 20 s is shown in figure 16(c). The high temperature of the bottom layer shows that the metal layer was subjected to ultrasonic heating, which is important when evaporating the ethanol droplets. In an open system, the droplets evaporated even when there was no temperature difference, since vapor pressure was not in equilibrium. However, the evaporation rate and condensation rate of ethanol were already in equilibrium in a closed system. An additional driving force was required for the droplets to evaporate, and this driving force was provided by ultrasonic heating. It is also worth pointing out that the temperature of the top layer was similar to the temperature of the bottom layer. This indicate that the ultrasonic heating from the bottom layer heated the entire cavity, resulting in a uniform temperature distribution within the system.

The videos taken during the experiment was analyzed to plot the displacement and temperature change over time. The video that recorded the displacement of the top layer was analyzed using image processing to plot the displacement change of the top plane. The result is shown in figure 17(a), where the displacement reached ~ 5 mm after ~ 20 s. The maximum temperature from the infrared camera was also recorded over time. The temperature change is plotted in figure 17(b), where the maximum temperature reached ~ 36 °C after ~ 20 s.

3.4.2. Finite element model

Unlike materials that deform linearly (*i.e.*, following Hooke's law), soft materials are often used to sustain large and nonlinear deformations. Materials with such a wide range of elastic response are regarded as hyperelastic, and their stress-strain relation is established from the strain energy function. The second Piola-Kirchhoff stresses, S, are obtained from the partial derivative of the strain energy function, W, with respect to strain.

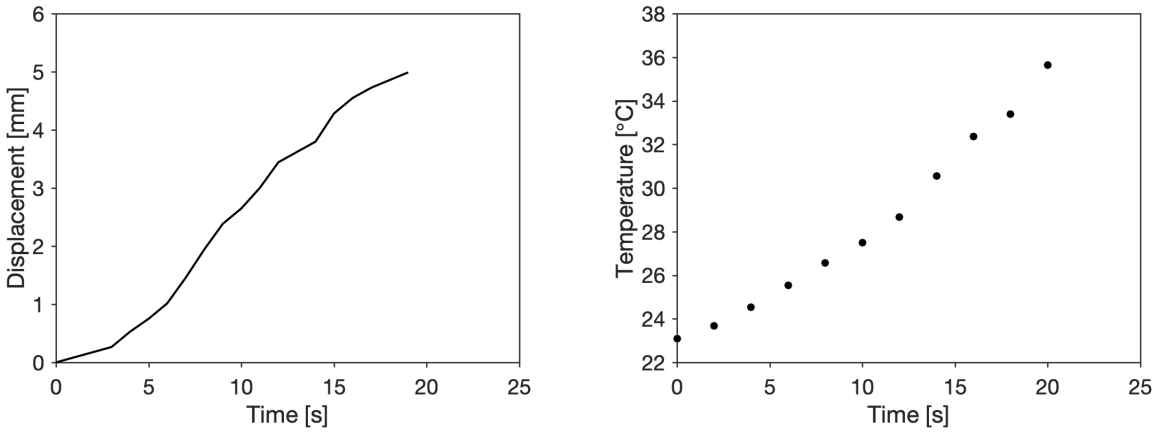

(a) (b)

Figure 17. (a) Image processing was used to measure the displacement of the top layer throughout soft structure actuation. (b) The temperature measured with the infrared camera was plotted with respect to time.

$$S = 2\frac{\partial W}{\partial C} \tag{7}$$

where C is the right Cauchy-Green deformation gradient tensor. The difficulty lies in developing models for the strain energy function W. The Neo-Hookean model is one of the simpler models that assumes the material to deform linearly in the initial stage and becomes nonlinear after a certain threshold. The strain energy density for the Neo-Hookean model is as follows:

$$W = C_1(trace(F^T F) - 3) \tag{8}$$

where C_1 is a material constant, and F is a deformation gradient. The form of the energy is constructed based on the thermodynamic consideration of rubber elasticity, as well as incompressibility. The model is based on statistical thermo- dynamics of rubber-like polymers with crosslinked chains. The model considers the crosslinks to deform in a linear manner, and, upon reaching a threshold, the material is expected to exhibit nonlinear deformation.

The inflation of the structure was simulated by applying the ideal gas law inside the chamber. Increasing the volume of gas inside the chamber applied pressure on the walls and deformed the initial structure. The pressure inside the chamber decreases as the structure inflates, and the relationship was defined through the following equation:

$$\frac{P}{P_0} = \left(\frac{V_0}{V}\right)^{\gamma} \tag{9}$$

where P is pressure of gas, V is volume, γ is the specific ratio of heat, and the subscript, 0, denotes the initial condition.

The overall simulation was conducted using *COMSOL*. The geometry and configuration of the problem were modeled in accordance with the experimental conditions. A 3D structure with a cavity was modeled as a solid, which was discretized predominantly by tetrahedron meshes. It was assumed that the structure was clamped at its bottom, where increasing the volume of gas inside the chamber inflated and deformed the enclosed cavity. The simulation result was compared with the experimental results to analyze the performance of soft structure actuation induced by ultrasonic atomization.

3.4.3. Volume of generated vapor

The simulation result is plotted in figure 18(a), which shows the relationship between the increase in volume within the chamber and the displacement of the top layer. Through this relationship, the displacement of the experimental result shown in figure 17(a) can be converted to change in volume. The result is plotted as a solid line in figure 18(b). Since evaporation is highly related to temperature, the increasing trend of the volume was similar to the temperature plot in figure 17(b).

It is worth pointing out that the system was capable of atomizing ethanol with a rate of ~ 1.7 mg/s in open air. Assuming a situation where 100 % of the generated droplets evaporate immediately, the maximum volume change of the system can be calculated using the ideal gas law. This ideal case is plotted as a dotted line in figure 18(b). The lower volume change during actuation indicates that only a portion of the generated droplets evaporated. Since temperature is highly related to evaporation, providing additional heat is expected to increase volume change during actuation. This result also indicates that increasing the atomization rate will have little effect on increasing the actuation efficiency.

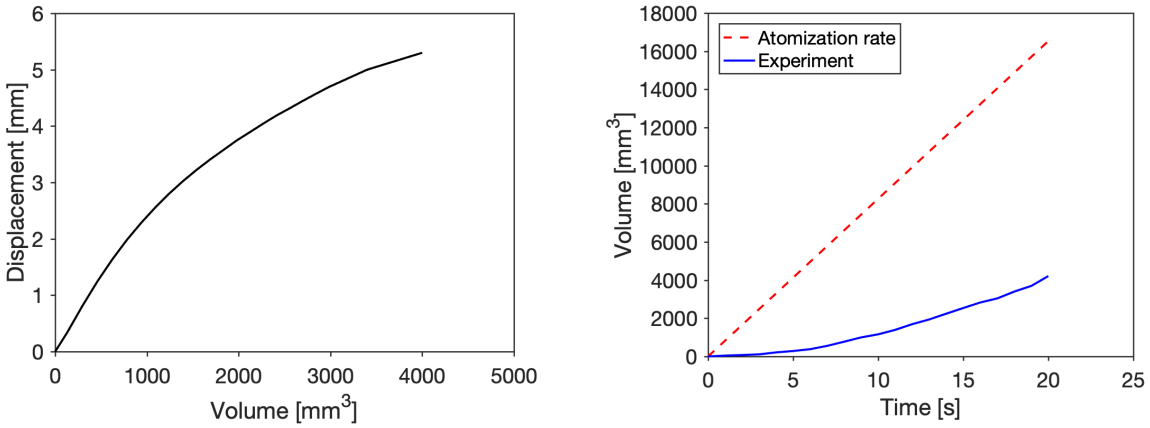

(a) (b)

Figure 18. (a) The hyperelastic and ideal gas models were used to simulate the relationship between the change in volume and the displacement of the top layer. (b) The simulation result was used to estimate the change in volume during the experiment. The dotted line indicates the change in volume of an ideal situation, assuming that all the droplets evaporated immediately.

3.5. Demonstrations

3.5.1. Soft variable buoyancy system

A soft variable buoyancy system (VBS) that resembles a cylindrical accordion-like structure was fabricated by pouring an uncured elastomer in a 3D-printed mold. The three-part mold was 3D- printed with polylactic (PLA) as shown in figure 19(a). The soft structure was fabricated using FX-Pro elastomer (Smooth-On, Inc.) due to its ease of fabrication and capability of undergoing large deformations. Two parts of the uncured elastomer were mixed by hand and subjected to vacuum to remove any air bubbles in the mixture. The three-part mold was assembled after pouring in the uncured FX-Pro, which was then left to rest at room temperature for the silicone rubber to cure. After removing the soft structure from the mold, two thin steel sheets were used to seal the top and bottom openings of the structure as shown in figure 19(b). The two sheets were sealed in place by applying more uncured FX-Pro at the interface. The metal sheet allowed ultrasonic waves to propagate inside the structure with minimal attenuation. During the sealing process, the hollow structure was partially filled with ethanol (~ 5 mL).

The fabricated structure was fixed above an ultrasonic transducer as shown in figure 19(c). A holder for the ultrasonic transducer was 3D-printed with a flexible Ninjaflex filament. The transducer was bonded to the top of the holder using a small amount of uncured FX-Pro, whereas the bottom of the holder was designed to attach weights for testing buoyancy control. Figure 19(d) shows an image of the soft structure fabricated from the mold, and the final assembly of the soft actuator is shown in figure 19(e).

Figure 20 shows the cross-section of the final structure. The ultrasonic transducer was bonded to the bottom holder with an air gap underneath to maximize vibrations generated during actuation. A function generator was connected to an amplifier, which excited the transducer using a 2.66 MHz and ~ 320 V waveform. It should also be mentioned that coupling agent was not required between the transducer and structure. The ultrasonic wave transmitted through

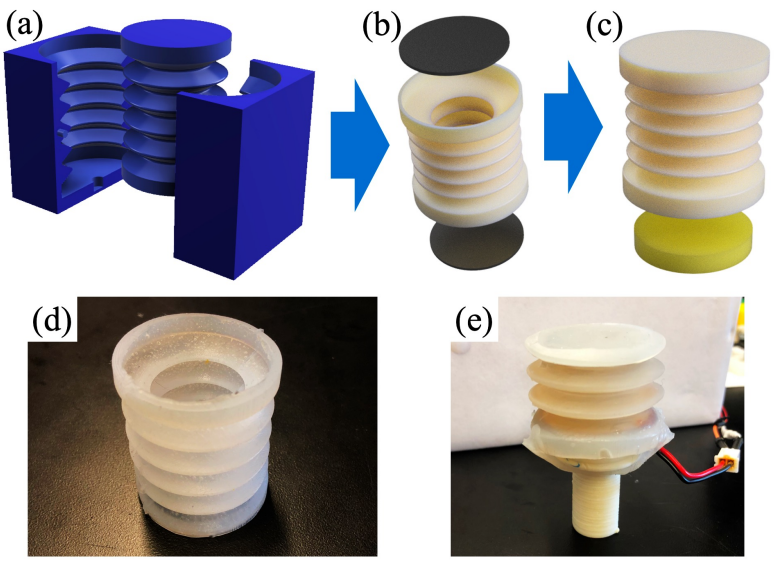

Figure 19. (a) The illustration shows a 3D-printed mold to fabricate the soft actuator. (b) Two ends of the soft structure were sealed with thin metal sheets to minimize attenuation of the ultrasonic wave. A small amount of ethanol was injected into the structure for ultrasonic atomization. (c) The structure was placed above the ultrasonic transducer to atomize the embedded ethanol. (d) The image shows the soft structure fabricated from the mold. (e) The bottom holder with the ultrasonic transducer was connected to the bottom of the soft structure.

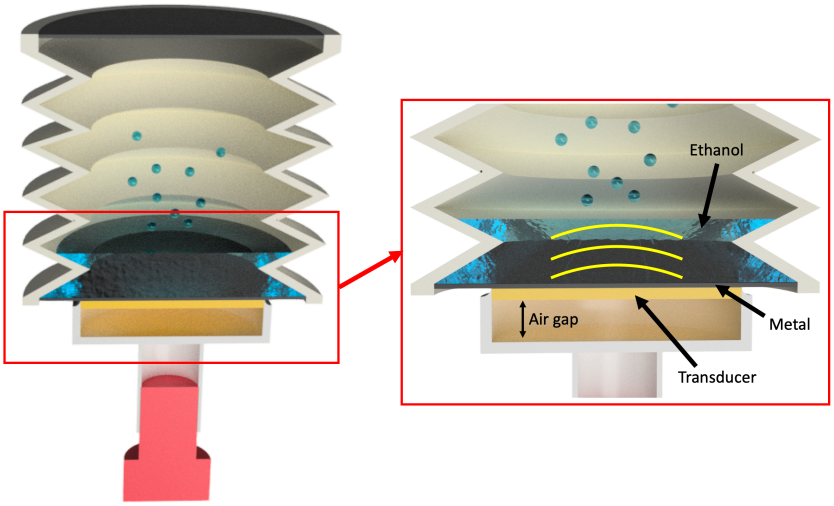

Figure 20. The cross-section of the final structure is illustrated. The ultrasonic transducer was placed beneath the metal sheet. The transducer generated ultrasonic waves that propagated through the metal sheet and atomized the embedded ethanol.

water and the bottom metal layer, which atomized the embedded ethanol into small droplets. The ethanol droplets evaporated and inflated the closed soft structure, which would decrease density and increase buoyancy of the VBS.

The soft VBS was placed underwater with a metal weight fixed at the bottom of the holder. The weight was heavy enough to hold the structure at the bottom of the container during actuation. The initial setup is shown in figure 21(a), and figure 21(b) shows the structure after ~ 100 s of actuation. Video was recorded throughout actuation, and the vertical displacement of the soft structure was quantified through image processing. The displacement time history of the test is plotted in figure 21(c). Displacement increased at a constant rate and reached a plateau after ~ 100 s. The displacement decreased upon turning the transducer off after ~ 130 s. The slope of the displacement decreased with respect to time and required more than 600 s to reach its original state.

Additional tests were conducted to demonstrate repeatability of the soft actuation through ultrasonic atomization. Actuation was repeated three times using the same conditions, and displacement was again determined through image processing. The results of the three actuation cycles are shown in figure 22, and the consistent change in displacement validates reliable buoyancy control for VBS.

The increasing volume of the soft structure during atomization increased its buoyancy, which showed that the method is suitable for VBS. The buoyancy force (F) of the structure was determined using:

$$F = \rho g V \tag{10}$$

where ρ is water density, g is gravitational acceleration, and V is the volume of the displaced body of water. The overall setup was placed on a digital balance to measure its weight,

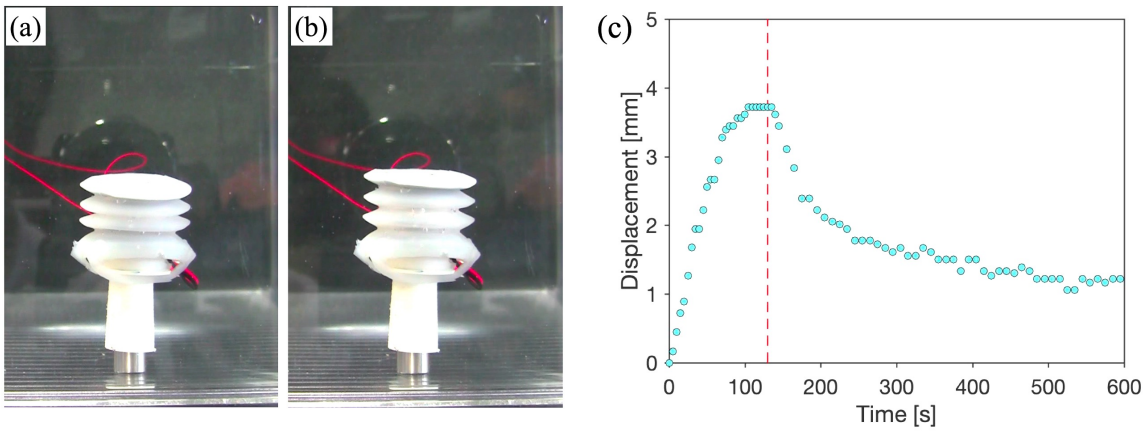

Figure 21. (a) The picture shows the initial setup just prior to actuating the soft structure. A metal weight was fixed to the bottom holder to analyze the vertical displacement of the structure underwater. (b) Vertical displacement of the soft structure reached ~ 3.8 mm after propagating ultrasonic waves for ~ 100 s. (c) The plot shows the displacement of the soft structure over time. Displacement rapidly decreased when the transducer was switched off after ~ 130 s.

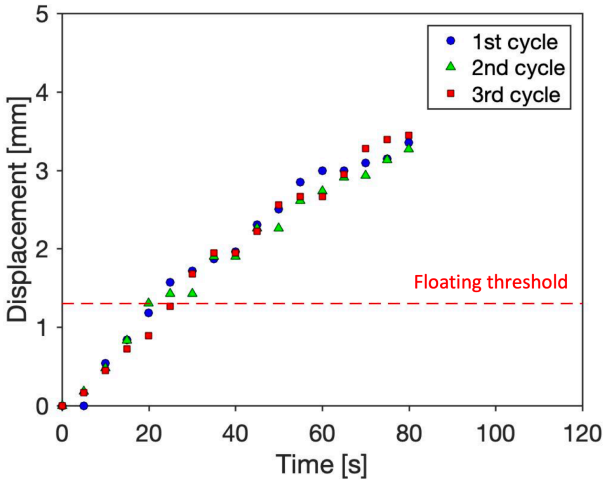

Figure 22. The plot shows the displacement time history corresponding to three cycles of actuation. The dotted line shows the estimated displacement when the structure will start to float.

and the volume of the structure was determined by placing it in a beaker filled with water. The increase in height of the water was used to measure the volume. The weight and volume of the structure was ~ 20 g and ~ 20 mL, respectively. Next, the buoyancy force of the structure was analyzed when a 10 g weight was attached to the bottom of the structure. The displacement required for the structure and the 10 g weight to float is plotted as a dotted line in figure 22.

To demonstrate operations of the soft VBS, the structure was attached to a 10 g weight and placed underneath water. Exciting the ultrasonic transducer atomized the embedded ethanol and inflated the structure, resulting in buoyancy control. Figure 23(a) shows the initial setup, and actuating the structure for ~ 35 s increased the buoyancy as shown in figure 23(b). Similar to the previous experiments, video was recorded throughout testing, and the position of the VBS was determined through image processing. The change in height over time is plotted in figure 23(c). The system started to float after ~ 20 s of actuation, which is in agreement with figure 22. Upon reaching the threshold, the structure floated at ~ 80 mm from the bottom and reached the surface after ~ 15 s. The ultrasonic transducer was turned off after ~ 50 s of actuation, and the structure began to sink after ~ 10 s.

The last test was conducted to float the soft VBS to a targeted height and maintain its position by controlling and modulating atomization. The target height was selected as ~ 60 mm from the bottom, and the results are shown in figure 24. Similar to the previous test, the structure started to float after ~ 20 s, and the ultrasonic transducer was turned off and on for ~ 1 to 2 s to hold its position (or displacement). The structure was successfully maintained at the target height for ~ 10 s. Then, the ultrasonic transducer was continuously actuated again for the VBS to float to the surface. The results show that atomization is capable of controlling buoyancy of the system.

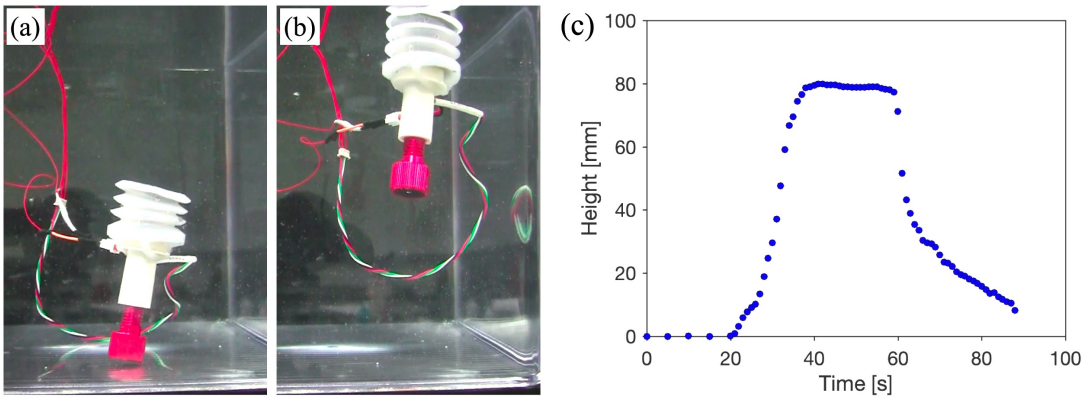

Figure 23. (a) The image shows the soft structure connected to a 10 g weight. (b) The structure started to float after ~ 20 s and reached the surface after ~ 35 s. (c) The plot shows the vertical position during actuation. The transducer was turned off after ~ 50 s.

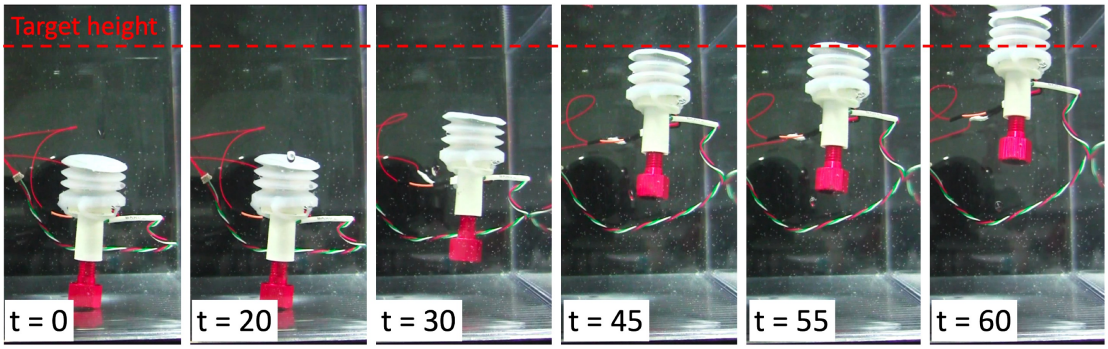

Figure 24. The excitation of the transducer was controlled to maintain the structure at a target height, which is indicated by the dashed red line.

3.5.2. Soft gripper

The well-studied PneuNet structure was chosen to show that actuation through ultrasonic atomization can demonstrate functionality without permanently installing the soft structure in place or attaching tethered tubes. It was shown that bonding the backs of two bending structures resulted in a structure that could achieve reversible back-and-forth motion.[104] Two of these structures were applied as fingers for the soft robotic gripper used in this study. The assembly drawing of the gripper is shown in figure 25(a). The base of the gripper was 3D-printed with a flexible Ninjaflex filament that had four indentations. Magnets were first placed in the indentation so that the steel sheets at the base of the bending structures would be fixed in place. If the transducers were placed directly above the magnets, the magnets pressed up against the bottom surface of the transducer, which hindered its vibration. Therefore, 3D-printed PLA rings were also placed in between the magnets and the transducers so that there was an air gap beneath the transducers for vibration.

The overall structure of the finger was similar to PneuNets from other studies. An illustration of the structure's cross-section is shown in figure 25(b). Thin steel sheets were installed on the side of the base chamber so that laying down the structure resulted in the sheets being on the bottom. Since actuation induced by atomization involves liquid, the base of the structure was designed accordingly. An additional layer of Dragon Skin was added to confine the ethanol at the base, where the ultrasonic wave was applied. A small hole above the layer allowed the evaporated ethanol to inflate the rest of the structure.

The fabricated gripper with two fingers is shown in figure 25(c). It should be mentioned that the soft fingers were untethered from the base of the gripper and held in place with magnets. Installing and detaching the fingers were as easy as simply placing them in place and removing them from the transducers. This untethered setup also allowed replacing the fingers with soft structures of different geometries to achieve various types of motions. Actuating the outer

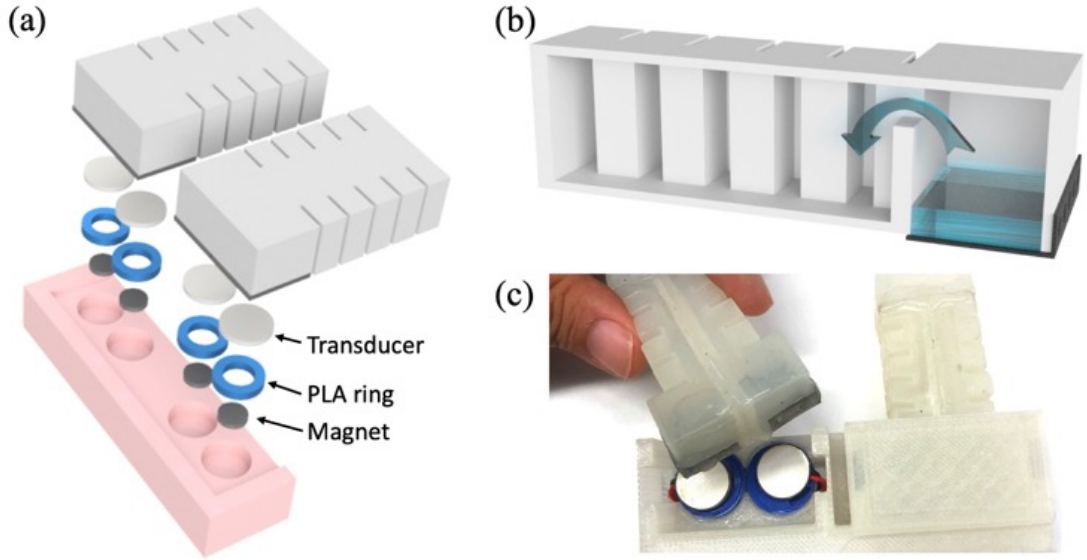

Figure 25. (a) The illustration shows the assembly of a soft robotic gripper. The base was 3D-printed with a flexible material (Ninjaflex), which holds PLA rings that separated the magnets and the ultrasonic transducers. The backs of two bending structures were bonded to achieve back-and-forth motion. (b) The illustration shows the cross-section of the bending structure. A thin layer was included to contain the liquid ethanol at the base. As the ethanol evaporates, gas flows over the layer and inflates the overall structure. (c) The image shows that the soft fingers are actuated by simply placing them above the ultrasonic transducers.

transducers closed the fingers, whereas actuating the inner transducers spread them apart.

The images in figure 26 show the gripper lifting various objects. Each example was selected to represent different types of objects that are generally difficult for rigid robotic systems to handle (*i.e.*, without damaging the target object). Figure 26(a) shows the image of the gripper holding a very thin playing card. A cylindrical pen with a small contact area was used in figure 26(b). The gripper was also capable of holding onto delicate objects such as a strawberry in figure 26(c), as well as a brittle light bulb in figure 26(d). Overall, the results presented in figure 26 successfully validated that ultrasonic atomization could be leveraged to actuate and control soft robotic systems, such as a gripper.

3.6. Conclusions

In this chapter, soft actuation through ultrasonic atomization was analyzed using a numerical model and comparing it with experimental results. These soft structures were partially filled with ethanol, and an ultrasonic transducer propagated ultrasonic waves to atomize the embedded ethanol into small droplets that then inflated the structure. First, it was found that ultrasonic-induced atomization of the embedded ethanol ejected small droplets that enhanced the evaporation rate at temperatures well below boiling. The fast evaporation of the small droplets expanded the structure, which was enough to demonstrate different types of deformation. Their deformation could also be controlled by adjusting input voltage and frequency used to excite the ultrasonic transducer. Second, the contributions of atomization versus temperature-induced actuation to total deformation was assessed using open-ended soft structures. By measuring the weight loss of ethanol over time and due to atomization and heating separately, it was found that the displacements of both structures due to atomization were ~ 10 times greater than displacements induced by evaporation. It was found from experimental tests that the droplets initially evaporated at a slow rate, but the rate rapidly increased with increasing temperature. Furthermore, atomizing ethanol into small droplets demonstrated a much

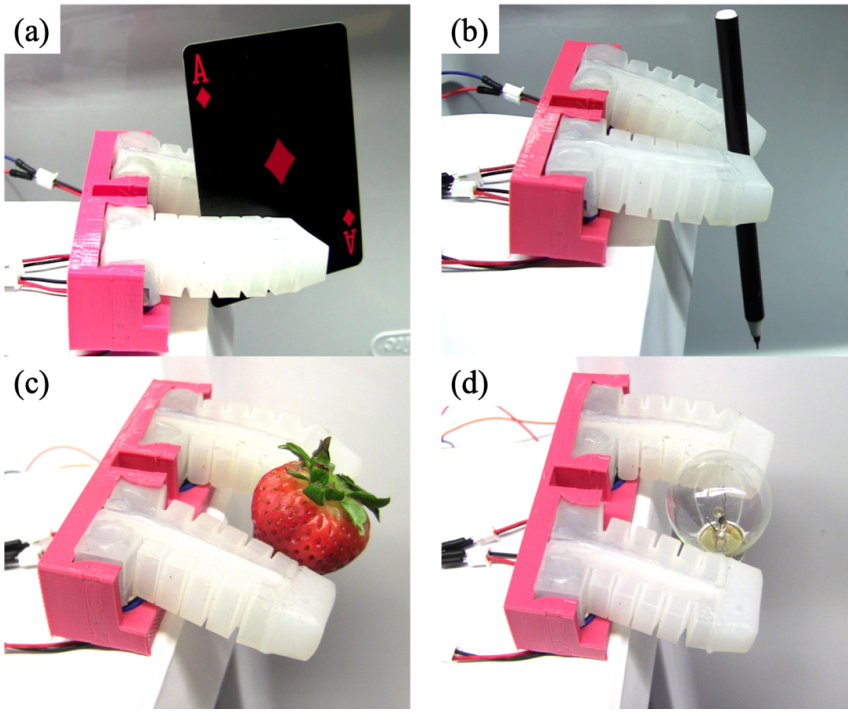

Figure 26. The images show demonstrations of the gripper holding various objects, namely, (a) a playing card, (b) pen, (c) strawberry, and (d) light bulb.

higher evaporation rate as compared to heating the bulk liquid. Overall, the volume change during evaporation was significant enough to actuate the bending structure. In addition to the experiments, *COMSOL* was used to simulate the inflation of the bending structure and to characterize actuation through atomization. The analysis showed that there is room for improvement by providing additional heat. Finally, soft robotic VBS and grippers were fabricated and were successfully validated for functional applications.

3.7. Acknowledgments

Chapter 3, in part, is a reprint of the materials as it appears in Soft material actuation by atomization, Smart Materials and Structure 28 (2018) 025030, H.-J. Lee and K.J. Loh, Characterization of a soft gripper with detachable fingers through rapid droplet evaporation, Proceedings of 3rd IEEE International Conference on Soft Robotics (2020) 83-88, H.-J. Lee, N. Melchor, H. Chung, and K.J. Loh, Soft material actuation and shape-change through ultrasonic atomization, Proceedings of the 12th International Workshop on Structural Health Monitoring, Stanford, CA (2019), H.-J. Lee, N. Melchor, and K.J. Loh, Characterization of soft actuation through ultrasonic atomization, TMS 149th Annual Meeting & Exhibition Supplemental Proceedings, Springer, San-Diego, CA (2020) 881-888, H.-J. Lee and K.J. Loh, and Actuation of soft materials through ultrasonic atomization, Bioinspiration, Biomimetics, and Bioreplication VIII 10593 (2018) 105930Z, H.-J. Lee, M. Funderburk, and K.J. Loh. The dissertation author was the primary investigator and author of these papers. These works were supported by the U.S. National Science Foundation under Grant No. CMMI-1762530. Additional support was provided by the Jacobs School of Engineering, University of California San Diego.

Chapter 4. Actuation through Vibrating Mesh Atomization

4.1. Introduction

This chapter is a continued study from chapter 3, with the aim of improving its performance. While low vapor pressure at a certain temperature considers the equilibrium condition, the time it takes to approach that equilibrium is also critical. The amount of liquid is important when considering this phase transformation kinetics, since the required heat is generally proportional to the mass. This is another reason why a very small amount of liquid is generally embedded when a heater is used to boil the liquid. The method used in chapter 3 bypassed this issue by dispersing the liquid into small droplets through ultrasonic atomization.[104] Very strong ultrasonic waves were applied from the exterior, which propagated through the wall and atomized the embedded liquid. During this process, a small amount of heat was generated at the interface between the wall of the structure and the ultrasonic transducer. The total surface area of the small droplets was large enough to vaporize the liquid even when below the boiling temperature (i.e., through evaporation). However, this method required applied voltages that were as high as 320 V, and the speed of actuation was still much slower than a conventional pneumatic pump.

Therefore, the objective of this chapter is to implement a completely different type of atomization method for improving the performance of actuation through vaporization. Vibrating mesh atomization was employed to drastically lower the required power for atomization. In order to increase vaporization rate, a separate heater with a large surface area was installed above the atomizer. Upon powering the system, the atomizer dispersed small droplets into the air, which vaporized as they passed through the heater. The entire system was enclosed inside a soft elastomer to demonstrate actuation during the vaporization process. This study addresses four limitations of actuation through vaporization. First, the system utilizes evaporation, which does not necessitate high temperatures. This is critical, since most heating elements usually require very high current to heat the system to boiling. Second, much faster actuation speed can be attained by vaporizing small droplets as compared to heating bulk

liquid. Third, actuation speed is independent of how much liquid is stored inside the system. This allows one to maintain actuation speed and simply exhaust the vapor for rapid actuation reversal. Fourth, the setup of the system enables actuation regardless of how much the structure is tilted. This is important since methods that boil bulk liquid only work when the liquid is in the vicinity of the heater.

4.2. Atomization methods

Several methods have been developed to atomize liquid into small droplets. These techniques are implemented in various fields and applications. Pressure atomization generates droplets by discharging liquid through a small orifice.[105] If the pressure drop is sufficiently high, the jet of liquid disintegrates into small droplets. This method is widely used in internal combustion engines,[106] where the large surface area of the droplets provides rapid reaction during combustion. Ultrasonic atomization used in chapter 3 is another technique that generates droplets by applying strong ultrasonic waves onto a layer of liquid.[92] Beyond a certain threshold, the surface of the liquid becomes unstable and disperses small droplets into the air. In the medical field, ultrasonic atomization is implemented in nebulizers for delivering the precise amounts of drugs to the lungs.[107] Last, vibrating mesh atomization utilizes a mesh to reduce the required power for achieving atomization. Instead of subjecting the liquid itself to ultrasonic waves, this method places a mesh on the surface of the liquid. When this mesh vibrates, the liquid is separated into small droplets as it escapes the small holes of the mesh.[108] In general, this mesh is bonded at the center of a piezoelectric ring to generate such vibrations. Most applications for these atomizers take advantage of the large surface area of the droplets (*e.g.*, faster vaporization). In this chapter, the vibrating mesh atomizer was used for dispersing droplets into the chamber of a soft elastomer and for their low power consumption.

4.3. Rapid actuation through droplet evaporation

4.3.1. Fabrication

The setup of the system comprises an atomizer and a heater, which is illustrated in figure 27. The piezoelectric ring with the metal mesh was fixed in place above a piece of cotton. The purpose of the cotton is to absorb liquid so that the bottom of the mesh is always in contact with the liquid. When the ring vibrates, liquid stored in the moist cotton escapes through the mesh, and small droplets are dispersed into the chamber. Considering that the vapor pressure of ethanol is already in equilibrium in the sealed system, a separate heater is required to evaporate the droplets. To provide the driving force for evaporation, a heater was installed above the atomizer. The heater's cross-section and surface area was designed to maximize exposure of the ejected liquid droplets to heat. Both the heater and the atomizer were powered simultaneously during actuation. When actuation was tested with a single flat heater, the actuation speed was considerably slower. The heater consisted of interwoven nichrome wires that were sealed between two heat resistant silicone tapes.

The actuator setup was then sealed inside a soft elastomer to inflate the system upon vaporization. The molds for the bottom chamber and the bellows structure were 3D-printed with polylactic acid (PLA). Uncured Dragon Skin FX-Pro was poured into the mold to fabricate the stretchable structures. A tube was connected to the side of the structure to inject liquid into the system initially, as well as for exhausting the vapor after actuation. Since most elastomers have considerable permeability,[52] completely sealing the structure requires periodic injections of the liquid with a syringe. Connecting a tube provided a much easier method to fill the liquid for continued use. Here, 3 mL of ethanol was used as the phase-changing liquid due to its low boiling temperature and chemical inertness.

The image of the 3D-printed holder and the piezoelectric ring is shown in figure 28(a). The diameter of the disc was ~ 15 mm, and the inset shows the image of the mesh. The holes

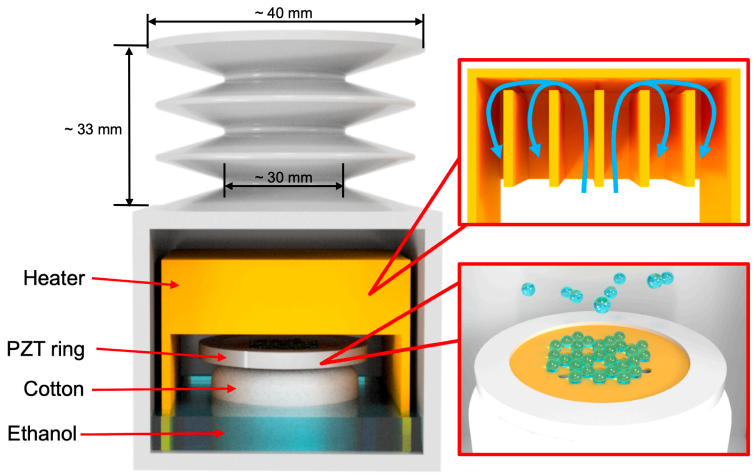

Figure 27. The schematic shows the setup of the actuator. The vibrating mesh was bonded to the center of the piezoelectric ring. The ring was fixed in place above a piece of cotton to supply liquid to the bottom of the mesh. Small droplets were dispersed into the air when the mesh was vibrated. These droplets evaporated as they passed through the heater. The cross-section of the heater was designed to maximize the surface area.

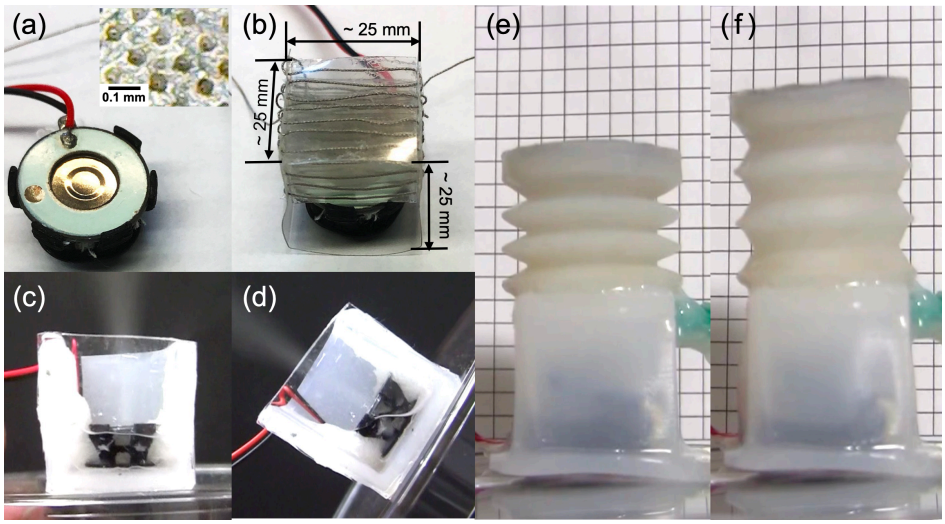

Figure 28. (a) A 3D-printed support fixed the cotton and the piezoelectric ring in place. The inset shows a magnified view of the mesh. (b) The heater was fabricated over the atomizer to evaporate the droplets. (c) One section of the wall was fabricated with a transparent material to visualize the atomization process. The cotton was spread out to cover the walls, which absorbed the liquid and supplied ethanol to the mesh atomizer. (d) Due to the cotton, the atomizer continued to function even when the system was tilted. (e) A bellows structure was bonded to the top of the chamber. The distance between the gridlines was 5 mm. (f) The displacement of the top layer reached ~ 13 mm after 8 s of actuation.

were in the shape of a cone with a bottom diameter (reservoir side) of ~ 60 μm and top diameter (dispersing side) of ~ 10 μm. The generated droplets were expected to be in the similar micrometer scale,[109-112] and these droplets were reported to evaporate almost immediately as compared to the actuation time.[113,114] The atomizer, which was capable of atomizing ~ 11 mg/s in an open system, was then installed inside of a hollow cuboid chamber. One side of the cuboid wall was fabricated with transparent polydimethylsiloxane (PDMS) to visualize the atomization process. The cotton under the mesh was wide enough to cover the walls of the inner chamber. The atomization circuit was powered with 5 V, and the piezoelectric ring was excited with a frequency of ~ 110 kHz. The power consumption of the atomizer was ~ 2 W. Figure 28(c) shows the atomizer dispersing ethanol into small droplets. The wide area of cotton was capable of absorbing ethanol even when the system was rotated. Consistent atomization is shown in figure 28(d), where the system was tilted to one side.

4.3.2. Actuation performance

The final structure was placed in front of a grid with gridlines separated by 5 mm, as shown in figure 28(e). The atomizer and the heater were powered simultaneously, where the atomizer was powered with ~ 2 W, and 8 V was applied to the heater. The power that was consumed by the heater was ~ 15 W (*i.e.*, current was ~ 1.8 A). The structure started to inflate immediately, and the displacement of the top layer reached ~ 13 mm (strain of ~ 40 %) after 8 s. The inflated structure after actuation is shown in figure 28(f). Video was recorded throughout the actuation process, and the displacement was periodically measured using image processing. The displacement time history is plotted in figure 29(a). Three different voltage conditions (4, 6, and 8 V) were applied to the heater to characterize actuation performance, and these tests were repeated five times to obtain statistically representative results. For all three conditions, figure 29(a) shows that the instantaneous displacement (*i.e.*, slope at any given time) stared to

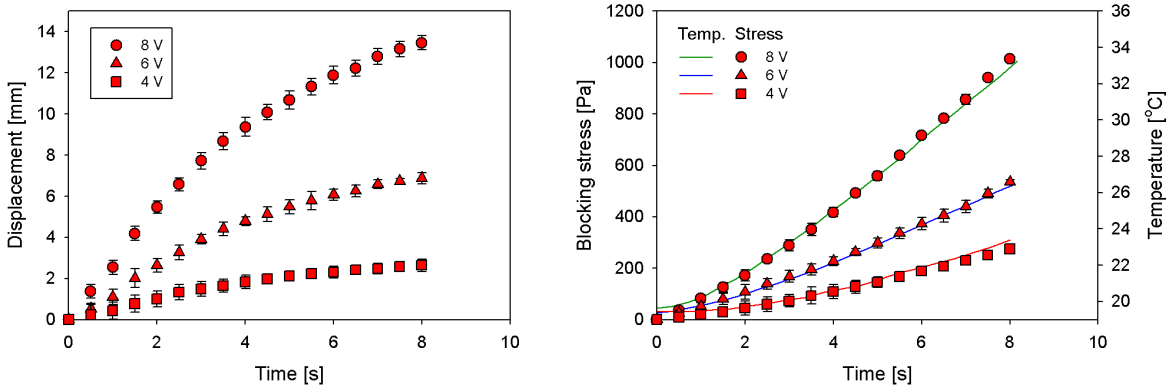

(a) (b)

Figure 29. (a) The displacement of the top layer was measured for 8 s when the heater was powered by 4, 6, and 8 V. (b) A load cell was placed above the structure to measure blocking stress. The temperature of the heater was also measured using an embedded thermocouple. Each condition was tested five times to show the averages and corresponding error bars.

decrease with continued actuation, since more force was required to deform the hyperelastic bellows structure. Blocking stress was also measured by fixing a load cell above the bellows structure, thus fixing the displacement at its initial position throughout actuation. The dotted plots in figure 29(b) show the blocking stress for the same voltage conditions, which were also tested five times to calculate the average. The blocking stress reached ~ 1,000 Pa after applying 8 V to the heater for 8 s. Unlike the displacement time histories, the instantaneous slopes in figure 29(b) continued to increase, as blocking stress was not affected by the deformed structure. Thus, blocking stress was a better comparison with the temperature increase of the heater. To make such a comparison, temperature change was measured by installing a thermocouple inside the heater. The increasing trend of temperature agreed with the increase in blocking stress. It is worth pointing out that the maximum temperature throughout the test was only ~ 34 °C, which is well below the boiling temperature of ethanol (78 °C). However, applying 8 V to the heater without atomization increased the temperature to ~ 100 °C after 8 s. When the heater was turned on together with the atomizer, the temperature rise was much lower, since the droplets absorbed most of the heat during vaporization.

In order to demonstrate the effects of atomization, a similar test was conducted by submerging the heater under the same amount of ethanol (3 mL). Even after operating the heater with 8 V for 8 s, no change in displacement was observed. Compared to other studies that heat the system beyond the boiling point, implementing atomization provides significant benefits by drastically enhancing actuation speed with significantly less input power. Two parameters can be adjusted to further increase blocking stress. Since stress is directly affected by temperature, simply powering the heater for a longer time or applying higher current will result in higher blocking stress. As mentioned earlier, it was observed that the surface area of the heater highly affects vaporization rate as well. Designing a heater that increases the surface area is also expected to increase blocking stress.

When comparing this work with other methods, the displacement plot in figure 29(a) is not a suitable reference. Thus, the displacement was converted to the amount of gas that was generated during actuation, which was also shown in chapter 3. A finite element model (FEM) was used to correlate displacements with volume. The bellows structure was modeled as a hyperelastic structure, and the Neo-Hookean parameter was obtained from tensile testing. Then the structure was inflated through the ideal gas model using equation (9). The bellows structure was predominantly discretized with tetrahedron elements, while the bottom layer was fixed in place. The number of elements were ~ 17,000, and the displacement of the top layer was analyzed while increasing gas volume inside the bellows structure. The simulation was used to convert displacement to the corresponding change in volume.

The results of the change in volume are plotted in figure 30. To provide a better comparison, the total consumed power is indicated instead of voltage. The applied power of 6, 11, and 17 W corresponds to inputs of 4, 6, and 8 V, respectively. For all three conditions, 2 W was consumed by the atomizer, while the rest was applied to the heater. When 8 V was applied to the heater, vapor was generated at a rate of ~ 2 cm^3/s. It is worth mentioning again that heating the bulk liquid with the same heater showed no change in volume. The results from actuation through ultrasonic atomization in chapter 3 are also plotted for comparison. Not only did ultrasonic atomization required higher power (~ 23 W), but its vaporization rate was also significantly lower. In addition, the results were compared with a commercial pneumatic pump. The same structure was connected to a pump with a power consumption of 5 W. The structure was inflated using the pump for 8 s, and displacement was converted into change in volume using results from the FEM. This test was also repeated five times to obtain the average. The analysis showed that the amount of injected gas inside the structure was similar to applying 17 W of power to vaporize ethanol through mesh atomization. Although the technique introduced in this study consumes more power, the result shows promising potential for liquid vaporization

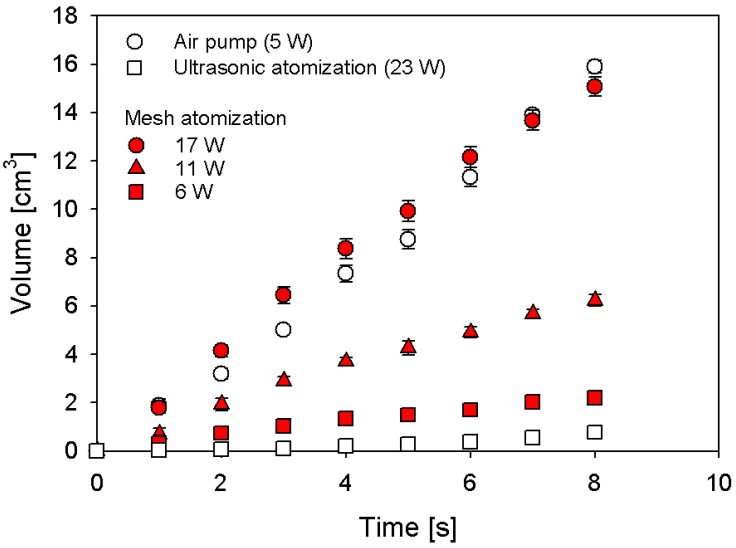

Figure 30. The displacement results were converted to the amount of generated gas. The power consumption of the atomizer and the heater was included in the total electrical work. The results are compared with ultrasonic atomization and a commercial pneumatic pump.

to demonstrate comparable performance as when pneumatic pumps are used. Overall, the developed method drastically improved actuation performance (as compared to simple boiling) by adding a vibrating mesh (~ 0.9 g) and a circuit (~ 7.2 g) to control atomization. These additional components are much smaller and lighter versus traditional pneumatic pumps (~ 100 g), which make them suitable for use in untethered and portable soft robotic systems.

4.3.3. Cyclic actuation

The repeatability of actuation through mesh atomization was studied by inflating the structure and exhausting the vapor through a valve. While any type of valve can be implemented, Arduino was used to control a small solenoid valve in this study. One of the benefits of vaporizing liquid through mesh atomization is that it enhances the vaporization rate regardless of how much liquid is stored in the system. This sufficient reservoir of ethanol allows the implementation of valves for the reversing process. The total number of actuation cycles for a fixed amount of embedded fluid can be estimated by assuming the ideal gas condition. The ethanol molar mass of 46.07 g/mol, density of 789 kg/m^3, and molar volume of 22.4 L were used to calculate the number of possible actuations when the change in volume during actuation was ~ 9.4 cm^3. It was estimated that 3 mL of ethanol was capable of actuating the structure ~ 120 times.

The actual experiment was conducted by applying 7 V to the heater during ~ 10 s of actuation, followed by exhausting the vapor through the solenoid valve. The next actuation was performed after 15 s for allowing time for the system to cool. The repeatability of actuation is plotted in figure 31. The minimum and maximum temperature during cyclic actuation testing is also overlaid as an area plot. The inset shows a zoomed-in portion of the time history response to better visualize its displacement and temperature response. The maximum displacement slowly increased, since temperature did not reach the initial value after each cycle. Although

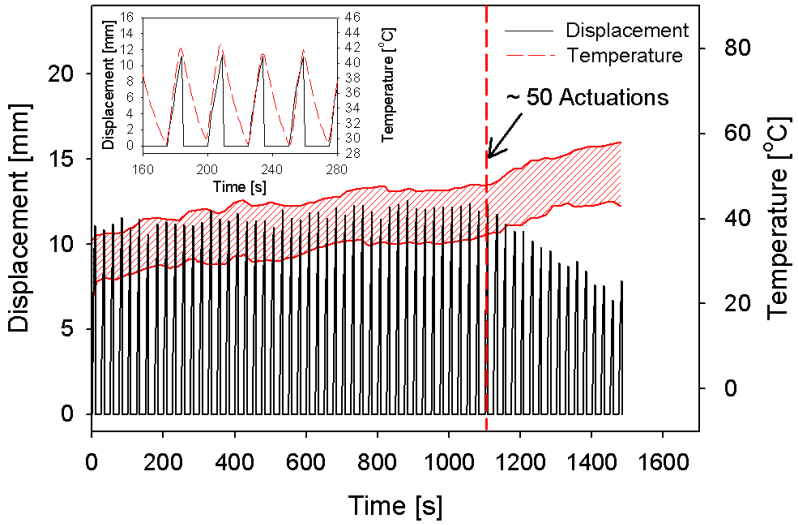

Figure 31. The structure filled with 3 mL of ethanol was repeatedly actuated for 10 s and then deflated. The next actuation was performed after 15 s to allow time for cooling in between actuations. The line plot show the displacement results, while the measured temperature range is shown by the area plot. The inset shows an enlarged view of system response during actuation and cooling. The displacement started to decrease after ~ 50 actuation cycles.

3 mL of ethanol was estimated to actuate the structure for ~ 120 times, the maximum displacement started to decrease after ~ 50 times. The most critical reason for this large discrepancy was because the chamber was completely filled with droplets during actuation. When opening the valve, a small portion of these droplets also escaped in addition to evaporated ethanol gas. Furthermore, the fact that the chamber was filled with the droplets also indicated that the atomizer was generating more droplets than the heater could evaporate. Thus, reducing the atomization rate is expected to minimize the escaping droplets and increase the number of consistent actuation cycles. The decreasing maximum displacement after ~ 50 cycles also indicates that a certain amount of ethanol is required for the liquid to be fully in contact with the vibrating mesh and for it to atomize properly. Atomization rate rapidly decreases when the remaining ethanol was less than this required amount. This can also be observed from the temperature increase after ~ 50 cycles of actuation due to less heat absorbed during phase transformation. Nevertheless, the current test setup was capable of actuating the structure for ~ 50 times using only 3 mL of ethanol.

4.4. Effect of atomization rate

4.4.1. Experimental setup

The mesh atomizer consisted of a piezoelectric ring and a metal mesh at the center. Similar to most vibrating mesh atomizers, the mesh consisted of conical holes that had a diameter of ~ 80 μm at the bottom and ~ 10 μm at the top. The setup to measure the atomization rate is shown in figure 32(a). The alternating current (AC) voltage that controls the mesh atomizer was produced by a Keysight 33210A function generator, which was amplified with an Electronics & Innovation 500S06 amplifier to power the piezoelectric ring. The atomizer was placed on the surface of the water inside a plastic petri dish. This petri dish was placed above a Mettler Toledo ME204E scale to measure weight loss. The weight loss was plotted over time, and the linear slope was measured to quantify the atomization rate.

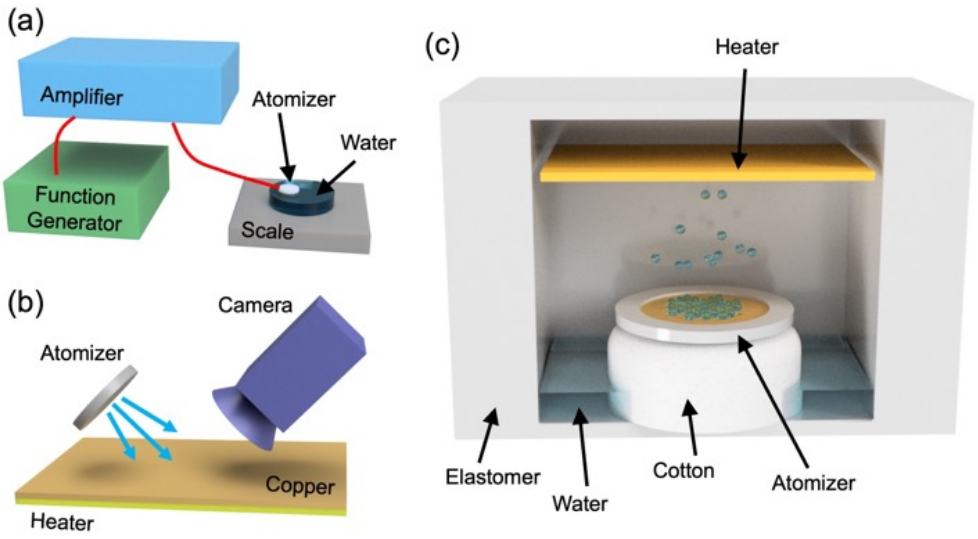

Figure 32. (a) The schematic shows the setup for measuring the atomization rate. A function generator was connected to an amplifier, which powered the atomizer. (b) The size of the droplets on the heater surface was measured with an optical microscope. The droplets were sprayed at an angle for the camera to record. (c) The image shows the cross-section of the actuator. The atomizer was fixed in place above the cotton wick, which absorbed the embedded water. The droplets were ejected to the heater, and the vapor inflated the structure.

In order to study the evaporation process, the sizes of the droplets were measured at the heater surface, and the setup is shown in figure 32(b). The heater consisted of nichrome wires that generated heat when current was applied. In this work, 3 V was applied to the heater using an Agilent E3642A, which was equivalent to ~ 0.34 A of current. A strip of 3M copper tape of high thermal conductivity was applied to the surface of the heater to better visualize the droplets. The atomizer was positioned so that it sprayed droplets to the heater at an angle. The droplets were collected at the heater surface, and their size was measured with an optical microscope. The sizes of the droplets were measured by calculating the average of the longest diameter of ~ 50 droplets. The temperature change at the surface was also measured with an Omega thermocouple throughout the test.

Actuation performance was measured by sealing the atomizer and heater inside a soft silicone elastomer, which was similar to previous experiments. The setup is shown in figure 32(c), where the atomizer was fixed in place above a cotton wick. After sealing the structure, 1 mL of water was injected into the chamber. The wick absorbed the embedded water so that the mesh can atomize the liquid. A flat compact heater was installed above the atomizer to evaporate the droplets. Although heater designs with complex cross-sections are expected to improve the evaporation process, a simple flat heater was used in this study to simplify the conditions. These components were sealed with Dragon Skin FX-Pro to achieve inflation during vaporization. The uncured elastomer was poured into 3D-printed molds to form the shapes. The side walls were ~ 6 mm thick, whereas the top layer was ~ 0.5 mm thick. The difference in thickness concentrated the deformation to the top layer, which was measured during testing. A video was recorded throughout the test, and image processing was used to calculate the displacement.

4.4.2. FE model

The detailed dimension of the atomizer is shown in figure 33(a). The piezoelectric ring

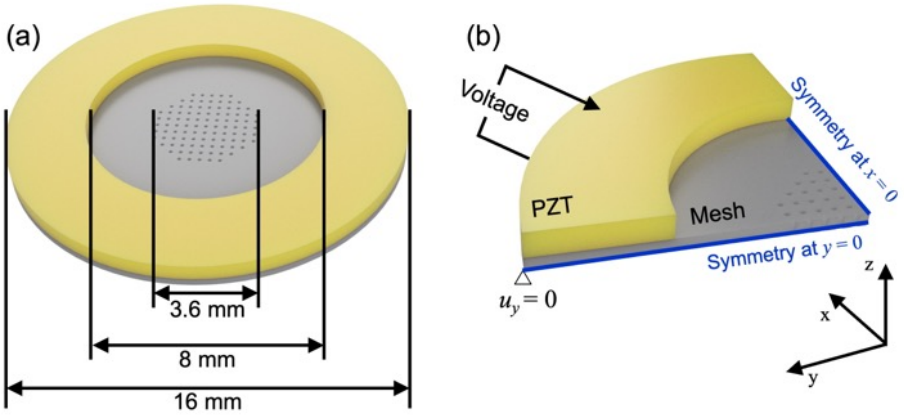

Figure 33. (a) The schematic shows the dimension of the atomizer. (b) The image shows how the atomizer was modeled in *ANSYS*. The voltage was applied to the top and bottom layers of the piezoelectric ring.

had an outer diameter of 16 mm and an inner diameter of 8 mm. The thickness of the ring was 0.63 mm, and the thickness of the metal mesh was 50 μm. The holes of the mesh were within 1.8 mm from the center of the disc. The mesh had 551 number of conical holes with ~ 80 μm on the bottom and ~ 10 μm on the top. Figure 33(b) shows the FEM in *ANSYS*. A quarter of the atomizer was modeled with *x* and *y*-axis symmetry. The displacement of the bottom edge was fixed in the *y*-direction, and voltage was applied to the top and bottom layers of the piezoelectric ring. The quarter of the piezoelectric ring was mapped using 675 number of SOLID5 hexahedral elements of eight nodes per element, and the stainless-steel disc consisted of 70341 number of SOLID186 tetrahedral elements of eight nodes per element with quadratic displacement.

The linear constitutive relations that define the coupling between mechanical stress, mechanical strain, electric field, and electric displacement are given as[115]:

$$\boldsymbol{\sigma} = [C^E] \cdot \boldsymbol{\varepsilon} - [e] \cdot \boldsymbol{E} \tag{11}$$

$$\boldsymbol{D} = [e]^T \cdot \boldsymbol{\varepsilon} + [\xi^S] \cdot \boldsymbol{E} \tag{12}$$

where $\boldsymbol{\sigma}$ is stress tensor, $\boldsymbol{D}$ is electric displacement vector, $\boldsymbol{\varepsilon}$ is strain tensor, $\boldsymbol{E}$ is electric field, $[C^E]$ is elastic constant at constant electric field, $[e]$ is piezoelectric stress coefficients, T is transpose of e, and $[\xi^S]$ is dielectric tensor at constant mechanic strain. The mechanical and electrical balance of the system can be defined using the following equations:

$$\rho \ddot{\boldsymbol{u}} = \nabla \cdot \sigma \tag{13}$$

$$\nabla \cdot \boldsymbol{D} = 0 \tag{14}$$

A frequency sweep of voltage was applied to the piezoelectric ring to analyze the vibration modes. The displacement at the center of the metal mesh was recorded to visualize the

results. Vibration modes of frequencies showing displacement peaks were also obtained. The parameters for the piezoelectric ring and stainless steel were obtained from parameters reported in other literatures.[116,117] A density of 7980 kg/m^3, Young's modulus of 186.8 GPa, and Poisson's ratio of 0.31 were used for the stainless steel. A density of 7500 kg/m^3 and Poisson's ratio of 0.32 were used for the piezoelectric ring. Detailed information on dielectric constant, piezoelectric constant, and elastic constant can be found in a previous literature.[116]

4.4.3. Vibration modes

Figure 34 shows the FEM result of a wide frequency sweep when 20 V of AC voltage was applied to the PZT ring. The displacement at the center of the disc was measured to represent the modes. The result shows several resonant frequencies from 0 to 150 kHz, where 110 kHz and 141 kHz showed the highest peaks. The max displacement at 110 kHz reached ~ 6 μm, while 141 kHz reached ~ 4.2 μm. The vibration modes of the two peaks are also shown in figure 34. At 110 kHz, the displacement was focused near the center of the disc. On the other hand, displacement at 141 kHz was relatively distributed evenly throughout the mesh. In addition, the piezoelectric ring also showed a small amount of displacement. The shapes of the cross-section are also expected to affect the atomization rate, since holes are concentrated near the center of the disc. Higher displacement at the center will facilitate higher atomization rate.[108] The next two highest peaks were at much lower frequencies between 20 and 30 kHz. However, the actual experiment did not show any atomization at these frequencies. Therefore, the experiments performed hereafter were focused on the frequency range between 100 and 150 kHz.

4.4.4. Displacement and atomization rate

The atomization rate was quantified by measuring weight loss during atomization, and

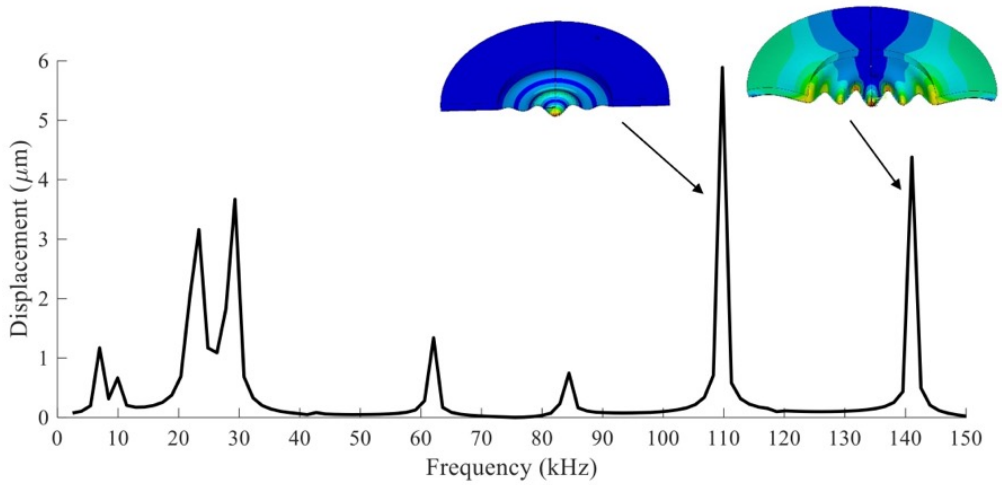

Figure 34. The displacement at the center of the mesh was measured through FEM during a frequency sweep. The vibration modes of the two largest peaks are also shown.

the results are shown in figure 35(a). The atomization rate was measured at 2 kHz intervals from 100 kHz to 150 kHz. The voltage applied to the atomizer was 80 V. Any frequencies without data points did not show any visible atomization. For comparison, an FEM result similar to figure 34 is also shown when 80 V was applied to the piezoelectric ring. The highest displacements at 110 kHz and 140 kHz were ~ 23 μm and ~ 13 μm, respectively. Similar to the FEM result, the atomization rate demonstrated two peaks at 110 kHz and 141 kHz. The atomization rate at 110 kHz was ~ 400 mg/min, whereas at 141 kHz, it was ~ 250 mg/min. Although the frequencies of the maximum peaks were in good agreement with the FEM results, the shape of the spectra distribution showed some discrepancies. These small differences were expected as the actual atomizer used epoxy to bond the piezoelectric ring to the metal mesh. In addition, the wires that were soldered to the ring also affected its vibration behavior.

The effect of voltage was studied at a frequency of 110 kHz, since it showed the largest amount of displacement and atomization rate. The displacement at voltages of 5, 10, 20, 40, 60, and 80 V were obtained through FEM. The trend was fairly linear, and the displacement at 80 V was the same as the result in figure 35(b). The atomization rate also decreased in a linear trend with decreasing voltage. However, the linear fit of the experimental result showed that a minimum of ~ 18 V was required for atomization. The results from figure 35 show that the FEM can be used to determine the optimal frequency of the atomizer, while increasing the driving voltage will linearly increase atomization rate.

4.4.5. Droplet analysis

The droplet size on the heater surface was studied in this section to analyze the effect of atomization rate on evaporation. The voltage applied to the atomizer varied from 40 to 80 V, and it was powered simultaneously with the heater. Figure 36 shows images of the droplets when atomizing water using 80 V. At this highest voltage, the growth of droplets was higher than the

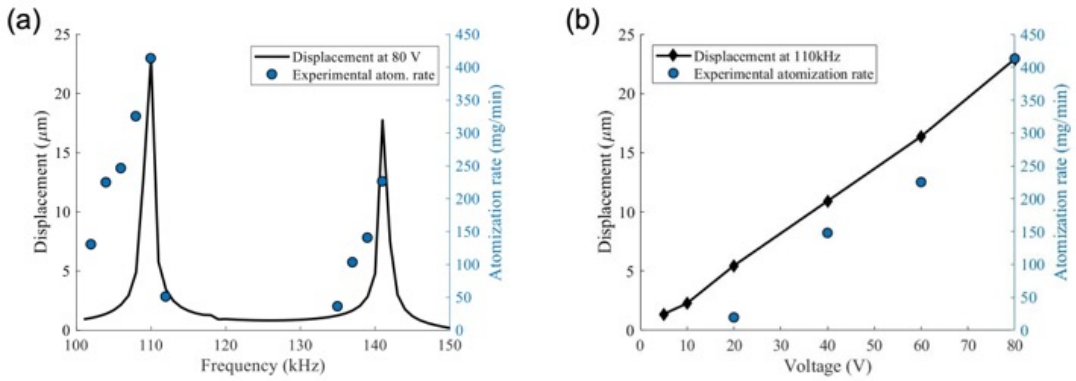

Figure 35. (a) The displacement of the center of the disc obtained from FEM is plotted together with the experimentally measured atomization rate. A voltage of 80 V was used for both results. (b) The plot shows displacement at the center of the disc at different frequencies. The results are compared with the atomization rate.

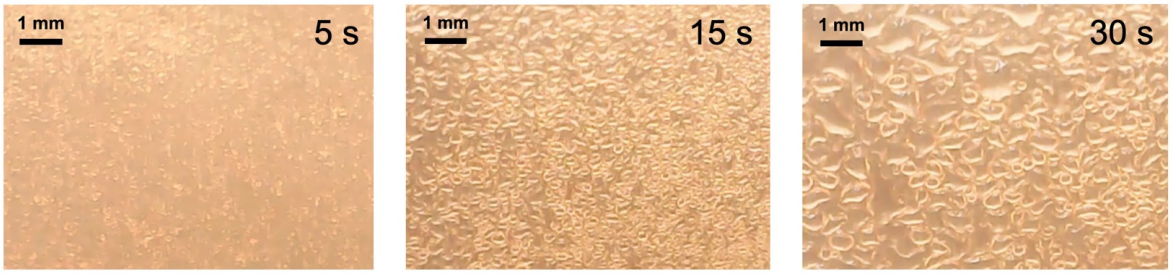

Figure 36. The images show the droplets at the heater surface when the atomizer was powered with 80 V. Power of ~ 1 W was applied to the heater. The droplets quickly started to grow over time.

evaporation rate. As a result, the size of the droplets continued to grow over time. The size started at ~ 70 μm at 5 s and quickly grew to ~ 400 μm after 30 s. Table 1 shows the average and standard deviation of the droplet sizes measured throughout the test. The results are better visualized in figure 37(a). At 40 V, the size of the droplets initially started to grow but decreased after ~ 10 s. The droplet size at this lowest voltage remained less than 100 μm throughout the test. At 44 V, the size tended to plateau after ~ 20 s, and the size increased continuously at 48 V or higher.

The temperature of the heater was also measured during the tests, and the results are shown in figure 37(b). The test conducted with 40 V showed the largest temperature increase over time and eventually reached ~ 2.7 °C. Considering that the boiling temperature of water is 100 °C, this very small increase in temperature was enough to evaporate the small droplets. The lowest atomization rate showed the slowest growth rate of the droplets, and the size started to decrease as temperature continued to rise. Experiments at higher atomization rates showed different trends when the droplet growth rate was larger than the evaporation rate. The surface area of the droplets starts to decrease with increasing droplet size, which significantly slows down the evaporation rate at the liquid surface. As a result of heating large droplets, the highest atomization rate at 80 V showed the lowest temperature increase after 30 s. These results show that evaporation rate converges to a maximum at a certain atomization rate. When higher voltage is applied to the heater, the optimal voltage to power the atomizer is expected to increase. Although this test was conducted in an open system, the buildup of droplets on the surface of the heater is expected to be present even in a closed system.

4.4.6. Effect on actuation

Figure 38(a) shows the fabricated structure placed in front of a grid with grid spacings

Table 1. Droplet size on the heater surface was measured over time during atomization.

Time / Voltage	5 s		10 s		15 s		20 s		25 s		30 s	
	Aver. (μm)	Std. (μm)	Aver.	Std.	Aver.	Std.	Aver.	Std.	Aver.	Std.	Aver.	Std.
40 V	77.1	14.4	95.7	21.8	94.8	26.0	93.9	23.0	74.5	20.3	67.7	13.4
44 V	67.7	13.4	94.8	18.2	114.7	29.8	123.3	36.7	102.0	15.1	113.0	19.7
48 V	66.5	15.0	89.0	21.3	105.2	18.2	112.7	26.6	124.9	19.5	126.1	41.4
52 V	76.0	14.0	102.8	15.9	114.4	32.0	139.0	44.4	150.3	41.1	164.7	43.2
56 V	86.2	20.5	124.9	32.6	127.1	44.9	159.4	54.9	190.3	91.1	220.8	50.3
60 V	71.1	13.0	111.6	38.3	142.9	51.3	205.9	91.8	248.9	84.6	322.3	111.3
80 V	73.8	15.6	147.9	58.1	263.8	100.7	311.7	119.5	364.1	104.4	402.4	117.9

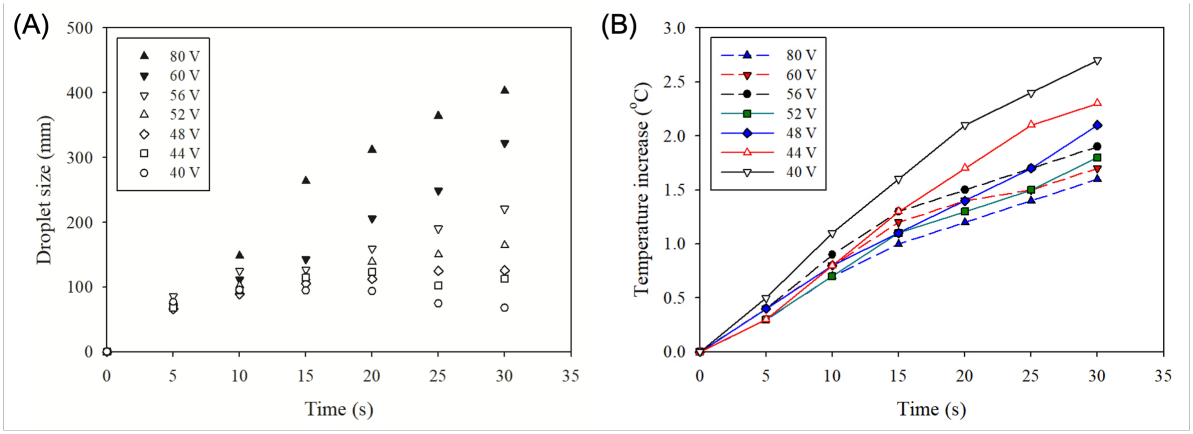

Figure 37. (a) The sizes of the droplets were measured over time. The voltage that powered the atomizer varied from 40 to 80 V. (b) The temperature of the heater was also measured throughout the test.

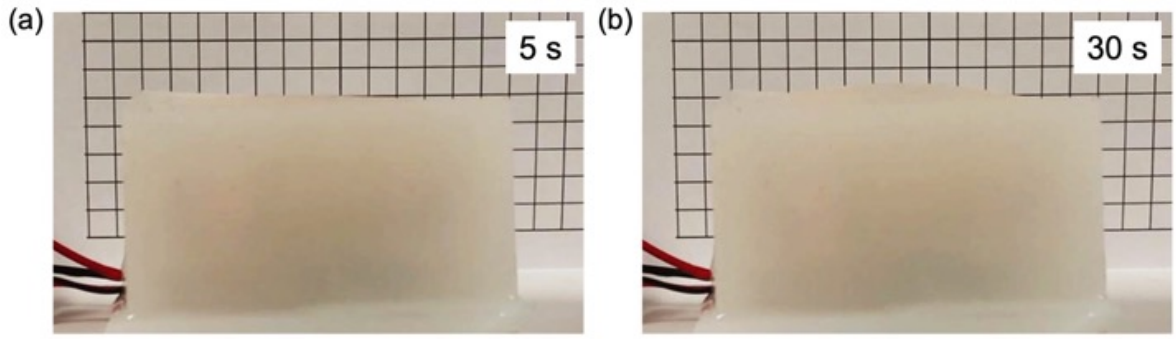

Figure 38. (a) The fabricated structure is placed in front of a grid with lines separated by 5 mm. (b) The image shows the inflated structure after 30 s of actuation.

of 5 mm. Voltages from 40 V to 100 V were applied to the atomizer at 10 V intervals, and 3 V applied to the heater resulted in 0.6 A of current. The structure after 30 s of actuation is shown in figure 38(b). Similar to the droplet size test in section 4.4.5., the heater and atomizer were powered simultaneously. The deformation of the cuboid structure was concentrated on the top layer due to its thinness. Inflation was recorded with a video camera, and image processing was used to determine the maximum displacement at the center. Since the method used water instead of ethanol, which was used in previous chapters, the rate of inflation was visibly slower. Nevertheless, the measured displacements provide information on how atomization rate affects actuation.

In order to represent the actuation performance, the displacement of the top layer after 30 s of actuation is plotted in figure 39. It was expected that the compact heater with higher power consumption used in the actuator reached higher temperatures in the closed system. The displacement increased linearly up to 80 V, which showed a maximum displacement of ~ 2.4 mm. The displacement started to decrease beyond this point, which reached ~ 1.8 mm at 100 V. The illustration above the plot represents the condition explained in the previous section. At lower atomization rates, the growth of droplets on the heater surface was lower than the evaporation rate. However, these droplets are expected to grow larger after a certain threshold. Continued increase in atomization rate will form larger droplets at the heater surface, which decreases the evaporation rate due to lower surface area. Eventually, evaporation is expected to significantly decrease when a thin liquid layer is formed on the heater surface, preventing the atomized droplets to come in contact with the heater. In the system presented in this work, ~ 80 V appeared to be the optimal voltage that maximized the evaporation process.

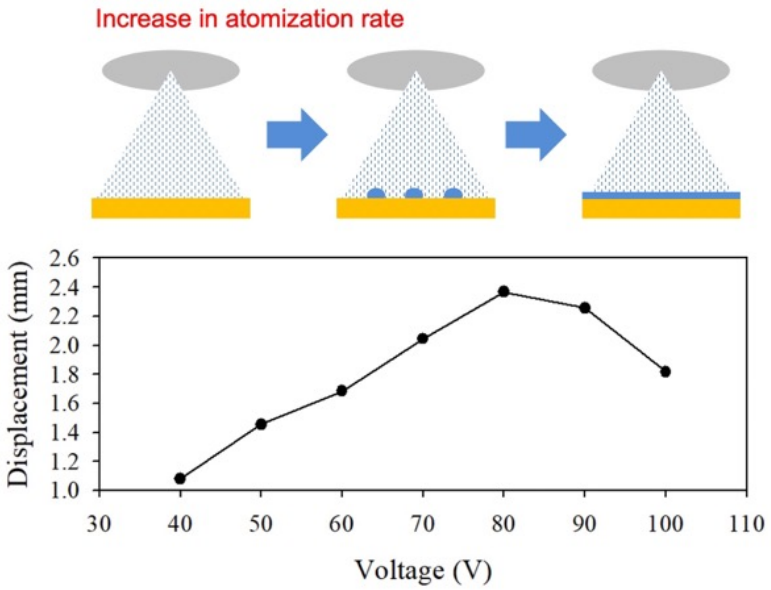

Figure 39. The displacement of the top layer after 30 s of actuation is shown in the plot. Higher voltage applied to the atomizer resulted in higher atomization rate. The large growth of the droplets at the heater surface slowed down the actuation speed.

4.5. Portable bistable gripper demonstration

Compliant mechanisms are widely used to convert the direction of movement,[118] amplify or reduce the degree of stress and strain,[119] and perform rapid movements through buckling.[120] Since cooling takes much longer than actuation for methods involving phase change, a bistable structure with a built-in snap-through buckling mechanism was utilized to achieve consistent movement speed. In addition, the bistable buckling mechanism can be used to maintain displacement without the need to consistently power the actuator. The schematic of the bistable gripper is shown in figure 40(a). The bistable finger was 3D-printed with thermoplastic polyurethane (TPU), and the stiff outer structure was 3D-printed with PLA. Two inflating structures were fixed in place to activate the buckling of the finger. Valves were not implemented for this demonstration, since buckling provides fast and consistent speed during the back-and-forth movements.

The amount of load that is required to activate buckling and bistable response was analyzed for characterizing the actuation process. Figure 40(b) shows a simplified drawing of the buckling structure, where the length between points A and B (d_{AB}) is the same as the length between points A and C (d_{AC}). The required force at point A is expected to vary throughout the deformation process. The force that spreads points B and C (F_{BC}) can be expressed as follows:

$$F_{BC} = \frac{F \sin\theta}{2\cos\theta} \tag{15}$$

where F is the vertical force applied at point A, and θ is half of the angle $\angle$BAC. Since the required F_{BC} increases as the distance between B and C (d_{BC}) increases, F_{BC} can be expressed as a function of Δd_{BC}. When the change in d_{BC} is small, the relationship can be assumed to be linear.

$$F_{BC} = E \times \Delta d_{BC} \tag{16}$$

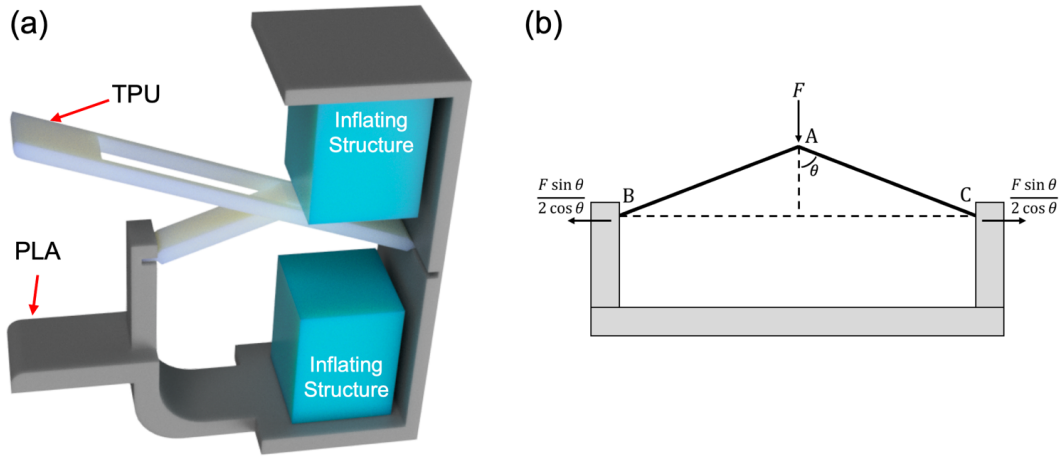

Figure 40. (a) A bistable gripper was fabricated by 3D-printing. Two inflating structures were installed to achieve cyclic motion. (b) The illustration shows the cross-section of the bistable structure.

where E is a proportionality constant or an equivalent stiffness of the system. This relationship was measured by spreading points B and C with a universal tensile machine (UTM), and the measured value for E was 2.91 N/mm. Here, Δd_{BC} can be expressed as follows from figure 40(b).

$$\Delta d_{BC} = 2d_{AB}(\sin\theta - \sin\theta_0) \tag{17}$$

where θ_0 is the initial angle. Combining equations (2), (3), and (4) results in the following equation.

$$F = 4E d_{AB} \frac{\cos\theta}{\sin\theta}(\sin\theta - \sin\theta_0) \tag{18}$$

The initial angle (θ_0) was 74°, and d_{AB} was 26 mm for the fabricated gripper. The predicted F was compared with experimental results to analyze the actuation process.

The image of the fabricated gripper is shown in figure 41. The portable system consisted of two lithium polymer (LiPo) batteries, a 9 V battery, a circuit for the atomizer, and a double-pole double-throw (DPDT) toggle switch. The two LiPo batteries were connected in series, and the output voltage was ~ 8 V when fully charged. These LiPo batteries were used to power the heater, and the 9 V battery was used to power the atomizer. Actuating the two inflating structures in sequence demonstrated the cyclic motion of the bistable structure. Similar to the displacement measurements conducted earlier, video was recorded, and image processing was used to determine the distance between the two fingertips.

Before actuating the structure, the UTM was used to buckle the finger by vertically pressing down at point A. The dotted plot in figure 42(a) shows the experimental results, and the plot is compared with the analytical prediction. The two results were in fairly good agreement. The required load increased and reached a maximum value of ~1.2 N when displacement was ~3 mm. After reaching the

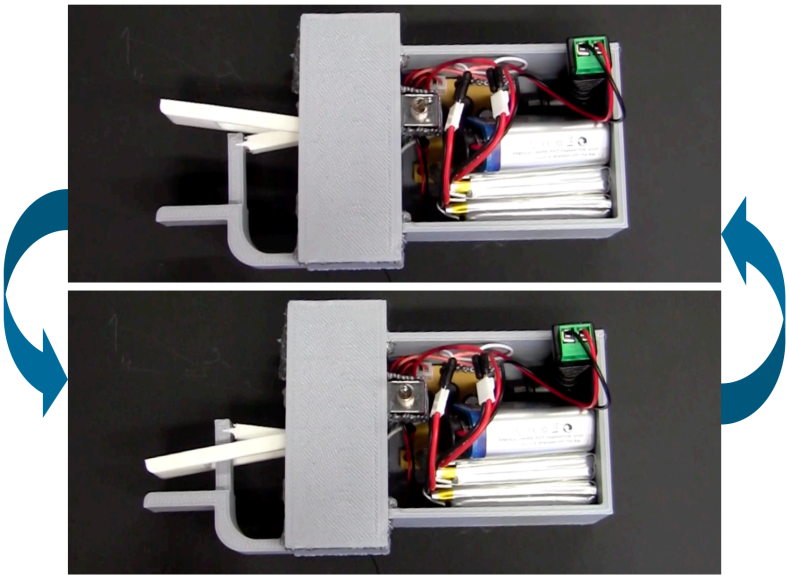

Figure 41. The entire system of the bistable gripper included two lithium polymer batteries, a 9 V battery, a circuit board, and a double-pole double-throw toggle switch. Flipping the switch actuated the two inflating structures and moved the finger.

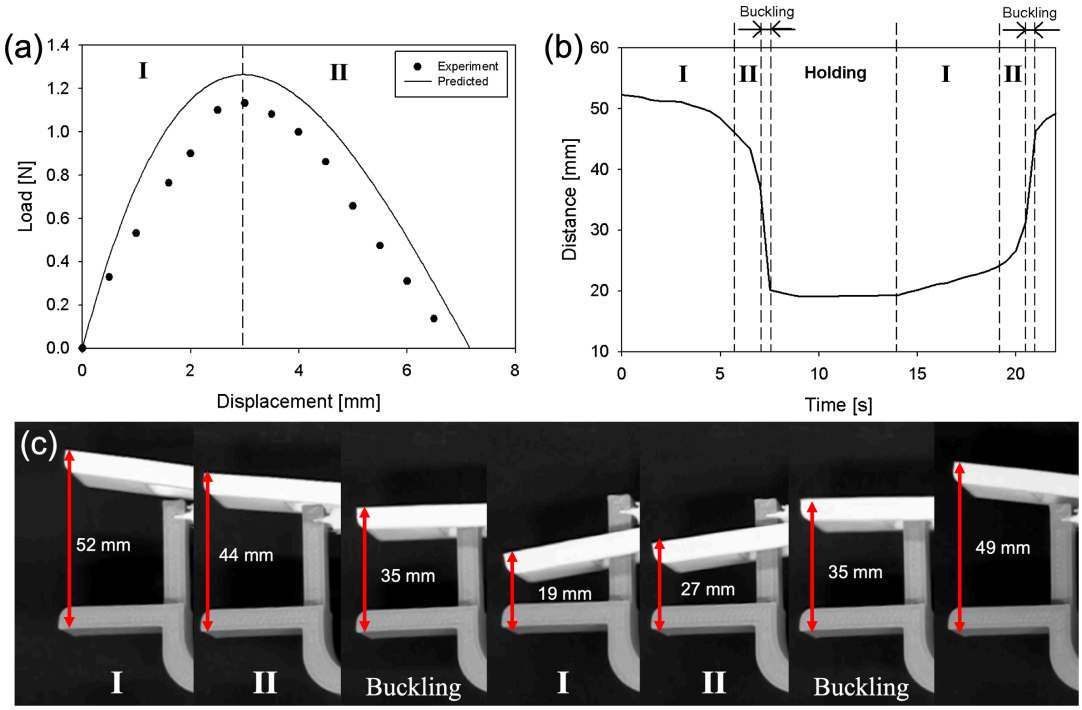

Figure 42. (a) A universal tensile machine was used to measure the load required to activate the bi-stable structure. (b) The distance between the two fingertips is plotted with respect to time. (c) Corresponding images of the fingertips are shown for each stage of loading.

maximum point, load started to decrease until the finger buckled after ~7 mm of vertical displacement. The first region with increasing load was labeled as I, and the second region with decreasing load was labeled as II. It can be predicted that the finger will move much faster once it reaches region II since the required load decreases.

The distance between the two fingertips during actuation is plotted in figure 42(b). When the upper actuator was turned on (at 0 s), the fingertip started to move slowly (region I). Its speed continued to increase, and the fingertip moved much faster as it reached region II. It was clearly observed that region I took much longer than region II, and this can be explained by the reducing load requirement in region II. Once the fingertip reached the critical buckling point, the finger snapped through and moved to the other end. By implementing the proposed actuator, the finger was actuated within 10 s of actuation, while boiling is expected to take several minutes. After the first actuation at ~8 s, the system was turned off for a short amount of time. Actuating the lower inflatable structure at ~14 s showed a similar result and returned the fingertip to its original position. Figure 42(c) shows the images of the fingertips for each region. It is worth pointing out that the final distance was slightly smaller than the initial distance. This is because the first upper inflatable structure did not fully cool down after the second actuation sequence. Nonetheless, the two actuation speeds were quite consistent, which shows the potential of implementing bistable structures to overcome the dissimilar speeds between heating and cooling the system when actuated by vaporization.

4.6. Conclusions

This chapter introduces the very first implementation of vibrating mesh atomization in soft actuation systems. This novel method of rapidly vaporizing liquid inside a soft elastomer is promising for replacing pneumatic pumps. The small actuator consisted of a metal mesh, piezoelectric ring, piece of cotton, and heater. The purpose of the cotton was to absorb the embedded liquid and allow the mesh to be in contact with the liquid regardless of the actuator's physical orientation. When the piezoelectric ring vibrated the metal mesh, liquid was dispersed into small droplets. The heater was designed to

maximize surface area, which directly affected vaporization rate. Overall, the proposed method provides several advantages with respect to conventional actuation methods (*i.e.*, boiling bulk liquid for actuation) in several aspects. First, dispersing the liquid into droplets opens the possibility of implementing evaporation instead of boiling. The results showed that considerable actuation was achieved even at temperatures well below boiling. Second, the vaporization rate of the proposed method was much higher compared with using the same heater for boiling the same amount of liquid. Third, actuation through vibrating mesh atomization could maintain a high vaporization rate even when a large amount of liquid is stored in the system. This allowed utilizing valves to simply exhaust the vapor rather than slowly cooling the system when trying to reverse the actuator's motions. Fourth, actuation was still functional even when the system was tilted. This was also an improvement compared with boiling bulk liquid with a heating element since the liquid would no longer be required to be in contact with the heater in this case. In addition, although the required power of the introduced method was ~ 3 times higher than a commercial pneumatic pump, the gas generation rate was almost similar. This is a great improvement because a small piezoelectric ring and a heater can potentially replace heavy and bulky pumps. In addition, the effect of atomization rate on droplet growth at the heater surface was studied to maximize the performance of the system. First, FEM was used to analyze the vibration modes of the atomizer. The simulation successfully predicted the resonant frequency of the system, which was chosen as the driving frequency for the piezoelectric ring. Increasing the voltage in the FEM showed a linear increase in displacement at the center of the disc. Although the experimental atomization rate showed a threshold, it also demonstrated a linear increase with increasing voltage. Second, the droplet growth was measured on the heater surface during atomization. At lower voltages, the size of the droplets eventually started to decrease over time. This is due to the constant heat generated by the heater, which steadily increased temperature. When the atomizer was powered with higher voltages, however, the droplets steadily started to grow on the heater surface over time. These results show that simply maximizing the atomization rate will impede the evaporation process. This effect was demonstrated by measuring the displacement of a soft actuator. The displacement of the system increased with increasing

atomization rate until it reached a maximum value. Powering the atomizer with voltages beyond this point resulted in lower actuation rates. Therefore, the optimal atomization rate should be first determined for a given heating condition to maximize the performance of the actuator.

4.7. Acknowledgments

Chapter 4, in part, is a reprint of the materials as it appears in Rapid soft material actuation through droplet evaporation, Soft Robotics (In press) DOI: 10.1089/soro.2020.0055 H.-J. Lee, P. Prachaseree, and K.J. Loh, and in part, has been submitted for publication of the material as it may appear in Frontiers in Robotics and AI (2021), H.-J. Lee, E. Guerra-Bravo, A. Baltazar, and K.J. Loh. The dissertation author was the primary investigator and author of both papers. These works were supported by the University of California Institute for Mexico and the United States (UC MEXUS) under Grant No. CN-19-153 and the U.S. National Science Foundation under Grant Nos. CMMI-1762530 and CMMI-2032021. Additional support was provided by the Jacobs School of Engineering, University of California San Diego.

Chapter 5. Selective Actuation through Acoustic Shape Optimization

5.1. Introduction

Selective actuation can be easily found in nature, where the brain of a living organism sends signals to discrete parts of the body for complex movements. The field of soft robotics currently takes advantage of demultiplexers or relays to disperse the input to different parts of the system.[121,122] When the system is powered by fluidic pumps, these electrical components are connected to multiple valves to distribute pressure. In a more recent research, a soft demultiplexer that was controlled by a few pumps was developed to increase the number of outputs.[123] Gas flow was regulated by inflating a control channel and closing the main channel that was connected to the soft structure. Laying out the control channel and main channel into a grid pattern allowed the method to function as a demultiplexer. However, these methods all require additional hardware to achieve selective actuation. Electrical components, in particular, are very rigid and susceptible to damage when embedding them inside the soft system.

This chapter extends the idea of utilizing ultrasonic waves for soft robotics to achieve selective actuation. The core concept is to manipulate ultrasonic waves that can potentially replace electrical components, which selectively send signals to desired locations. This complex functionality can be embedded in a single material that acts as a frequency-selective waveguide. When applying ultrasonic waves to a waveguide that splits into several channels, the output at the end of each channel can be controlled by designing the size and shape of the material. The complex design of the system can be achieved by applying shape optimization on the waveguide. The amplified ultrasonic wave at the tip of a certain channel can be converted to heat, when the wave is absorbed in a soft material. Soft actuation is achieved when the embedded liquid is vaporized and inflates the soft structure. The other channels can be designed through shape optimization to damp the wave with the given frequency. In this chapter, a waveguide was first designed through shape optimization to maximize the acoustic output at a certain frequency and minimize the output at another frequency. After showing the proof-of-concept, a

waveguide that splits into two channels will be designed so that one channel amplified the wave at a certain frequency while damping the other. The second channel can be designed to behave in the opposite manner. This study shows promising results to develop demultiplexing systems in the material scale that can be utilized for soft robotics.

5.2. Shape and topology optimization

Shape and topology optimization are broad fields that became popular with the spread of additive manufacturing. Both methods are mathematical approaches to update the original shape and topology of a system to maximize or minimize certain parameters of interest, such as structural responses,[124] heat conduction,[125] or even both.[126] Shape optimization updates the shape of the selected boundary, whereas topology optimization updates the material distribution within a domain. As a result, topology optimization is more challenging to fabricate the complex design. In addition, the development of additive manufacturing enabled the fabrication of complex structures that can successfully manipulate acoustic waves[127] and light.[128] This study aims to optimize the outer shape of a waveguide to amplify or damp ultrasonic waves at certain frequencies. The sound pressure level (SPL) between the input and output of the waveguide was defined as the objective function to update the shape.

5.3. Shape optimization of cylindrical waveguide

Shape optimization was performed on a waveguide through *COMSOL*. The initial shape of the cylindrical waveguide was designed in an axis-symmetrical plane as shown in figure 43(a). An ultrasonic wave was numerically applied to the top boundary, which propagated towards the bottom. In order to make fabrication easier, the properties of a Pewter alloy (Sn-7.5Sb-0.5Cu wt.%) were used to define the material. The measured density and wave speed of the alloy was 7289 kg/m^3 and 3370 m/s, respectively. The harmonic sound wave in the material was defined using the Helmholtz equation:

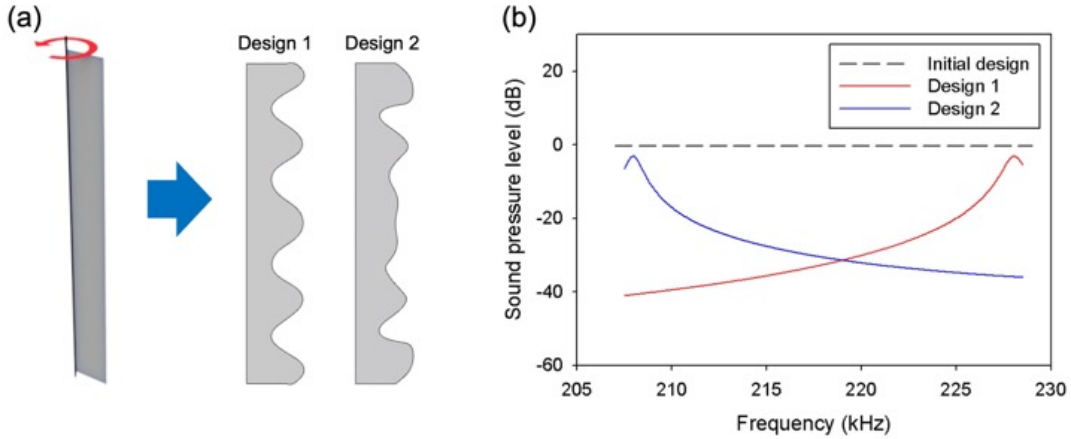

Figure 43. (a) An initial waveguide was designed in an axis-symmetrical plane. Design 1 is the shape of the waveguide that maximizes output at 228 kHz and minimizes output at 208 kHz. Design 2 outputs in an opposite trend. (b) The sound pressure level between the input and output of the wave is plotted over a range of frequency.

$$\nabla \cdot \left(-\frac{1}{\rho}\nabla p\right) - \left(\frac{w^2 p}{\rho c^2}\right) = 0 \tag{19}$$

where ρ is density, p is pressure, w is angular frequency, and c is speed of sound. The 2D domain was discretized predominantly by triangular meshes with 620 elements. The top layer was inlet port, bottom layer was outlet port, left layer was symmetry axis, and right layer was the free shape boundary. The following objective function that minimizes the sound pressure level was used for method of moving asymptotes (MMA):

$$Objective = \begin{cases} \log_{10}\dfrac{P_{out}}{P_{in}}, & when\ f < \dfrac{f_1 + f_2}{2} \\ -\log_{10}\dfrac{P_{out}}{P_{in}}, & when\ f \geq \dfrac{f_1 + f_2}{2} \end{cases} \tag{20}$$

where P_{in} is input power, P_{out} is output power, and f is frequency. Two frequencies (f_1 and f_2) were selected by conducting a frequency sweep on a piezoelectric disc. The two frequencies with the highest output were selected for this study (208 kHz and 228 kHz). The shape of the outer boundary was optimized to maximize and minimize the acoustic output. For each node, the maximum displacement and filter radius was set as 4 mm and 1.2 mm, respectively.

The results of shape optimization are also plotted in figure 43(a). Design 1 minimizes the output at 208 kHz and maximizes the output at 228 kHz. Design 2 was optimized to perform with an opposite trend. A frequency sweep was performed on these designs to evaluate their acoustic performances, and the results are shown in figure 43(b). The black dotted line represents the SPL of the initial cylindrical waveguide. The SPL of design 1 dropped as low as -40 dB at lower frequencies and reached around -2 dB at ~ 228 kHz. Frequency sweep result of design 2 showed the opposite trend, indicating that the shape optimization was successful.

5.4. Fabrication and performance of optimized waveguides

The steps to fabricate the waveguides are shown in figure 44. First, a positive mold with half of the waveguide was 3D-printed with Clear Resin using Form 3 (from Formlabs). The smallest layer thickness of 25 μm was used to maximize the resolution of the print. Then, uncured Mold Max 60 (from Smooth-on) was poured into the positive mold to create a heat resistant negative mold. The mixture was left in room temperature for 24 hours to fully cure into solid molds. Last, molten Pewter alloy was poured into the assembled negative mold. The alloy with melting point of ~ 300 °C was heated to 400 °C and was carefully poured into the mold. The mold was left in room temperature for several minutes before opening and removing the sample. Figure 45 shows the positive mold printed with clear resin on the left. The red mold on the right shows the heat resistant negative mold after casting Pewter alloy.

The fabricated waveguides of design 1 and 2 are shown in figure 46(a). Similar to the finite element study, a piezoelectric disc was bonded to the top of the waveguide using epoxy to apply ultrasonic waves. A similar disc was bonded to the bottom of the waveguide, which was connected to an oscilloscope to measure the wave output. The SPL of the test was obtained through the following equation:

$$SPL_{ex} = 20 \log_{10} \frac{V_{op}}{V_{in}} \tag{19}$$

where V_{op} and V_{in} are voltage measured from the optimized and initial waveguide, respectively, and the subscript *ex* denotes the SPL measured by experiment. The experimental result of the frequency sweep is shown in figure 46(b) as dotted plots. The dashed lines show the gaussian fit of the two results, and they are in good agreement with figure 43(b). These show promising results to implement acoustic shape optimization on waveguides to selectively actuate different parts of the system.

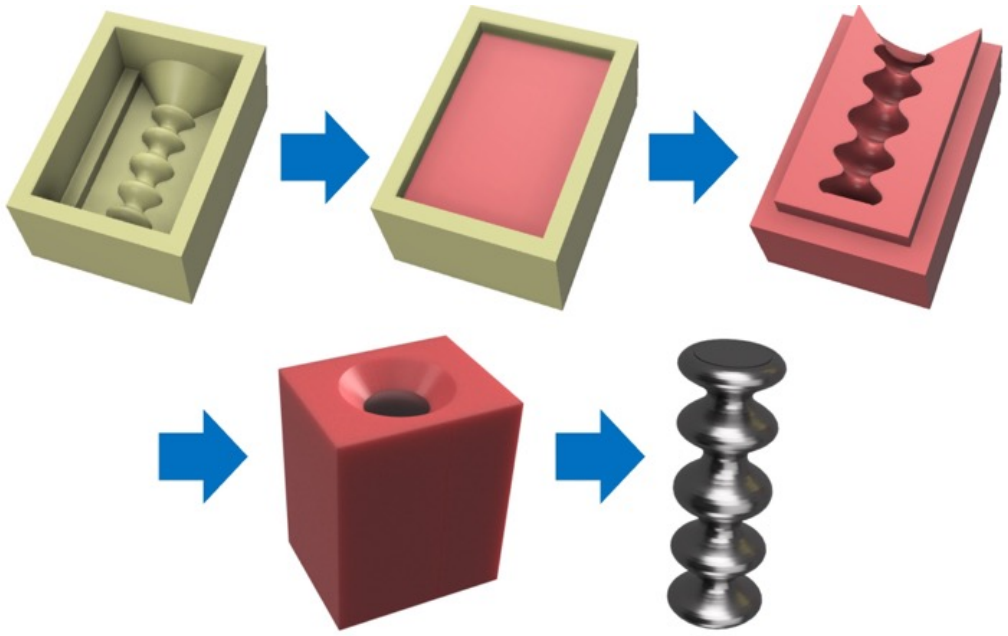

Figure 44. A positive mold was 3D printed using Form3. Next, a heat resistive rubber was poured to create a negative mold. The two parts of the negative mold was assembled, and molten Pewter alloy was poured to fabricate the waveguide.

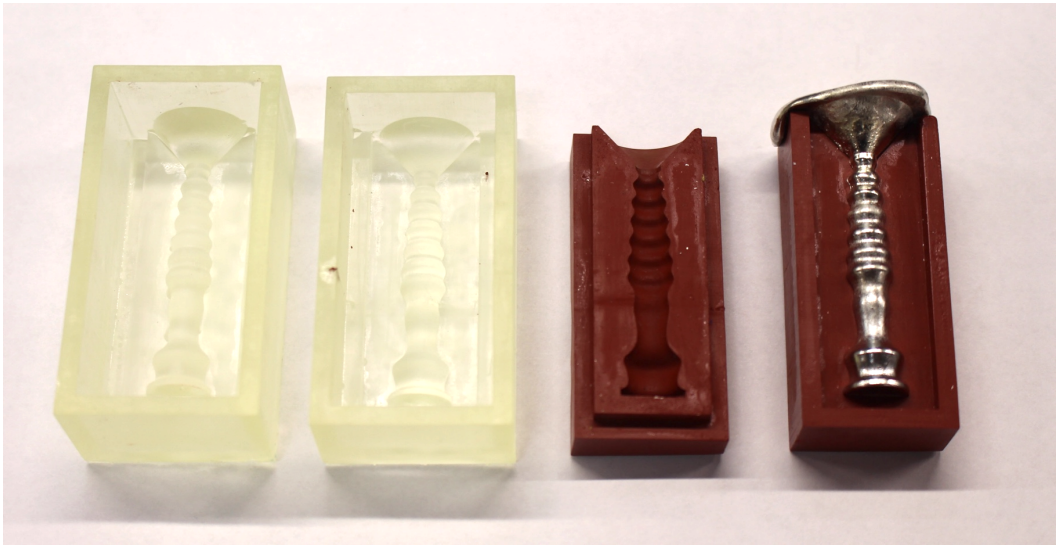

Figure 45. The image shows the 3D-printed positive mold, heat resistant negative mold, and casted sample.

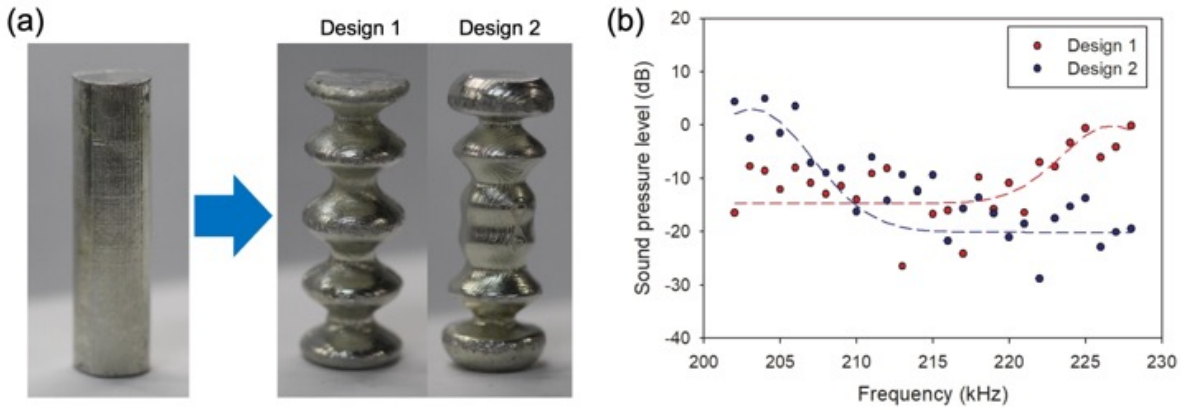

Figure 46. (a) The waveguides were fabricated by casting Pewter alloys in a negative mold. (b) A frequency sweep experiment was conducted on the waveguides to measure the sound pressure level.

5.5. Conclusions

This chapter shows preliminary results of utilizing ultrasonic waves to achieve selective actuation. The concept is to take advantage of shape optimization to design the waveguide that can send ultrasonic waves of certain frequency to designated locations in a soft structure. This method can potentially replace any complex electrical components (such as multiplexers or relays) that control electrical voltages for selective actuation. The function is instead achieved by a solid waveguide, which can be more robust and easier to fabricate than complex circuits. First, a simple waveguide in the shape of a rod was redesigned through shape optimization to maximize the output at a certain frequency while damping the signal at another frequency. These waveguides with periodic curvatures were then fabricated through additive manufacturing. A frequency sweep was conducted on the physical waveguides, which showed results that agreed with the numerical simulations. In order to fully implement this method for selective actuation, it should be applied to a waveguide that splits into several channels. Each output channel can be designed to maximize the output only at certain frequencies. Then, the ultrasonic waves at the tip must be converted to heat, which vaporizes liquid that is embedded in a soft material.

5.6. Acknowledgment

Chapter 5, in full, is currently being prepared for submission for publication of the material, H.-J. Lee, J.A. Mancini, C.M. Spadaccini, and K.J. Loh. The dissertation author was the primary investigator and author of this material. This work was supported by the U.S. National Science Foundation under Grant Nos. CMMI-1762530 and CMMI-2032021. Additional support was provided by the Jacobs School of Engineering, University of California San Diego.

Chapter 6. Conclusion

6.1. Summary of Results

This dissertation aims to advance the field of soft actuation through liquid vaporization by creatively combining the method with other techniques. The first limitation is that phase transformation is significantly sensitive to the environment. Extreme environments, such as underwater, drastically hinders actuation, since its surrounding acts as a large heat sink. Another limitation is that simply air cooling the system takes a long time to return the actuated structure to its original shape. Chapter 2 solves these issues by actively controlling heat loss through a thermoelectric device. The soft walls were designed to have two layers, which significantly decreased thermal conductivity. The thermoelectric device was installed beneath the embedded liquid, which actively heated and cooled the system. The setup allowed effective actuation even underwater, while decreasing the cooling time by ~ 60 %. The popular method of using pneumatic pumps for actuation requires the inflating chambers to be physically tethered to the large and heavy pump. Chapter 3 aims to improve this setup by applying ultrasonic waves that propagate through the structure. The ultrasonic wave propagated through a thin metal sheet, which heated and dispersed the liquid into small droplets. This method allowed the demonstration of a soft gripper with detachable fingers for easy replacements. One of the most significant limitations of actuation through vaporization is actuation speed. In general, boiling the liquid takes a long time due to high heat capacity and low thermal conductivity of the materials and liquid used in the system. In addition, the embedded heater must always be in contact with the liquid to achieve vaporization, which can limit the method to applications that rotate the system. The method introduced in chapter 4 is an improvement of the results shown in chapter 3 to solve these limitations. A piece of cotton absorbed and supplied the liquid to a vibrating mesh atomizer. The atomizer dispersed the liquid into small droplets that were ejected into a heater. The overall system required significantly less power than ultrasonic atomization, while performing similar to pneumatic pumps. This method was also

capable of storing a large amount of liquid without sacrificing actuation speed. As a result, the structure was returned to its original shape by simply exhausting the vapor. This allowed much faster cyclic actuation as compared to cooling the entire system. Chapter 5 introduces a method to fully utilize ultrasonic wave properties to achieve selective actuation. The ultrasonic waves were manipulated by designing frequency selective waveguides by employing shape optimization of a cylindrical rod. The fabricated waveguides showed that the method could successfully maximize and minimize the output at selected frequencies (*i.e.*, to route and amplify or dampen ultrasonic waves at designated locations of the waveguide). This method has demonstrated potential for replacing electrical components while achieving selective actuation by embedding the function into waveguides.

6.2. Future works

While actuation through vibrating mesh atomization in chapter 4 showed promising results, further optimization is required to maximize its performance. Since the method is a complex multi-physics problem, there are numerous parameters and designs that need to be studied to acquire its full potential. Some of the works include but are not limited to optimizing the flow of droplets within the heater, designing the heater to maximize droplet evaporation, determining the optimal atomization rate for heaters with complex shapes, adjusting atomization rate throughout actuation, designing the structure to minimize temperature gradients within the system, and developing a setup that can recycle the liquid for cyclic actuation.

Another limitation of soft actuation through vaporization is the permeability of soft elastomers. When the system is left for a long time, the embedded liquid diffuses through the structure, resulting in an empty chamber. A system with composite materials should be studied to minimize the permeability while including other functionalities to solve this issue. The method introduced in chapter 5 also needs further study to demonstrate its validity. A waveguide that splits into several channels will be designed through shape optimization. The design aims to maximize the input signal at different channels when the frequency of the ultrasonic wave is adjusted. Then, the ultrasonic wave at the output must be

converted into heat to vaporize the embedded liquid. A soft robotic structure that contains the piezoelectric element at its head will be developed to fully mimic the performance of biological systems.

Soft robotics is expected to solve the limitation of current automated systems in various ways. The lightweight system capable of adjusting to its surrounding will allow safe human interactions and enable the field to blend into our everyday lives. Their ability to adapt to the environment will also help soft robotics to perform dangerous tasks or function in hazardous conditions. A dire need for soft robotics also includes automation in the industry due to the aging population, where the number of older people is expected to constantly increase. Soft robotics is in its very early stage, and advanced technologies introduced only in movies will be possible with continued study and development in the field.

References

1. Ebert, D. M. & Henrich, D. D. (2002). Safe human-robot-cooperation: Image-based collision detection for industrial robots. Paper presented at: 2002 Ieee/Rsj International Conference on Intelligent Robots and Systems, Vols 1-3, Proceedings.

2. Pedrocchi, N., Vicentini, F., Matteo, M. & Tosatti, L. M. Safe human-robot cooperation in an industrial environment. *International Journal of Advanced Robotic Systems* **10**, 27, (2013).

3. Bruzzone, L. & Quaglia, G. Review article: Locomotion systems for ground mobile robots in unstructured environments. *Mechanical Sciences* **3**, 49-62, (2012).

4. Aguilar, J., Zhang, T., Qian, F., Kingsbury, M., McInroe, B., Mazouchova, N., Li, C., Maladen, R., Gong, C., Travers, M., Hatton, R., Choset, H., Umbanhowar, P. & Goldman, D. A review on locomotion robophysics: The study of movement at the intersection of robotics, soft matter and dynamical systems. *Reports on Progress in Physics* **79**, 110001, (2016).

5. Hughes, J., Culha, U., Giardina, F., Guenther, F., Rosendo, A. & Iida, F. Soft manipulators and grippers: A review. *Frontiers in Robotics and AI* **3**, 69, (2016).

6. Elango, N. & Faudzi, A. A review article: Investigations on soft materials for soft robot manipulations. *International Journal of Advanced Manufacturing Technology* **80**, 1027-1037, (2015).

7. Oliver, K., Seddon, A. & Trask, R. Morphing in nature and beyond: A review of natural and synthetic shape-changing materials and mechanisms. *Journal of Materials Science* **51**, 10663-10689, (2016).

8. Landkammer, S., Winter, F., Schneider, D. & Hornfeck, R. Biomimetic spider leg joints: A review from biomechanical research to compliant robotic actuators. *Robotics* **5**, 15, (2016).

9. Shadwick, R. E. & Gosline, J. M. Mechanical-properties of the octopus aorta. *Journal of Experimental Biology* **114**, 259-284, (1985).

10. Margheri, L., Laschi, C. & Mazzolai, B. Soft robotic arm inspired by the octopus: I. From biological functions to artificial requirements. *Bioinspiration & Biomimetics* **7**, 025004, (2012).

11. Allen, J. J., Bell, G. R. R., Kuzirian, A. M., Velankar, S. S. & Hanlon, R. T. Comparative morphology of changeable skin papillae in octopus and cuttlefish. *Journal of Morphology* **275**, 371-390, (2014).

12. Kier, W. M. & Stella, M. P. The arrangement and function of octopus arm musculature and connective tissue. *Journal of Morphology* **268**, 831-843, (2007).

13. Walker, I. D., Dawson, D. M., Flash, T., Grasso, F. W., Hanlon, R. T., Hochner, B., Kier, W. M., Pagano, C. C., Rahn, C. D. & Zhang, Q. M. Continuum robot arms inspired by cephalopods. *Unmanned Ground Vehicle Technology VII* **5804**, 303-314, (2005).

14. Cooper, K. M., Hanlon, R. T. & Budelmann, B. U. Physiological color-change in squid iridophores .2. Ultrastructural mechanisms in lolliguncula-brevis. *Cell and Tissue Research* **259**, 15-24, (1990).

15. Laschi, C., George, T., Dutta, A. & Islam, M. (2016). Soft robotics: From scientific challenges to technological applications. Paper presented at: Micro- and Nanotechnology Sensors, Systems, and Applications Viii.

16. Rus, D. & Tolley, M. Design, fabrication and control of soft robots. *Nature* **521**, 467-475, (2015).

17. Erb, R. M., Sander, J. S., Grisch, R. & Studart, A. R. Self-shaping composites with programmable bioinspired microstructures. *Nature Communications* **4**, 1712, (2013).

18. Lipson, H. Challenges and opportunities for design, simulation, and fabrication of soft robots. *Soft Robotics* **1**, 21-27, (2014).

19. Ross, D., Nemitz, M. & Stokes, A. Controlling and simulating soft robotic systems: Insights from a thermodynamic perspective. *Soft Robotics* **3**, 170-176, (2016).

20. Kim, S., Laschi, C. & Trimmer, B. Soft robotics: A bioinspired evolution in robotics. *Trends in Biotechnology* **31**, 23-30, (2013).

21. Mattar, E. A survey of bio-inspired robotics hands implementation: New directions in dexterous manipulation. *Robotics and Autonomous Systems* **61**, 517-544, (2013).

22. Lee, C., Kim, M., Kim, Y., Hong, N., Ryu, S., Kim, H. & Kim, S. Soft robot review. *International Journal of Control Automation and Systems* **15**, 3-15, (2017).

23. Mosadegh, B., Polygerinos, P., Keplinger, C., Wennstedt, S., Shepherd, R. F., Gupta, U., Shim, J., Bertoldi, K., Walsh, C. J. & Whitesides, G. M. Pneumatic networks for soft robotics that actuate rapidly. *Advanced Functional Materials* **24**, 2163-2170, (2014).

24. Ilievski, F., Mazzeo, A. D., Shepherd, R. E., Chen, X. & Whitesides, G. M. Soft robotics for chemists. *Angewandte Chemie-International Edition* **50**, 1890-1895, (2011).

25. Suzumori, K., Endo, S., Kanda, T., Kato, N. & Suzuki, H. (2007). A bending pneumatic rubber actuator realizing soft-bodied manta swimming robot. Paper presented at: Proceedings of the 2007 Ieee International Conference on Robotics and Automation, Vols 1-10.

26. Connolly, F., Walsh, C. J. & Bertoldi, K. (2017). Automatic design of fiber-reinforced soft actuators for trajectory matching. Paper presented at: Proceedings of the National Academy of Sciences of the United States of America.

27. Connolly, F., Polygerinos, P., Walsh, C. J. & Bertoldi, K. Mechanical programming of soft actuators by varying fiber angle. *Soft Robotics* **2**, 26-32, (2015).

28. Jani, J. M., Leary, M., Subic, A. & Gibson, M. A. A review of shape memory alloy research, applications and opportunities. *Materials & Design* **56**, 1078-1113, (2014).

29. Laschi, C., Cianchetti, M., Mazzolai, B., Margheri, L., Follador, M. & Dario, P. Soft robot arm inspired by the octopus. *Advanced Robotics* **26**, 709-727, (2012).

30. Hines, L., Petersen, K., Lum, G. & Sitti, M. Soft actuators for small-scale robotics. *Advanced Materials* **29**, 1603483, (2017).

31. Tondu, B. & Lopez, P. Modeling and control of mckibben artificial muscle robot actuators. *Ieee Control Systems Magazine* **20**, 15-38, (2000).

32. Albn-Schaffer, A., Fischer, M., Schreiber, G., Schoeppe, E. & Hirzinger, G. (2004). Soft robotics: What cartesian stiffness can we obtain with passively compliant, uncoupled joints? Paper presented at: IEEE/RSl International Conference on Intelligent Robots and Systems (Sendai, Japan).

33. Laschi, C., Mazzolai, B., Mattoli, V., Cianchetti, M. & Dario, P. Design of a biomimetic robotic octopus arm. *Bioinspiration & Biomimetics* **4**, 015006 (2009).

34. Lin, H. T., Leisk, G. G. & Trimmer, B. Goqbot: A caterpillar-inspired soft-bodied rolling robot. *Bioinspiration & Biomimetics* **6**, 026007, (2011).

35. Seok, S., Onal, C. D., Wood, R., Rus, D. & Kim, S. (2010). Peristaltic locomotion with antagonistic actuators in soft robotics. Paper presented at: 2010 Ieee International Conference on Robotics and Automation (Icra).

36. Bao, G. J., Fang, H., Chen, L. F., Wan, Y. H., Xu, F., Yang, Q. H. & Zhang, L. B. Soft robotics: Academic insights and perspectives through bibliometric analysis. *Soft Robotics* **5**, 229-241, (2018).

37. Marchese, A. D., Katzschmann, R. K. & Rus, D. A recipe for soft fluidic elastomer robots. *Soft Robotics* **2**, 7-25, (2015).

38. Katzschmann, R. K., DelPreto, J., MacCurdy, R. & Rus, D. Exploration of underwater life with an acoustically controlled soft robotic fish. *Science Robotics* **3**, eaar3449, (2018).

39. Marchese, A. D., Onal, C. D. & Rus, D. Autonomous soft robotic fish capable of escape maneuvers using fluidic elastomer actuators. *Soft Robotics* **1**, 75-87, (2014).

40. Galloway, K. C., Becker, K. P., Phillips, B., Kirby, J., Licht, S., Tchernov, D., Wood, R. J. & Gruber, D. F. Soft robotic grippers for biological sampling on deep reefs. *Soft Robotics* **3**, 23-33, (2016).

41. Wehner, M., Tolley, M., Menguc, Y., Park, Y., Mozeika, A., Ding, Y., Onal, C., Shepherd, R., Whitesides, G. & Wood, R. Pneumatic energy sources for autonomous and wearable soft robotics. *Soft Robotics* **1**, 263-274, (2014).

42. Reymundo, A., Munoz, E., Navarro, M., Vela, E. & Krebs, H. (2016). Hand rehabilitation using soft-robotics. Paper presented at: 2016 6th Ieee International Conference on Biomedical Robotics and Biomechatronics (Biorob).

43. Belforte, G., Eula, G., Ivanov, A. & Sirolli, S. Soft pneumatic actuators for rehabilitation. *Actuators* **3**, 84-106, (2014).

44. Kang, R. J., Guo, Y., Chen, L. S., Branson, D. T. & Dai, J. S. Design of a pneumatic muscle based continuum robot with embedded tendons. *Ieee-Asme Transactions on Mechatronics* **22**, 751-761, (2017).

45. Tolley, M. T., Shepherd, R. F., Mosadegh, B., Galloway, K. C., Wehner, M., Karpelson, M., Wood, R. J. & Whitesides, G. M. A resilient, untethered soft robot. *Soft Robotics* **1**, 213-223, (2014).

46. Terryn, S., Brancart, J., Lefeber, D., Van Assche, G. & Vanderborght, B. Self-healing soft pneumatic robots. *Science Robotics* **2**, eaan4268, (2017).

47. Liu, Y. L. & Chuo, T. W. Self-healing polymers based on thermally reversible diels-alder chemistry. *Polymer Chemistry* **4**, 2194-2205, (2013).

48. Altmuller, R., Schwodiauer, R., Kaltseis, R., Bauer, S. & Graz, I. M. Large area expansion of a soft dielectric membrane triggered by a liquid gaseous phase change. *Applied Physics a-Materials Science & Processing* **105**, 1-3, (2011).

49. Miriyev, A., Stack, K. & Lipson, H. Soft material for soft actuators. *Nature Communications* **8**, 596, (2017).

50. Miriyev, A., Caires, G. & Lipson, H. Functional properties of silicone/ethanol soft-actuator composites. *Materials & Design* **145**, 232-242, (2018).

51. Boyvat, M., Vogt, D. M. & Wood, R. J. Ultrastrong and high-stroke wireless soft actuators through liquid-gas phase change. *Advanced Materials Technologies* **4**, 1800381, (2019).

52. Nishikawa, Y. & Matsumoto, M. A design of fully soft robot actuated by gas-liquid phase change. *Advanced Robotics* **33**, 567-575, (2019).

53. Han, J., Jiang, W., Niu, D., Li, Y., Zhang, Y., Lei, B., Liu, H., Shi, Y., Chen, B., Yin, L., Liu, X., Peng, D. & Lu, B. Untethered soft actuators by liquid–vapor phase transition: Remote and programmable actuation. *Advanced Intelligent Systems* **1**, 1900109, (2019).

54. An, S. M., Ryu, J., Cho, M. & Cho, K. J. Engineering design framework for a shape memory alloy coil spring actuator using a static two-state model. *Smart Materials and Structures* **21**, (2012).

55. Mavroidis, C. Development of advanced actuators using shape memory alloys and electrorheological fluids. *Research in Nondestructive Evaluation* **14**, 1-32, (2002).

56. Liu, C. Y. & Liao, W. H. A snake robot using shape memory alloys. *IEEE ROBIO 2004: Proceedings of the IEEE International Conference on Robotics and Biomimetics*, 601-605, (2004).

57. Rodrigue, H., Wang, W., Han, M. W., Kim, T. J. Y. & Ahn, S. H. An overview of shape memory alloy-coupled actuators and robots. *Soft Robotics* **4**, 3-15, (2017).

58. Lee, Y. P., Kim, B. K., Lee, M. G. & Park, J. O. (2004). Locomotive mechanism design and fabrication of biomimetic micro robot using shape memory alloy. Paper presented at: 2004 Ieee International Conference on Robotics and Automation, Vols 1- 5, Proceedings.

59. Seok, S., Onal, C. D., Cho, K. J., Wood, R. J., Rus, D. & Kim, S. Meshworm: A peristaltic soft robot with antagonistic nickel titanium coil actuators. *Ieee-Asme Transactions on Mechatronics* **18**, 1485-1497, (2013).

60. Ko, H. & Javey, A. Smart actuators and adhesives for reconfigurable matter. *Accounts of Chemical Research* **50**, 691-702, (2017).

61. Kirillova, A. & Ionov, L. Shape-changing polymers for biomedical applications. *Journal of Materials Chemistry B* **7**, 1597-1624, (2019).

62. Kwon, G. H., Park, J. Y., Kim, J. Y., Frisk, M. L., Beebe, D. J. & Lee, S. H. Biomimetic soft multifunctional miniature aquabots. *Small* **4**, 2148-2153, (2008).

63. Must, I., Kaasik, F., Poldsalu, I., Mihkels, L., Johanson, U., Punning, A. & Aabloo, A. Ionic and capacitive artificial muscle for biomimetic soft robotics. *Advanced Engineering Materials* **17**, 84-94, (2015).

64. Garstecki, P., Tierno, P., Weibel, D. B., Sagues, F. & Whitesides, G. M. Propulsion of flexible polymer structures in a rotating magnetic field. *Journal of Physics-Condensed Matter* **21**, 204110, (2009).

65. Taccola, S., Greco, F., Sinibaldi, E., Mondini, A., Mazzolai, B. & Mattoli, V. Toward a new generation of electrically controllable hygromorphic soft actuators. *Advanced Materials* **27**, 1668, (2015).

66. He, Q. G., Wang, Z. J., Wang, Y., Minori, A., Tolley, M. T. & Cai, S. Q. Electrically controlled liquid crystal elastomer-based soft tubular actuator with multimodal actuation. *Science Advances* **5**, eaax5746, (2019).

67. Yamada, M., Kondo, M., Mamiya, J. I., Yu, Y. L., Kinoshita, M., Barrett, C. J. & Ikeda, T. Photomobile polymer materials: Towards light-driven plastic motors. *Angewandte Chemie-International Edition* **47**, 4986-4988, (2008).

68. Harris, K. D., Cuypers, R., Scheibe, P., van Oosten, C. L., Bastiaansen, C. W. M., Lub, J. & Broer, D. J. Large amplitude light-induced motion in high elastic modulus polymer actuators. *Journal of Materials Chemistry* **15**, 5043-5048, (2005).

69. Lee, H., Xia, C. G. & Fang, N. X. First jump of microgel; actuation speed enhancement by elastic instability. *Soft Matter* **6**, 4342-4345, (2010).

70. Menges, A. & Reichert, S. Material capacity: Embedded responsiveness. *Architectural Design* **82**, 52-59, (2012).

71. Wang, J. R., Wang, J. F., Chen, Z., Fang, S. L., Zhu, Y., Baughman, R. H. & Jiang, L. Tunable, fast, robust hydrogel actuators based on evaporation-programmed heterogeneous structures. *Chemistry of Materials* **29**, 9793-9801, (2017).

72. Wu, Z. L., Moshe, M., Greener, J., Therien-Aubin, H., Nie, Z. H., Sharon, E. & Kumacheva, E. Three-dimensional shape transformations of hydrogel sheets induced by small-scale modulation of internal stresses. *Nature Communications* **4**, 1586, (2013).

73. Kularatne, R. S., Kim, H., Boothby, J. M. & Ware, T. H. Liquid crystal elastomer actuators: Synthesis, alignment, and applications. *Journal of Polymer Science Part B-Polymer Physics* **55**, 395-411, (2017).

74. Ganji, F., Vasheghani-Farahani, S. & Vasheghani-Farahani, E. Theoretical description of hydrogel swelling: A review. *Iranian Polymer Journal* **19**, 375-398, (2010).

75. Ahmed, E. M. Hydrogel: Preparation, characterization, and applications: A review. *Journal of Advanced Research* **6**, 105-121, (2015).

76. Cartolano, M., Xia, B. X., Miriyev, A. & Lipson, H. Conductive fabric heaters for heat-activated soft actuators. *Actuators* **8**, 9, (2019).

77. Oh, S., Kim, S. U., Yeom, S., Kim, H., Kim, S. & Na, J. H. Continuum soft actuators based on reprogrammable geometric constraints. *Extreme Mechanics Letters* **36**, 100649, (2020).

78. Chellattoan, R., Yudhanto, A. & Lubineau, G. Low-voltage-driven large-amplitude soft actuators based on phase transition. *Soft Robotics* **7**, 688-699, (2020).

79. Li, X. Y., Duan, H. L., Lv, P. Y. & Yi, X. Soft actuators based on liquid-vapor phase change composites. *Soft Robotics* **8**, 251-261, (2020).

80. Oh, B., Park, Y. G., Jung, H., Ji, S., Cheong, W. H., Cheon, J., Lee, W. & Park, J. U. Untethered soft robotics with fully integrated wireless sensing and actuating systems for somatosensory and respiratory functions. *Soft Robotics* **7**, 564-573, (2020).

81. Kim, Y. I., An, S., Yarin, A. L. & Yoon, S. S. Performance enhancement of soft nanotextured thermopneumatic actuator by incorporating silver nanowires into elastomer body. *Soft Robotics*, (in press).

82. Hiraki, T., Nakahara, K., Narumi, K., Niiyama, R., Kida, N., Takamura, N., Okamoto, H. & Kawahara, Y. Laser pouch motors: Selective and wireless activation of soft actuators by laser-powered liquid-to-gas phase change. *Ieee Robotics and Automation Letters* **5**, 4180-4187, (2020).

83. Hong, S., Gu, Y., Seo, J. K., Wang, J., Liu, P., Meng, Y. S., Xu, S. & Chen, R. K. Wearable thermoelectrics for personalized thermoregulation. *Science Advances* **5**, eaaw0536, (2019).

84. dos Santos, W. N. & Gregorio, R. Hot-wire parallel technique: A new method for simultaneous determination of thermal properties of polymers. *Journal of Applied Polymer Science* **85**, 1779-1786, (2002).

85. Healy, J. J., Degroot, J. J. & Kestin, J. Theory of transient hot-wire method for measuring thermal-conductivity. *Physica B & C* **82**, 392-408, (1976).

86. Merckx, B., Dudoignon, P., Garnier, J. P. & Marchand, D. Simplified transient hot-wire method for effective thermal conductivity measurement in geo materials: Microstructure and saturation effect. *Advances in Civil Engineering* **2012**, 625395, (2012).

87. Lee, H.-J., Melchor, N., Chung, H. & Loh, K. J. (2020). Characterization of a soft gripper with detachable fingers through rapid evaporation. Paper presented at: 2020 3rd IEEE International Conference on Soft Robotics (RoboSoft).

88. Batham, E. J. & Pantin, C. F. A. Muscular and hydrostatic action in the sea-anemone metridium-senile (l). *Journal of Experimental Biology* **27**, 264-289, (1950).

89. Ansell, A. D. & Trueman, E. R. The mechanism of burrowing in the anemone, peachia hastata gosse. *Journal of Experimental Marine Biology and Ecology* **2**, 124-134, (1968).

90. Sund, P. N. A study of the muscular anatomy and swimming behaviour of the sea anemone, stomphia-coccinea. *Quarterly Journal of Microscopical Science* **99**, 401-420, (1958).

91. Wood, R. W. & Loomis, A. L. The physical and biological effects of high-frequency sound-waves of great intensity. *Philosophical Magazine* **4**, 417-436, (1927).

92. Lang, R. J. Ultrasonic atomization of liquids. *Journal of the Acoustical Society of America* **34**, 6-8, (1962).

93. Stevens, H. R. & Albregt, H. B. Assessment of ultrasonic nebulization. *Anesthesiology* **27**, 648-653, (1966).

94. Inculet, I. I. & Klein, R. G. Electrostatic painting of nonconductive surfaces with water-base paints. *Ieee Transactions on Industry Applications* **32**, 90-92, (1996).

95. Nandiyanto, A. B. D. & Okuyama, K. Progress in developing spray-drying methods for the production of controlled morphology particles: From the nanometer to submicrometer size ranges. *Advanced Powder Technology* **22**, 1-19, (2011).

96. Okawa, H., Nishi, K., Kawamura, Y., Kato, T. & Sugawara, K. Utilization of ultrasonic atomization for dust control in underground mining. *Japanese Journal of Applied Physics* **56**, 07JE10, (2017).

97. Lee, H.-J., Funderburk, M. & Loh, K. J. (2018). Actuation of soft materials through ultrasonic atomization. Paper presented at: SPIE Smart Structures and Materials + Nondestructive Evaluation and Health Monitoring (Denver: SPIE).

98. Sollner, K. The mechanism of the formation of fogs by ultrasonic waves. *Transactions of the Faraday Society* **32**, 1532-1536, (1936).

99. Yasuda, K., Honma, H., Xu, Z., Asakura, Y. & Koda, S. Ultrasonic atomization amount for different frequencies. *Japanese Journal of Applied Physics* **50**, 07HE23, (2011).

100. Ramisetty, K. A., Pandit, A. B. & Gogate, P. R. Investigations into ultrasound induced atomization. *Ultrasonics Sonochemistry* **20**, 254-264, (2013).

101. Barreras, F., Amaveda, H. & Lozano, A. Transient high-frequency ultrasonic water atomization. *Experiments in Fluids* **33**, 405-413, (2002).

102. Mahravan, E., Naderan, H. & Damangir, E. Frequency and wavelength prediction of ultrasonic induced liquid surface waves. *Ultrasonics* **72**, 184-190, (2016).

103. Babin, V. & Holyst, R. Evaporation of a sub-micrometer droplet. *Journal of Physical Chemistry B* **109**, 11367-11372, (2005).

104. Lee, H.-J. & Loh, K. J. Soft material actuation by atomization. *Smart Materials and Structures* **28**, 025030, (2019).

105. Faeth, G. M., Hsiang, L. P. & Wu, P. K. Structure and breakup properties of sprays. *International Journal of Multiphase Flow* **21**, 99-127, (1995).

106. Soid, S. N. & Zainal, Z. A. Spray and combustion characterization for internal combustion engines using optical measuring techniques - a review. *Energy* **36**, 724-741, (2011).

107. Le Brun, P. P. H., de Boer, A. H., Heijerman, H. G. M. & Frijlink, H. W. A review of the technical aspects of drug nebulization. *Pharmacy World & Science* **22**, 75-81, (2000).

108. Yan, Q. F., Wu, C. Y. & Zhang, J. H. Effect of the dynamic cone angle on the atomization performance of a piezoceramic vibrating mesh atomizer. *Applied Sciences-Basel* **9**, 1836, (2019).

109. Beck-Broichsitter, M., Paulus, I. E., Greiner, A. & Kissel, T. Modified vibrating-mesh nozzles for advanced spray-drying applications. *European Journal of Pharmaceutics and Biopharmaceutics* **92**, 96-101, (2015).

110. Beck-Broichsitter, M., Knuedeler, M. C., Seeger, W. & Schmehl, T. Controlling the droplet size of formulations nebulized by vibrating-membrane technology. *European Journal of Pharmaceutics and Biopharmaceutics* **87**, 524-529, (2014).

111. Beck-Broichsitter, M., Schmehl, T. & Seeger, W. Customized vibrating-membrane nozzles for enhanced fluid atomization. *Aerosol Science and Technology* **49**, iii-viii, (2015).

112. Kuo, Y. M., Chan, W. H., Lin, C. W., Huang, S. H. & Chen, C. C. Characterization of vibrating mesh aerosol generators. *Aerosol and Air Quality Research* **19**, 1678-1687, (2019).

113. Li, T., Nishida, K. & Hiroyasu, H. Droplet size distribution and evaporation characteristics of fuel spray by a swirl type atomizer. *Fuel* **90**, 2367-2376, (2011).

114. Banerjee, R. Numerical investigation of evaporation of a single ethanol/iso-octane droplet. *Fuel* **107**, 724-739, (2013).

115. Rupitsch, S. J. (2019). Piezoelectric sensors and actuators. Berlin: Springer

116. Li, F. X. & Li, G. J. (2015). Application of ansys apdl in the design of piezoelectric transducer. Paper presented at: Proceedings of the 2015 International Conference on Advanced Engineering Materials and Technology.

117. Dou, Y. C., Luo, H. & Zhang, J. Elastic properties of fecr20ni8xn (x = mo, nb, ta, ti, v, w and zr) austenitic stainless ateels: A first principles study. *Metals* **9**, 145, (2019).

118. Pedersen, C. B. W., Buhl, T. & Sigmund, O. Topology synthesis of large-displacement compliant mechanisms. *International Journal for Numerical Methods in Engineering* **50**, 2683-2705, (2001).

119. Canfield, S. & Frecker, M. Topology optimization of compliant mechanical amplifiers for piezoelectric actuators. *Structural and Multidisciplinary Optimization* **20**, 269-279, (2000).

120. Hu, N. & Burgueno, R. Buckling-induced smart applications: Recent advances and trends. *Smart Materials and Structures* **24**, 063001, (2015).

121. Naranjo, A., Martin, C., Lopez-Diaz, A., Martin-Pacheco, A., Rodriguez, A. M., Patino, F. J., Herrero, M. A., Vazquez, A. S. & Vazquez, E. Autonomous self-healing hydrogel with anti-drying properties and applications in soft robotics. *Applied Materials Today* **21**, 100806, (2020).

122. Miao, Y., Dong, W. & Du, Z. J. (2017). Design of a soft robot with multiple motion patterns using soft pneumatic actuators. Paper presented at: 2017 4th International Conference on Advanced Materials, Mechanics and Structural Engineering (4th Ammse 2017).

123. Bartlett, N. W., Becker, K. P. & Wood, R. J. A fluidic demultiplexer for controlling large arrays of soft actuators. *Soft Matter* **16**, 5871-5877, (2020).

124. Hsu, Y. L. A review of structural shape optimization. *Computers in Industry* **25**, 3-13, (1994).

125. Bruns, T. E. Topology optimization of convection-dominated, steady-state heat transfer problems. *International Journal of Heat and Mass Transfer* **50**, 2859-2873, (2007).

126. Kambampati, S., Gray, J. S. & Kim, H. A. Level set topology optimization of structures under stress and temperature constraints. *Computers & Structures* **235**, 106265, (2020).

127. Zhu, Y. F., Gerard, N. J. R. K., Xia, X. X., Stevenson, G. C., Cao, L. Y., Fan, S. W., Spadaccini, C. M., Jing, Y. & Assouar, B. Systematic design and experimental demonstration of transmission-type multiplexed acoustic metaholograms. *Advanced Functional Materials* **31**, 2101947, (2021).

128. Huang, J., Yang, J. B., Chen, D. B., Bai, W., Han, J. M., Zhang, Z. J., Zhang, J. J., He, X., Han, Y. X. & Liang, L. M. Implementation of on-chip multi-channel focusing wavelength demultiplexer with regularized digital metamaterials. *Nanophotonics* **9**, 159-166, (2020).